University of Reading

Instrumental Development of an Atmospheric Pressure Liquid UV-MALDI Mass Spectrometer Source and Interface for the Analysis of Multiply Protonated Peptide Ions

PhD in Chemistry, May 2020

Jeffery M. Brown
21810289

Declaration

I confirm that this is my own work and the use of all material from other sources has been properly and fully acknowledged.

Signed  Jeffery Brown

Date……14th May 2020

Acknowledgements

I would like to express my sincere thanks to my academic supervisor Professor Dr. Rainer Cramer who has provided limitless support and enthusiasm for this project. In addition, I thank my industrial supervisor, Dr. Michael Morris (Senior Director MS Research at Waters) for his guidance, strong support and for facilitating the project within Waters Research in Wilmslow. I am also very grateful to Professor Cramer's past and present group members as well as my colleagues in the Mass Spectrometry Research Departments in Waters. Thank you to Professor Joe Beckman who travelled to Wilmslow (from Oregon, USA) on more than one occasion to assist with the installation of the prototype ECD cell. Also, Dr. Keith Richardson (Waters Research) for modifications to the mass spectrometer control software to enable high throughput data acquisition.

I also thank my wife, Ruth and our two daughters, Hannah and Lucy for their patience and support.

Abstract

Over the last three decades, electrospray ionisation (ESI) and matrix-assisted laser desorption/ionisation (MALDI) have been the most prevalent types of ion source fitted to commercial instruments for biological mass spectrometry (MS) analysis. In particular, the qualitative and quantitative analysis of peptides and proteins has been revolutionised by these techniques. Also, the routine analysis of many other molecule types including DNA, sugars, carbohydrates, synthetic polymers and even virus capsids has been facilitated by ESI and MALDI.

Despite the commercial success of these ionisation methods, there are relative advantages and limitations inherent to both techniques. For example, conventional solid-state crystalline MALDI generates mainly singly charged analyte ions. As the ion of interest increases in mass, the mass spectrometer analysis becomes compromised. In contrast, liquid atmospheric pressure (AP) MALDI source (the focus of this work) generates multiply charged ions and is more suited for coupling with high-performance MS systems. ESI also produces a spatially diffuse beam of ions from a flowing liquid inlet whereas the source of ions from liquid AP-MALDI can be precisely controlled by the laser, both in time and space. Ultimately, flexibility of control will enable ultrahigh-throughput sample rates.

Liquid AP-MALDI MS is the focus of this thesis and includes details of the design and optimisation of the new ion source and coupling interface. Significant advances in the performance of the ionisation source are reported with attention to the optimisation of the pressure regime and temperature of the ion inlet interface. Focusing on multiply protonated peptides, instrumental developments have been applied to increase the sensitivity (ions detected per mole), signal persistence, as well as the speed of analysis using fast laser repetition rates of up to 5 kHz. Charge state enhancement through ion mobility offers signal-

to-noise increases of up to two orders. Electron-mediated fragmentation of multiply charged ions from liquid AP-MALDI provides new tandem MS functionality relative to conventional singly charged MALDI ions (that would be neutralised by electrons in ECD). Although the new MALDI technique produces ESI-like spectra, the advantage of a discrete spatial ionisation point and time offers the distinct possibility of ultra-high-throughput sample acquisition from high-density sample arrays at rates theoretically limited to greater than 100 samples/second. It is therefore concluded that the liquid AP-MALDI source provides powerful enhancements over both ESI and conventional MALDI.

Contents

Table of figures

Publications related to this work

There are several publications related to this work co-authored with Reading University and Waters Research group members. I have provided varying levels of contribution to these papers. In addition to my assistance in reviewing the data and content, I have contributed more generally to the initial design of the liquid AP-MALDI ion source and the heated inlet interface for coupling with the Synapt (the mass spectrometer used in all these papers). I also procured and supplied ion source components such as the modified sample cone assemblies, the modified source housing, the XY sample plate stage and the heated inlet assembly as described in the papers. I helped with the development and deployment of the Waters Research Enabled Software scripting software (WRENS) used. The Initial experiments to improve the multiply charged ion yield through optimisation of the heated capillary and counter flow "cone gas" are reported in this thesis and were later advanced and reported in the "Investigation and optimization of parameters affecting the multiply charged ion yield in AP-MALDI MS".[1] Other papers of relevance include, "Protein identification using a nanoUHPLC-AP-MALDI MS/MS workflow with CID of multiply charged proteolytic peptides", [2] "Production and analysis of multiply charged negative ions by liquid atmospheric pressure matrix-assisted laser desorption/ionization mass spectrometry"[3] and "Advancing Liquid Atmospheric Pressure Matrix-Assisted Laser Desorption/Ionization Mass Spectrometry Toward Ultrahigh-Throughput Analysis".[4] In addition, several patents and conference presentations were forthcoming from this research. Front pages from a selection of published granted patents and published patent applications are shown in the appendix.

1. Introduction

1.1 Biological mass spectrometry

The early days of mass spectrometry involved experiments to determine the nature of discharge tube "canal rays" or "anode rays" first observed by German physicists Plücker and Hittorf and then reported by Goldstein in 1876[5,6]. These new rays that were later determined to be positive ions appeared to travel in the opposite direction to cathode rays. About a decade after their discovery, Wien found that it was necessary to apply much stronger magnetic fields to deflect the rays compared to the cathode rays, he also found that they consisted of both charged and neutral particles. Wien was able to very approximately determine the mass-to-charge ratio of the deflected components. Thomson who had discovered the electron in 1897 continued to refine the instrumentation and went on to resolve the lightest of the canal rays, H^+ and H_2^+. The first mass spectrograph or spectrum was reported by Thomson in 1913.[7] Since the early discharge tubes, many differing ionisation sources and analysers have been developed and as a result, mass spectrometry has become an incredibly powerful analytical technique for measuring the molecular weight and abundance of a wide range of chemical classes.

Today, modern mass spectrometers are designed to very precisely manipulate ions in space and time using magnetic or electric fields in a way that generates a "mass spectrum" or two-dimensional plot of ion abundance versus mass-to-charge ratio (*m/z*). Mass spectrometry can also be used to determine the quantity of known materials or to identify unknown compounds within a sample. Analyte ions can be selected and activated in ways that cause them to break into their individual constituents thus enabling the elucidation of their chemical structures.

Mass spectrometer systems are often enhanced with liquid chromatography sample inlets providing separation of complex liquid sample mixtures prior to ionisation. Furthermore, ion mobility devices are also employed within mass spectrometer systems to separate complex

mixtures of gas phase ions based on their size and charge. Ion mobility is a powerful technique and is able to provide measurements of the collisional cross-sections of analyte ions within a mass spectrometer.

Mass spectrometry applications are diverse. For example, accelerator mass spectrometers can perform highly sensitive analysis of carbon-14 isotopes for microdosing studies[8] and at the other extreme of molecular size, charge detection mass spectrometers can measure the mass and charge of virus capsids in the gigadalton range.[9] Small molecules being developed by pharmaceutical companies are analysed both for efficacy and purity and there is an ongoing drive to acquire spectral information at faster and faster rates. Mass spectrometry imaging (MSI)[10] direct from surfaces is a rapidly growing field in which, for example, small regions of a biological tissue section are desorbed and ionised by a tightly focused laser whilst the mass spectrometer generates spectral information from the constituent analytes, pixel by pixel from the tissue. Each pixel of the image can be shown as a spectrum providing invaluable information. Ion imaging in this manner can be used to identify the location of a pharmaceutical drug within a biological tissue or to understand the fundamental biology of an organ, or even to quantify the extent of spatial spread of a cancerous tumour *in-vivo*.

A recent development, the intelligent knife[11] or "i-knife" is able to vaporise biological tissue in real time within the operating theatre and present the surgeon with clinical information such as the spatial extent of a cancerous tumour. Even though it may not be possible to identify every peak in a mass spectrum, quite often for a biological mixture of molecules the spectral pattern can be classified using data mining algorithms and principal component analysis (PCA).

Mass spectrometry analysis of peptides, carbohydrates, glycans is particularly important in the life sciences field. The identification and quantitation of peptides and proteins with their vast set of post-translational modifications is responsible for a large proportion of mass spectrometers sold. Despite the high analytical performance of modern-day mass spectrometers, it seems that the technical development of mass spectrometry and ancillary

equipment is still in its early stages with many innovative advances occurring every year. Extensive advances in sample preparation, purification of analytes through chromatography and ionisation continues at a pace. Mass analyser developments in terms of sensitivity and resolving power, ion detection and data analysis are achieving new levels of performance year on year. It is clear that mass spectrometry offers a direct benefit to society and its success as an analytical technique is reflected in the worldwide market sales estimated to reach over $5 billion in 2021.[12]

1.2 Electrospray Ionisation and MALDI Sources

1.2.1 Electrospray ionisation

Over the last three decades, the techniques of matrix-assisted laser desorption/ionisation (MALDI)[13,14] and electrospray ionisation (ESI)[15,16] have transformed the field of mass spectrometry, particularly in the analysis of larger biomolecules. This is primarily because of their "soft" nature and ability to generate ions from minute quantities of analyte molecules. In ESI, charged solvent droplets containing analyte ions are sprayed from a fine capillary towards the skimmer inlet cone (or "counter electrode"), of the mass spectrometer using the influence of an applied electric field (Figure 1).

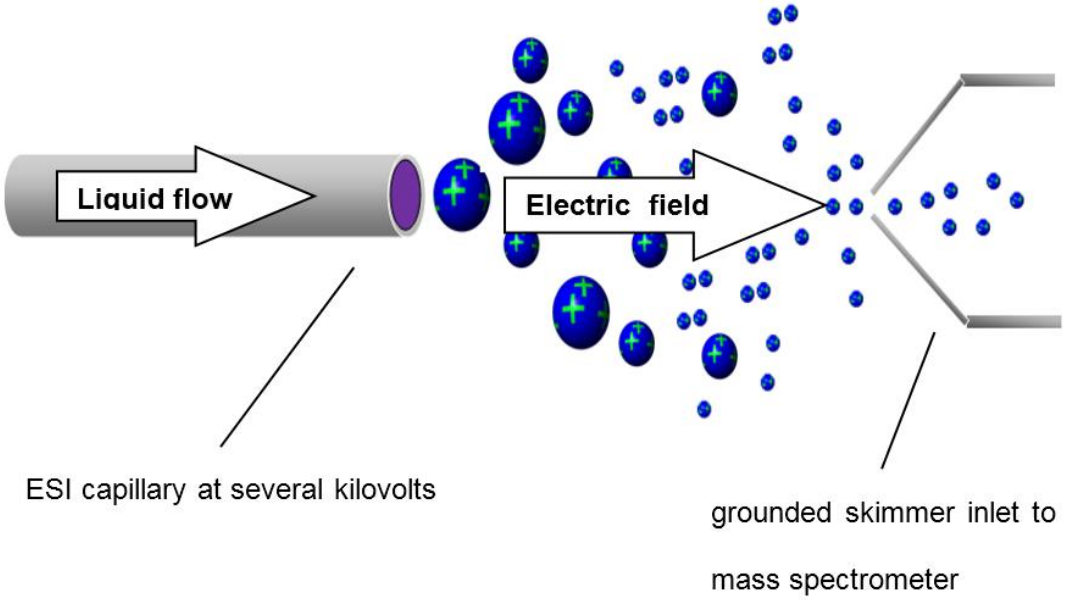

Figure 1: Electrospray ionisation – positively charged droplets are sprayed from a liquid flow exiting a capillary at a positive potential towards a grounded mass spectrometer skimmer inlet cone ("counter electrode"), the droplets evaporate and eventually lead to bare cations. Negatively charged droplets and analyte ions can be generated by reversing the potential differential.

As the droplets traverse the electric field, the solvent evaporates, ultimately generating a continuous stream of bare analyte ions. In ESI, charging of analyte molecules occurs within the liquid phase prior to the spraying of the charged droplets into the mass spectrometer inlet. Evaporation of the droplets leads to the formation of multiply protonated (or deprotonated) gas phase ions. Figure 2 illustrates two examples of multiply protonated ESI ions detected on a Synapt Q-Tof mass spectrometer from (a) - an infused solution of a small peptide, bradykinin, with a molecular weight of 1060 Da and (b) - a larger monoclonal antibody protein, trastuzumab (introduced using high performance liquid chromatography (HPLC)) with a molecular weight of ~145 kDa.

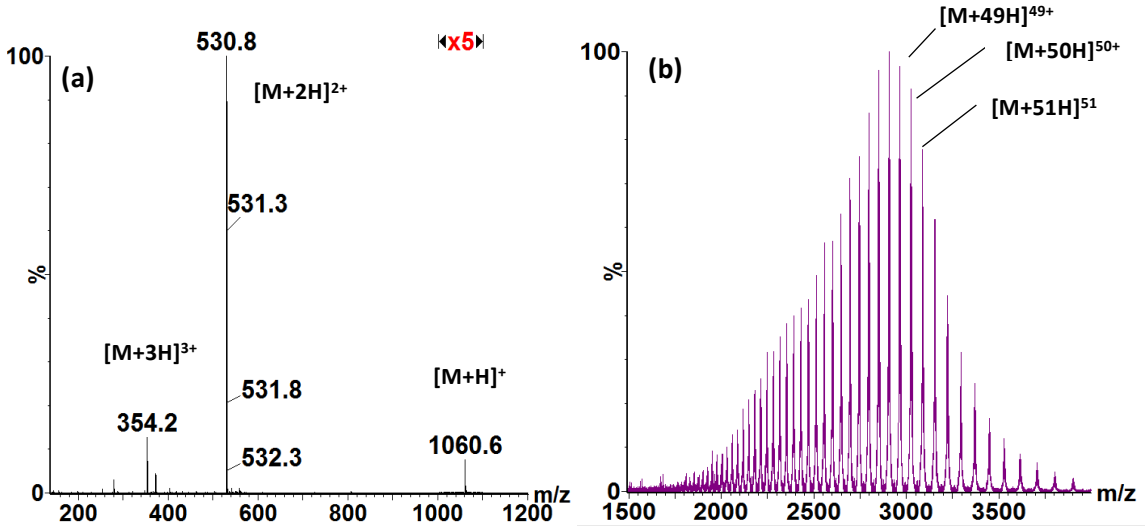

Figure 2: ESI spectra from a Q-TOF mass spectrometer showing multiply protonated peaks for (a) a peptide with a molecular weight of 1060 Da (bradykinin) and (b) a complete antibody of trastuzumab with a molecular weight of 145 kDa.

As the highly charged droplets evaporate and reach the Rayleigh limit[17], they undergo Coulomb fission thereby ultimately producing gas phase ions. There are two predominant models describing the generation of ions from droplets. The charge residue model (CRM)[18] and the ion evaporation model (IEM)[19]. In the CRM, fission provides a charged droplet with one (on average) analyte molecule which is released and picks up multiple charges from the droplet after the solvent evaporates. In the IEM model, the applied electric field is strong enough to desorb the molecular analyte ion directly from the droplet as it reduces in size. IEM generally applies to low molecular weight analytes whereas for large globular species the charged residue model (CRM) is followed. In addition to the CRM and IEM models, the chain ejection model (CEM) has also been proposed[20] and this applies to disordered analyte polymeric chains and involves the ejection of the unfolded chain of a (bio)polymer such as a peptide/protein from the shrinking droplet.

1.2.2 MALDI

Prior to MALDI, laser desorption/ionisation (LDI) mass spectrometers were developed in the 1970s primarily for analysis of small inorganic and organic molecules in the field of biomedical analysis[21,22]. Mixing the matrix with the analyte was a fundamental advance in softening the ionisation process allowing the intact analysis of more labile molecules and even large proteins beyond 100,000 Da[13,14]. In MALDI the conventional "dried-droplet" method employs a solid crystalline and UV light-absorbing matrix with the analyte embedded within it, in a large molar ratio (ca. 10,000:1; matrix:analyte). A small volume (typically one microliter) of a mixture of the solutions of matrix and analyte are deposited onto the surface of a metal sample plate where the solvents are allowed to evaporate leaving a thin layer of sample-matrix crystals. Thus, the analyte is co-crystallised in a UV light-absorbing matrix onto the surface of a sample plate electrode. A short (typically nanosecond) laser pulse is fired at the matrix/analyte mixture, resulting in desorption and ionisation of both the matrix and the analyte (Figure 3). For each laser pulse, a pulse of analyte ions is introduced into the mass spectrometer using electric fields in vacuum-MALDI, and mainly gas flow dynamics in AP-MALDI systems.

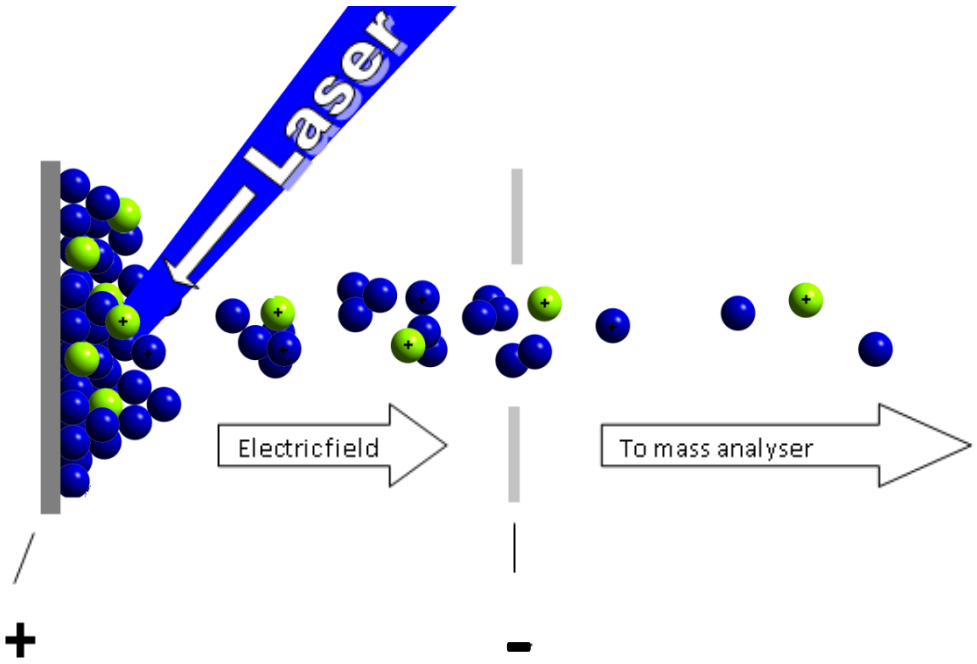

Figure 3: In MALDI, a short pulse of UV laser light, typically lasting a few nanoseconds, is focused to a small diameter (<500 µm) spot. The crystalline MALDI sample consists of a mixture of matrix and analyte. In positive ion mode, following desorption and ionisation, cations are extracted away from the positively charged sample plate towards the more negative inlet of the mass spectrometer.

Typically, ions generated following laser desorption from the solid crystalline sample-matrix surface are singly charged. The process of ion generation is still not fully understood or accepted by researchers [23]. Two theoretical models persist, the first is the gas phase protonation model [24] and the second is known as the "Lucky Survivor"[25]. In the gas phase protonation model, the radical matrix ions are formed initially via photoionisation from the laser. Subsequently, protonated and deprotonated matrix ions are generated through secondary reactions (eq. 1 to eq. 4). Within the plume, analyte molecules are assumed neutral and protons are subsequently transferred to/from the protonated matrix ions to the analyte molecules forming both anions and cations (eq. 5 and eq. 6).

$$matrix \xrightarrow{h\upsilon} matrix^{+\cdot} + e^{-} \ldots\ldots\ldots\ldots\ldots\ldots\ldots\ldots\ldots\ldots\ldots\ldots\ldots\ldots\ldots\ldots eq.\,1$$

$$matrix + e^- \longrightarrow matrix^{-\cdot} \ldots\ldots\ldots\ldots\ldots\ldots\ldots\ldots\ldots\ldots\ldots\ldots\ldots\ldots\ldots\ldots \text{eq. } 2$$

$$matrix^{+\cdot} + matrix \longrightarrow [matrix + H]^+ + [matrix - H]^- \ldots\ldots\ldots\ldots eq. 3$$

$$matrix^{-\cdot} + matrix \longrightarrow [matrix - H]^- + [matrix + H]^+ \ldots\ldots\ldots\ldots eq. 4$$

$$[matrix + H]^+ + analyte \longrightarrow matrix + [analyte + H]^+ \ldots\ldots\ldots\ldots eq. 5$$

$$[matrix - H]^- + analyte \longrightarrow matrix + [analyte - H]^- \ldots\ldots\ldots\ldots eq. 6$$

In the lucky survivor model, upon desorption, any pre-formed analyte ions and clusters are largely neutralised within the expanding plume through ion-ion reactions with clusters and/or photoelectrons. The remaining "surviving" ions are more likely to be singly charged than multiply charged as the ion-ion reaction cross section is dependent on the product of opposing charges squared and thus largely favours higher charged ions.[26] It is of course feasible that both models play a role[27,28]. Interestingly, the Zenobi group investigated the electrospraying of insulin under ambient conditions on to surfaces of conventional MALDI matrix. It was found that ions desorbed from the surface had retained, to some extent, their higher levels of charging [29].

1.2.3 Atmospheric Pressure (AP) MALDI

In 2000, atmospheric pressure MALDI (AP-MALDI) was described[30] and appeared to offer advantages over conventional MALDI ion sources that operated under vacuum. For example,

AP-MALDI ion sources did not require the engineering complexities of transporting the MALDI sample plate into the high vacuum region of the mass spectrometer. Furthermore, the analysis of more volatile samples became possible. Like conventional vacuum MALDI, AP-MALDI has also been used for the analysis of a wide range of sample classes including tryptic peptides, pesticides and oligosaccharides. AP-MALDI has also been used for MS imaging experiments.[31,32] Comparative studies of vacuum MALDI and AP-MALDI generally report at least an order of magnitude lower ion signal for AP-MALDI compared to vacuum MALDI[31, 33] and this is probably attributed to poor ion transmission from atmosphere to vacuum.

Generally, in most commercial mass spectrometers, as the *m/z* ratio increases, the ion generation, ion transmission and subsequent detection of ions becomes more challenging – this has rendered traditional singly charged MALDI sources at a relative disadvantage compared to ESI which produces higher charged ions and thus ions with lower *m/z* values. Despite several MALDI applications requiring the direct ionisation from surfaces, such as MS imaging, ESI, with its inherent generation of multiply charged ions, at low *m/z*, has dominated the MS market.

MALDI does however have various advantages over ESI. For example, sample preparation is fast and simple. It also lends itself to high-throughput analysis from robotically prepared high-density sample plates, and under certain conditions, ultimate detection limits are extremely low. Other advantages include the ability to provide ions from small and precise spatial locations for MS imaging (≤1µm as defined by the wavelength of the laser).[34] MALDI is also more amenable to analysis of mixtures than ESI and more tolerant to sample impurities and additives [35]. However, for ESI in particular, the problem of mixture analysis is largely solved by separating complex analyte solutions with high performance liquid chromatography (HPLC) prior to MS analysis, although at the expense of additional time and potential sample losses.

1.2.4 Liquid AP-MALDI and multiply charged ions

Typically, liquid matrices are composed of a chromophore (as is used in conventional dried-droplet crystalline MALDI), a proton-donating weak acid, a non-volatile liquid (such as glycerol) to maintain stability of the liquid phase solution and a more volatile solvent to enhance the mixing of all components.[36] Liquid matrices have been used both within vacuum and AP-MALDI sources, however the stability of the liquid droplet is easier to maintain at atmospheric pressure. Both IR and UV MALDI using liquid matrices have reported significant advantages over conventional crystalline MALDI.[37,38] For example, when the laser focus is positioned onto the sample/matrix droplet the "self-healing" properties of the liquid mean that from shot-shot, the intensity of ion the signals generated is very stable and several thousand laser shots can be fired at the sample before the droplet is depleted. Therefore, the mass spectrometer operator does not have to continuously move the sample plate relative to the laser whilst searching for so-called "sweet-spots" as is the case with crystalline MALDI.

The liquid format also facilitates on-target chemistries in which additional reagents can be added. For example, the broad tolerance of pH range within the sample/matrix allows tryptic digestion of the MALDI analyte and detection of its products.[39]

One significant difference between the conventional MALDI and ESI ionisation process is that the MALDI ions observed are usually singly charged while ESI ions show a charge distribution of mainly multiply charged ions. Researchers have been attempting to generate multiply charged ions using MALDI for several years.[29,40] Ideally, the higher charged MALDI ions would be generated at low laser fluence (with less sample wastage through ablation), high sensitivity and increased signal longevity. More recently, promising results have been published using a standard UV laser operating at low fluence in combination with a liquid matrix/sample.[41] The fluence reported was under 2000 J/m^2 which was substantially lower than laserspray ionisation[42] (described below) that reported typical fluences of 40-50 kJ/m^2. The impetus to generate multiply charged MALDI ions is not just because the lower *m/z* ions lend themselves

to analysis by established high-performance mass spectrometers, but also because multiply charged ions are more amenable than singly charged ions to fragmentation processes. In particular, ECD/ETD (described below) are advantageous for structural elucidation but require multiply charged cations.

1.2.5 Sonic spray, laserspray, solvent-assisted and matrix-assisted inlet ionisation

Similar to ESI, "sonic spray" involves spraying liquid droplets using a coaxial gas flow toward the inlet of the mass spectrometer but without using assistance from the electric field.[43] It generates both singly and multiply charged ions, either with or without a voltage applied within the liquid phase. (However, significantly more ions are generated when a voltage difference is applied within the sample liquid.) The charged ions observed are reported to come from the statistical imbalance and distribution of charges prior to downstream droplet disruption and shearing. [43,44]

Laserspray ionisation (LSI). [42] like conventional (solid-state) AP-MALDI, utilises a solid matrix. Singly charged species are often generated and multiply charged ions are also generated. Unfortunately, the laser fluence (laser pulse energy per irradiated area) required in this technique is large compared with liquid AP-MALDI. [42] It has also been shown that through the use of lower volatility matrices higher charged ions can be generated when sufficient desolvation energy is provided by the laser.[45]

Solvent-assisted inlet ionisation (SAII) [46] is a relatively simple technique, whereby a liquid analyte solution is introduced directly into the heated inlet capillary of the mass spectrometer. It produces multiply charged ions when droplets interact (and receive energy) from the heated capillary inlet surfaces. A characteristic "sizzle" sound is often heard preceding the detection of ions.

Matrix-assisted inlet ionisation (MAII)[47] is similar to laserspray ionisation, but with no laser desorption. Instead, the use of heat to vaporise the matrix or a mechanical disturbance causes the matrix/analyte to enter the MS inlet. Multiply charged ions are observed and the fracturing or shearing of the matrix/sample crystal is a possible theory for generating multiply charged ions in MAII.[44,48] Unfortunately, there appears to be limited control of these ionisation processes either spatially (for ion imaging) or temporally compared with MALDI, and sample consumption is high.

Both infrared (IR)[40] as well as UV[41] liquid AP-MALDI have been shown to generate multiply charged ions. The latter provided signals from lower (more analytically useful) sample concentrations and with conventional MALDI (dried droplet) fluence levels.

With all the above methods, there appear to be several features in common such as the heated inlet capillary, an electric field and liquid droplets. The process of droplet shearing as mentioned above[44], resulting in a net charge appears to be a common theme in these ionisation processes.

1.3 Mass Spectrometer Analysers

The results in this project were all obtained from an orthogonal time-of-flight (TOF) analyser fitted with a quadrupole (Q) mass filter for precursor ion selection. The system also included a stacked ring travelling wave ion mobility device positioned between the quadrupole and TOF analysers. It should be noted that the liquid AP-MALDI source might be easily adapted to fit on other types of analysers that are designed to use an AP ion source, for example, Orbitrap or FTICR systems. However, for this project, a Q-TOF system was used (Waters Synapt G2-Si, see Figure 4) to generate data. As such, the basic operation of the quadrupole mass filter, ion mobility separation and the TOF analyser are covered below. For context, a brief description of vacuum based MALDI mass analysers is also provided.

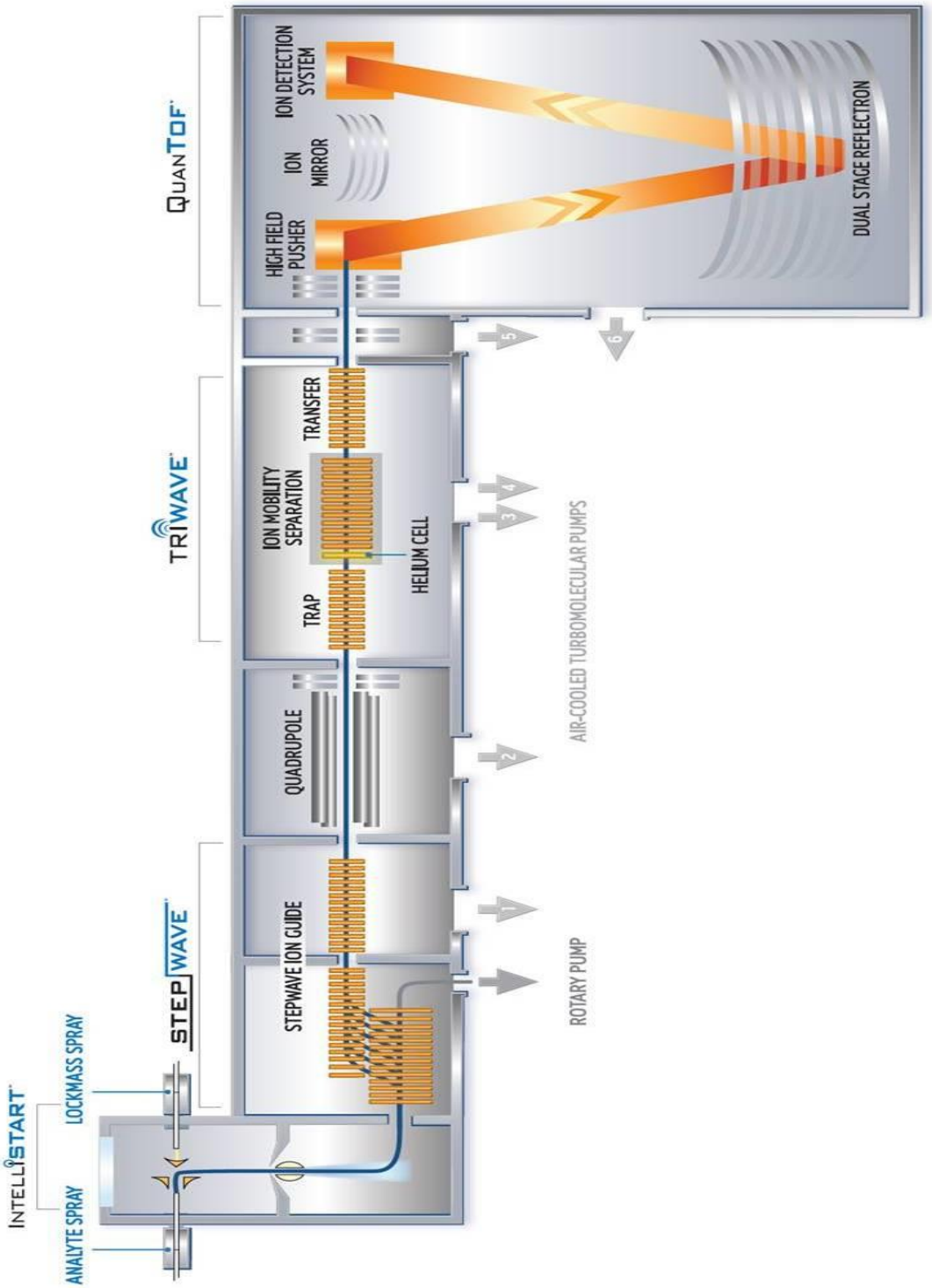

Figure 4: Schematic of the Synapt G2-Si HDMS (reproduced with permission from Waters Corporation).

1.3.1 The quadrupole (Q) mass filter

The quadrupole (Q) mass filter was developed by Wolfgang Paul's group[49] in the 1950s and is constructed with four highly parallel rods, ideally hyperbolic in shape but often circular for simplicity of manufacturing (see Figure 5 and Figure 6). Both radiofrequency (RF) and direct current (DC) potentials are applied to the rod set. Adjacent rods have opposing RF phases and opposing DC polarity applied. The spacing and diameter of the rods and the amplitude of the RF potentials applied are arranged to generate a harmonic pseudopotential well[50] in the XY plane. The stability of ions within a quadrupole mass filter can be seen graphically within the Mathieu stability diagram shown in Figure 7.

The Mathieu stability diagram is useful for determining the range of *m/z* values that are transmitted through the device and is derived from the differential equations of motion in the quadrupolar and DC fields in which ions have stable trajectories. The vertical axis of the stability diagram is proportional to the DC applied and the horizontal axis is proportional to the RF applied. Both axes of the stability diagram are inversely proportional to the *m/z* of the ion so for a given RF and DC potential a range of *m/z* values along the line in the shaded region are transmitted.

Without DC applied to the rods, the quadrupole is known to be operating in RF-only mode and is often used as an ion guide within mass spectrometers. However, in RF-only mode lower *m/z* ions become unstable below a certain value as their amplitude of oscillation becomes so large that they collide with the rods. Higher *m/z* ions with excess radial kinetic energy are also able to escape the pseudopotential well (as its strength is inversely proportional to *m/z*)[51] but the loss of higher *m/z* ions is not such an abrupt cut off and is determined by the distribution of their kinetic energy distribution. It can be seen from the stability diagram that applying DC to the rods introduces a more defined cut off for higher *m/z* ions and the combined effect of RF and DC results in a device able to filter ions based on a narrow *m/z* window.

RF-only rods first developed by Brubaker[52] are usually fitted at the entry and exit of the quadrupole and ensure efficient transmission of ions into (and out of) the device.

Despite the quadrupole mass analyser having a low duty cycle compared to TOF mass analysers (i.e. most of the ions are rejected by the device), it is well suited to select ions of interest for dissociation and analysis. Within the Synapt, the quadrupole is used for precursor *m/z* selection so that the specific ions of interest are subsequently dissociated via collision-induced dissociation (CID) or electron transfer dissociation (ETD) within the trap cell. Ion mobility of the product ions can be carried out, alternatively, CID product ions can be generated after ion mobility of the precursor ions (with or without prior quadrupole selection). In this project a prototype device for electron capture dissociation (ECD) was fitted after ion mobility.

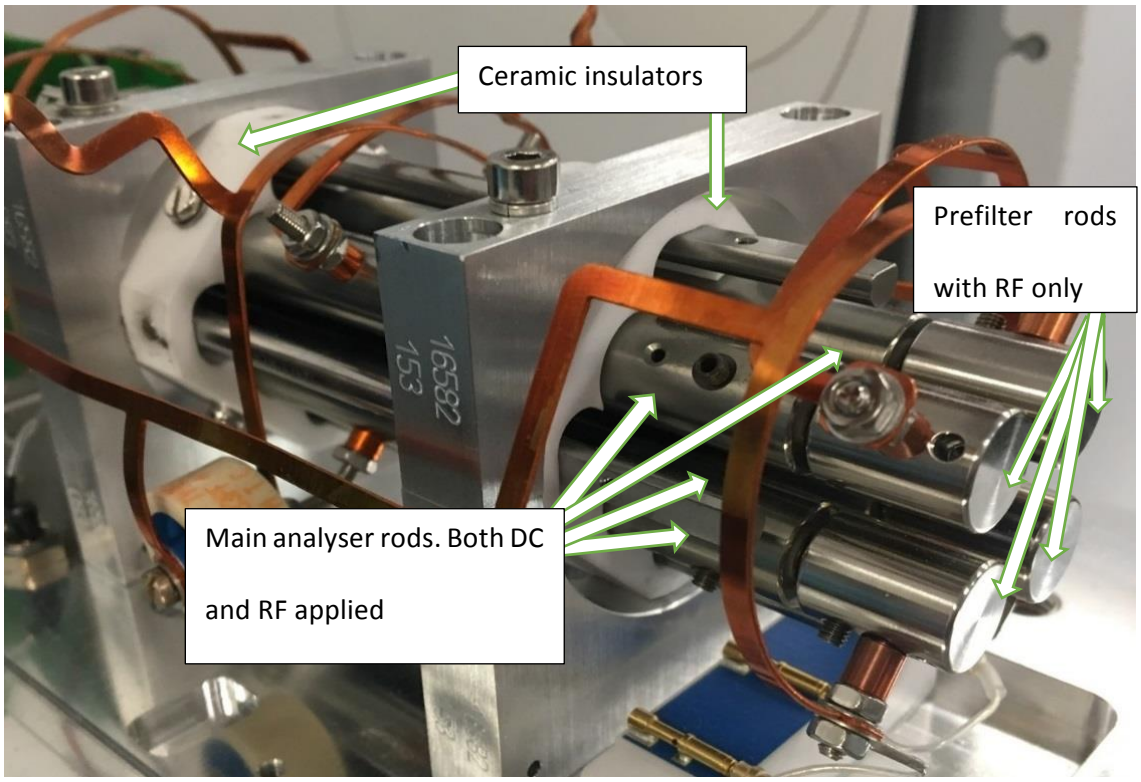

Figure 5: A Waters quadrupole mass filter showing the four rods mounted within ceramic insulators. At each end of the device the four rods are split and only the RF voltage component is applied. These RF-only rods first developed by Brubaker[52] are called pre and post filters and they ensure efficient transmission of ions into (and out of) the device.

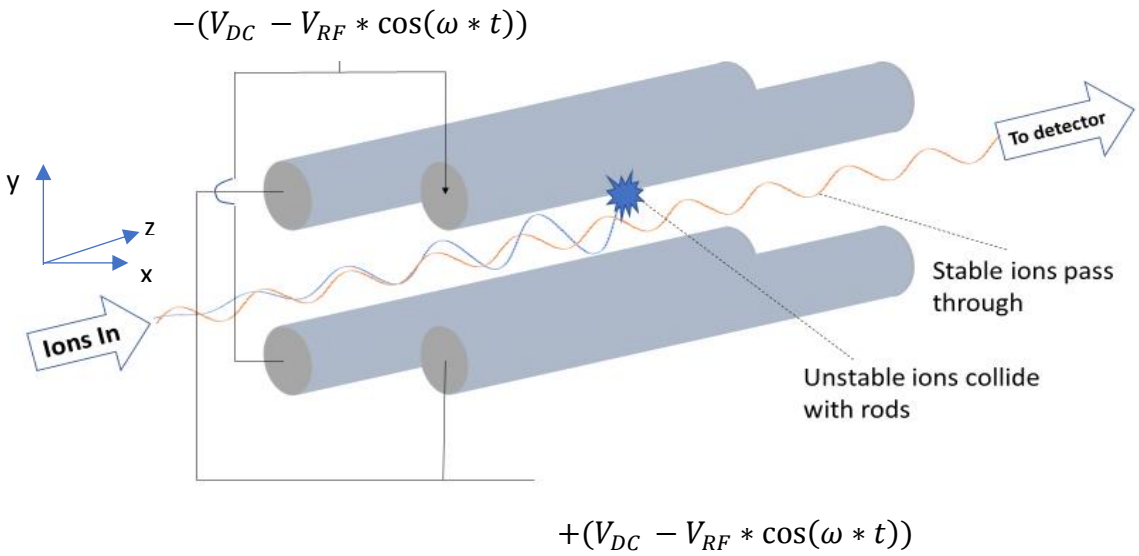

Figure 6: A quadrupole mass filter is composed of four cylindrical rods with opposing phases of RF applied to adjacent rods. A superimposed DC voltage is also applied to adjacent pairs of rods which causes specific ions to become unstable in the xy plane and to strike the rods.

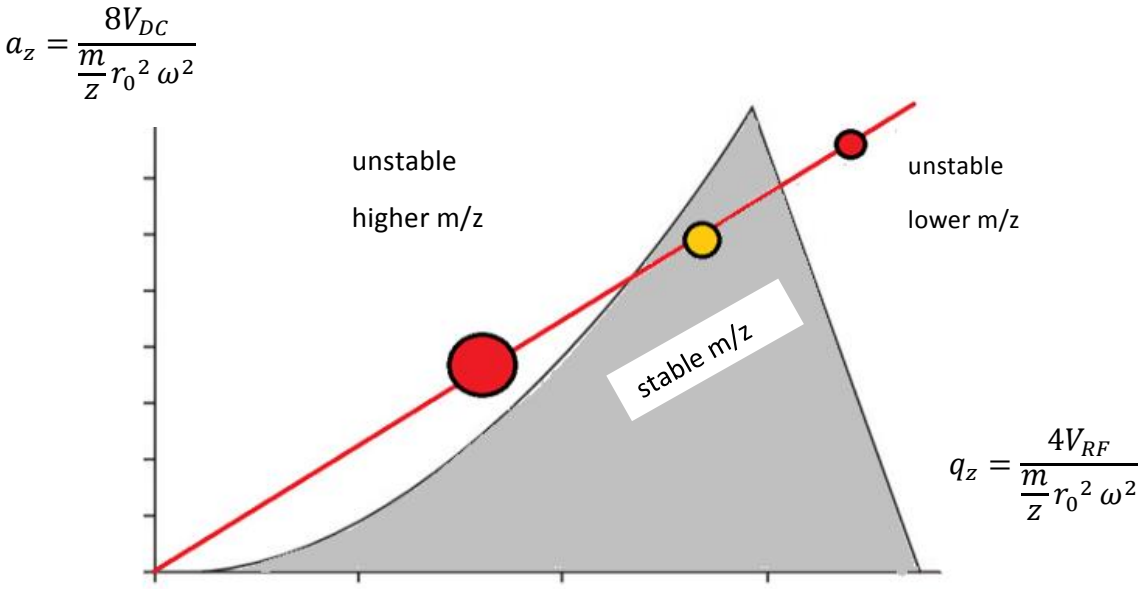

Figure 7: The Mathieu quadrupole stability diagram. Ions in the shaded region remain within the confines of the rods and are transmitted through the device. The x-axis is proportional to the V_{RF} applied and the y-axis is proportional to the V_{DC} applied, both axes are inversely proportional to the m/z. (For q_z and a_z V_{RF} is the amplitude of the RF voltage applied, ω is the RF angular frequency, V_{DC} is the DC voltage applied and r_0 is the inscribed radius between the quadrupole rods.)

1.3.2 RF multipole ion guides

Mass spectrometer ion guides are required to efficiently collect and transport ions from the ion source into the vacuum as well as between discrete devices within the vacuum system. RF ion guides are often partially filled with a collision cooling gas such as argon at approximately 10^{-2} mbar. For guides directly preceding an orthogonal TOF mass analyser the cooling gas acts to dampen the kinetic energy of ions, thus providing a pre-conditioned ion beam with reduced energy spread in the TOF direction. This is advantageous as a reduced energy spread requires less energy correction leading to higher ultimate resolving powers. Another aspect of collision gas is that if the incoming axial kinetic energy of ions is increased then CID occurs. The product ions generated are radially contained and also transmitted with reduced energy spread into the downstream TOF mass analyser.

The quadrupole rod set described above when operating in RF-only mode without the mass resolving DC is one common form of RF ion guides in which the pseudopotential (or effective potential) generated by the device is proportional to the radius squared. Other RF multipole guides utilising more rods are often used as their ion transmission characteristics may be more suited to a particular function within the system (Figure 8). For example, multipoles of higher number have flatter central pseudopotential profiles and can accept (and emit) wider diameter beams. In RF multipole rod guides there is no axial thrust to keep ions moving through the guide, this can become problematic when collisional cooling gas is admitted as it causes ions to travel very slowly or even become stationary along the device depending on the ion flux and space charge. This has detrimental consequences when, for example, the mass spectrometer is running a fast multiple reaction monitoring (MRM) experiment as crosstalk between transitions might be observed.

In the Synapt Q-TOF mass spectrometer most of the RF ion guides are constructed from stacked rings with adjacent phases of RF applied to adjacent plates. It can be seen from Figure 8 that the effective potential (or pseudopotential) for the stacked ring guide is significantly flatter than a quadrupole, hexapole or octopole device.[51] In the Synapt, the stacked ring ion guides also include "travelling wave" DC potentials superimposed onto the rings and the potentials are arranged to drive ions axially in a very controlled manner[53]. This not only overcomes the crosstalk problem described above but with additional gas can be used to separate ions according to the collision cross section and this functionality is at the heart of the ion mobility cell within the Synapt[54].

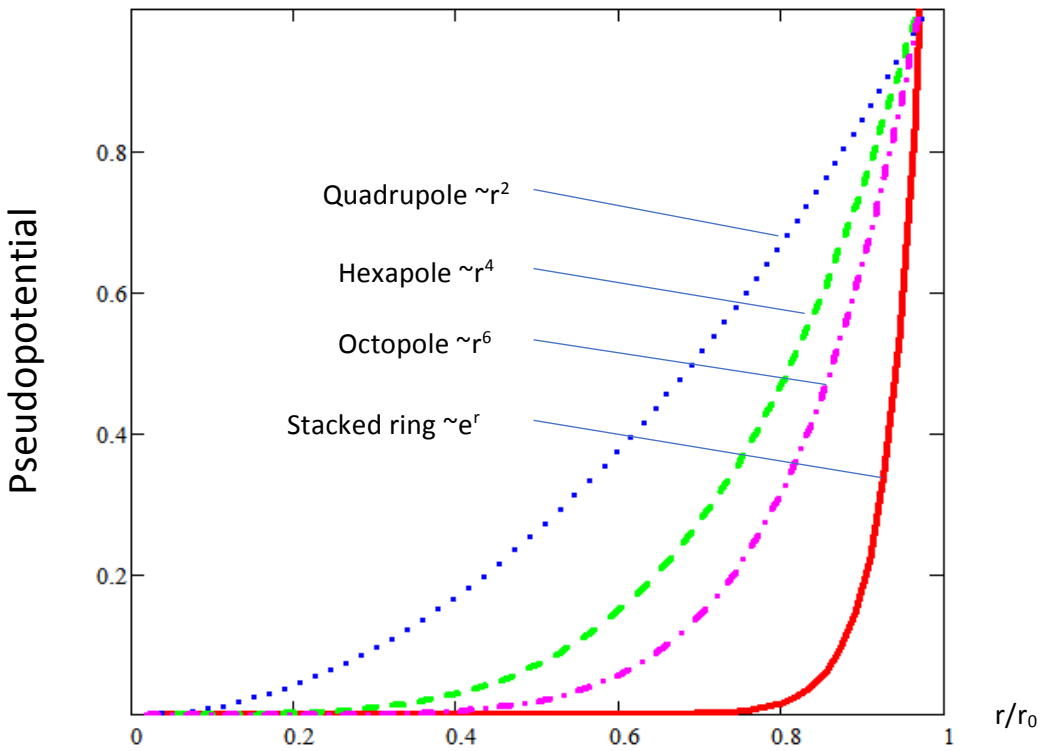

Figure 8: The effective potential (pseudopotential) normalised for different RF ion guides as a function of ion radial location r (divided by r_0) for a quadrupole, hexapole, octopole and stacked ring ion guide[51]. Where r_0 is the effective inscribed radius of the multipole rods or rings defining the physical extent of ion motion (e is the mathematical constant 2.718).

1.3.3 Ion mobility within traveling wave ion guides

Within the ion mobility cell, pulsed DC potentials are applied to the rings as shown in Figure 9(b). The traveling wave DC pulses drive ions axially along the device. When the device is pressurised with gas such as nitrogen at a few mbar the smaller (cross section) ions with higher charges tend to "surf" along more often with the traveling wave potentials, whereas larger ions or ions carrying less charge fall behind the traveling wave fronts. On average drift times are very closely related to the collision cross section and charge. The separation of ions according to their collision cross sections and charge provides an effective way of increasing the spectral signal to noise through summation of spectra in which the mobility drift times are associated with the analyte of interest. In addition, through calibration of the drift times (using standards) through the IMS cell, the collision cross section of an ion can be determined.

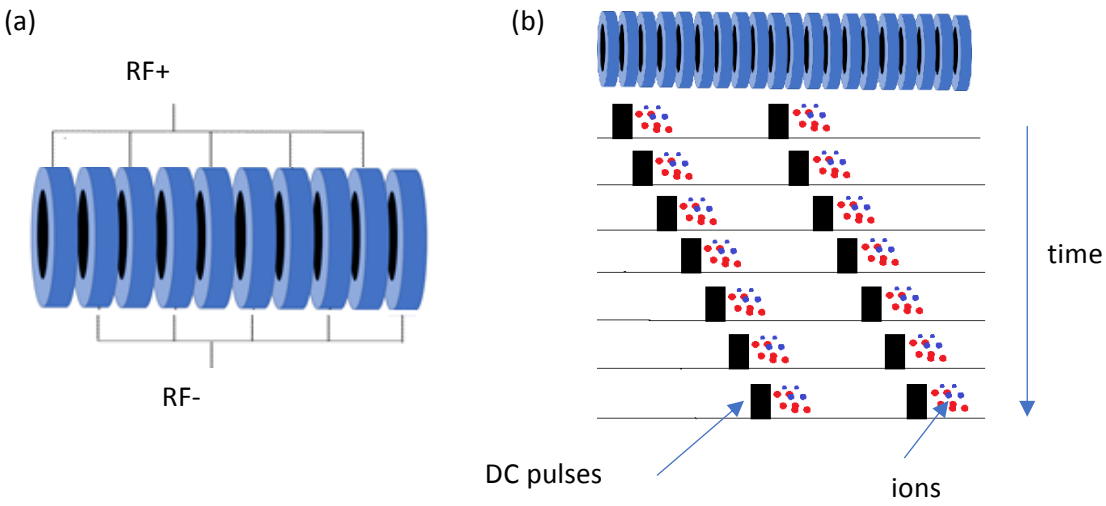

Figure 9: Schematic of stacked ring ion guide (a) where adjacent rings are connected to opposing phases of RF potential. In addition to the RF, DC travelling wave pulses are superimposed on the rings causing ions to be driven axially along the guide (b). [54]

1.3.4 Time-of-flight (TOF) mass analysers

Once ions have been generated and introduced into the vacuum it is possible to accurately measure the time of flight of ions to fractions of a nanosecond. Ions are first accelerated using

an electric field with potentials typically between 5kV and 20kV across distances of a few centimetres, ions then enter a field-free drift region. The drift region may be at ground potential with the ion source floated at the accelerating voltage, alternatively it is sometimes convenient to have the ions source close to ground potential and then to float the drift region (field free region) at a high accelerating voltage. The polarity of the electric field defines whether anions or cations are to be analysed. From the start time of the acceleration to the stop time at the detector is the measured time of flight. Heavy ions have the same kinetic energy as light ions of the same charge. The energy equation states:

$$\frac{1}{2} * Mass * Velocity^2 = z * Acceleration\_Volts \ \ldots\ldots\ldots\ldots\ldots\ldots\ldots\ldots\ldots. eq\ 7$$

For the distance of the field-free drift region:

$$Velocity = \frac{Distance}{TOF} \ldots\ldots\ldots\ldots\ldots\ldots\ldots\ldots\ldots\ldots\ldots\ldots\ldots\ldots\ldots\ldots\ldots\ldots\ldots\ldots.\ldots\ldots\ldots eq\ 8$$

where the ion has the *Velocity* (m/s) defined by the *Distance* (m) and *TOF* (s).

Rearranging this equation results in:

$$TOF = Distance * \sqrt{\frac{\frac{m}{z}}{2 * Acceleration\_Volts}}. \ldots\ldots\ldots\ldots\ldots\ldots\ldots\ldots\ldots\ldots\ldots\ldots eq\ 9$$

where the ion has the mass *m* (kg), charge *z* (C), *Distance* (m) and *Acceleration_Volts* (V) as the potential difference that the ions are initially accelerated through. When ions fly through regions with electrostatic fields such as the acceleration region of an ion source or a reflectron device (see below) the time-of-flight equation becomes more complex and depends on the geometry and magnitude of the fields. However, for simplicity the “Distance” term in

equations 8 and 9 can be viewed as the effective flight path that the ions traverse within a system even when multiple electrostatic fields are included.

K can be defined as an instrument constant determined by the physical geometry of the complete system and the voltages applied. The basic TOF equation is as follows:

$$\frac{m}{z} = K * TOF^2 \quad \text{.....eq. 10}$$

Practically, the TOF equation is only used to determine approximate *m/z* measurements. The *m/z* axis can be more accurately calibrated to higher order by measuring the TOFs for set of calibrant peaks with known masses as described in Chapter 2.

Differentiation of equation 10, provides the mass resolving power for a given time aberration within a TOF system is:

$$Resolution\ (FWHM) = \frac{m}{\delta m} \approx \frac{TOF}{2 \cdot \delta TOF} \ldots\ldots\ldots\ldots\ldots\ldots\ldots\ldots\ldots\ldots\ldots\ldots\ldots\ldots\ldots eq\ 11$$

The various uncorrected TOF aberrations in the system (δTOF) accumulate (for an ion population), leading to a broadening of the peak of ions with the same *m/z*. δTOF can be considered as the sum in quadrature of all the TOF aberrations in a system.[55]

At each stage within the TOF analyser, careful attention is paid in the design to reduce aberrations so that the highest resolving power can be achieved within the constraints of instrument size.

There are several contributions to the aberrations, a few of which are listed as follows:

- Turn-around time (twice the velocity difference divided by the ion acceleration) is the time-of-flight difference between two isobaric ions that are initially moving in opposing directions in the orthogonal acceleration field.
- Timing errors associated with both the ion detection system as well as the digital recording circuitry that determine the ion peak arrival times (analogue to digital converters (ADC) or time to digital converters (TDC)).
- Flatness of the microchannel plate (MCP) or conversion dynode detector surface can be relevant as differing path lengths to different points on the detector can introduce a time of flight variation.
- Variations in kinetic energy of ions due to power supply voltage ripple or thermal drift.
- In gridded TOF assemblies, electric field boundaries are defined by grids. However, the small apertures existing between grid wires act as tiny ion lenses causing variation in ion velocity.[56]

1.3.5 Reflectron systems

Ion mirrors, also called reflectrons in mass spectrometry, were reported by Mamyrin in 1966[57] and increase the mass resolving power for two reasons. Firstly, they increase the effective path length and time of flight for a given *m/z*, as such, aberrations (such as peak timing jitter or turn-around time described above) become a smaller proportion of the overall flight time. Secondly, reflectrons cause isobaric ions of higher kinetic energy to spend longer within the reflectron than ions of lower energy. The increase in the time of flight within the reflectron for the higher energy ions is arranged to exactly compensate for the shorter time of flight within the field-free regions (exterior to the reflectron).

Reflectrons also provide an additional degree of freedom in the design of the TOF geometry. The first time-of-flight focal plane acts as a virtual source of ions for the reflectron device and

with higher orthogonal extraction fields the focal plane can be located much closer to the extraction electrodes than for “linear” (non-reflectron) TOF systems. The higher orthogonal extraction field is very advantageous as it reduces the turn-around-time aberration. Multiple field regions within reflectrons as well as multiple stages of acceleration fields are often utilised in modern TOF systems to achieve higher-order spatial focusing and improved resolving power.[58]

1.3.6 Linear and reflectron-based MALDI-TOF systems

Differences between the techniques of AP ESI and vacuum MALDI have led to divergent instrument designs. Systems known as “linear” TOF MALDI mass spectrometers exist in which the detector is positioned in-line with the initial ion direction (Figure 10). Alternatively, in reflectron-based MALDI-TOF mass spectrometers the detector is positioned after ions are reflected by an ion mirror (Figure 11). Such linear or reflectron MALDI-TOF mass analysers operate at pressures of ~10^{-7} mbar and are ideally suited to the pulsed nature of the MALDI process and the technique of delayed extraction[59]. For MALDI the development of delayed extraction provided significant enhancements in mass resolving power. After laser desorption/ionisation ions are allowed to expand towards the TOF analyser in an electric field-free region according to their initial velocity distributions, typically at velocities up to approximately 1000 ms^{-1} (depending on the matrix). After a delay of a few hundred nanoseconds the electric field is applied to accelerate ions from the source, this is arranged to cause isobaric ions with low velocities to catch up with ions of higher velocities, which are less exposed to the electric acceleration field. The pulsed electric field in delayed extraction which can also act as the start time for the time-of-flight digitiser clock. Pulsed electric field parameters for TOF were originally developed by Wiley and Mclaren[60] in 1955 and provided the basis for many of the present day commercial TOF instruments.

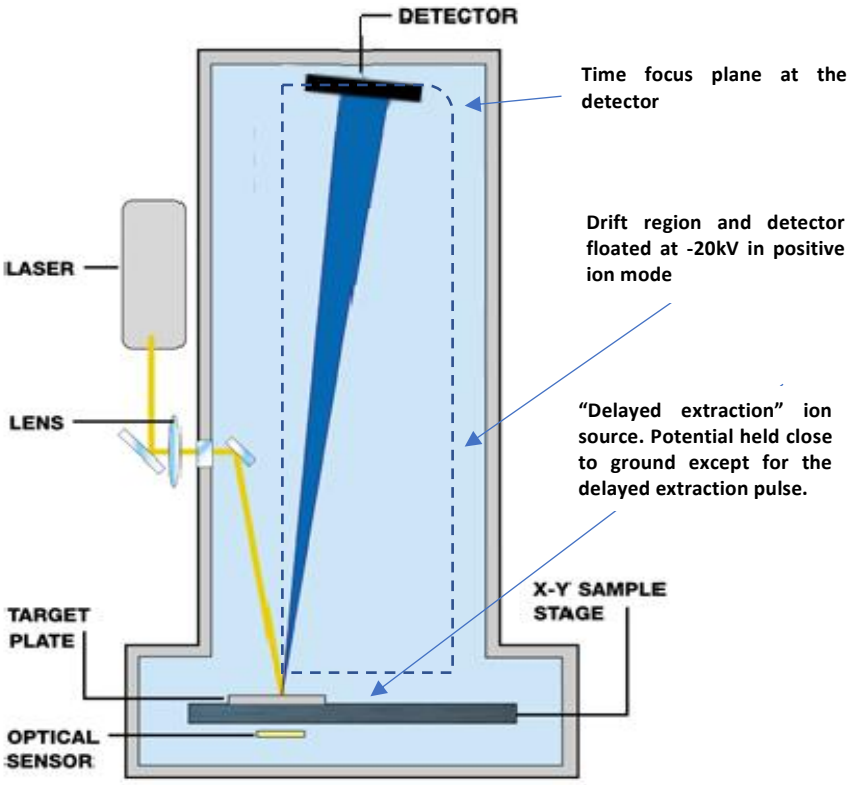

Figure 10: Schematic of a linear axial vacuum MALDI-TOF instrument where for cations -20kV is applied to the drift region while the target plate is held close to ground potential. The "optical sensor" is used to provide the spatial position of the XY stage. (Figure reproduced and modified from M@LDI Micromass Operators Guide).[61]

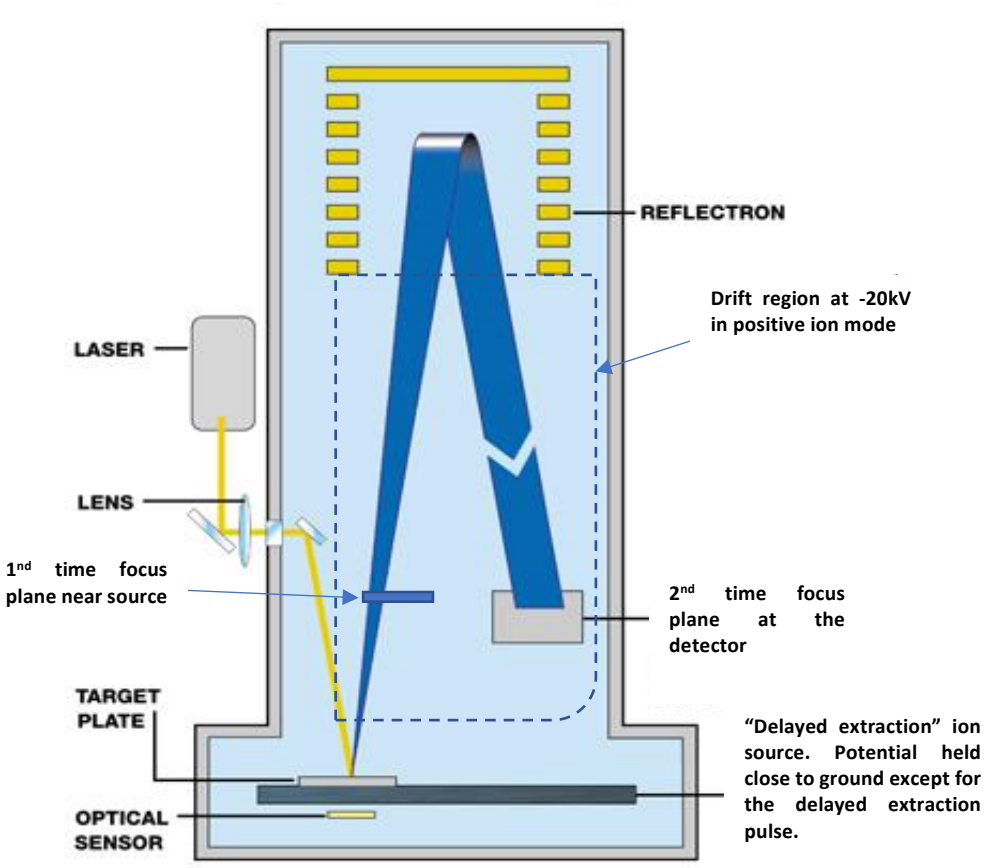

Figure 11: Schematic of a reflectron-based axial vacuum MALDI-TOF system. As in the linear version, the drift region is held at -20kV and the target plate is held close to ground potential. The rear of the reflectron is also held at a potential slightly higher than ground and reverses the direction of ions. Ions of the same m/z but differing energies arrive at the detector at the same time. (Figure reproduced and modified from M@LDI Micromass Operators Guide).[61]

1.3.7 Orthogonal TOF mass analysers

Axial TOF mass analysers (where the ions travel linearly along an ion optical axis) are well suited to pulsed ionisation sources such as (vacuum) MALDI sources with delayed extraction. However, such analysers are not very compatible with the continuous beam of ions generated from an AP ESI source. Orthogonal acceleration TOF (oa-TOF) mass analysers were developed in the 1980s to accept and analyse continuous beams of ions. In these systems a portion of

the ions are accelerated orthogonally to their direction of introduction into the TOF mass analyser region.[62,63]

Figure 12 depicts a schematic of an early example of an oa-TOF constructed by Dawson, in which ions from a continuous electron ionisation source were analysed. Oa-TOF systems can analyse ions from a large variety of continuous beam ion sources as well as pulsed ion sources such as AP-MALDI and now liquid AP-MALDI.

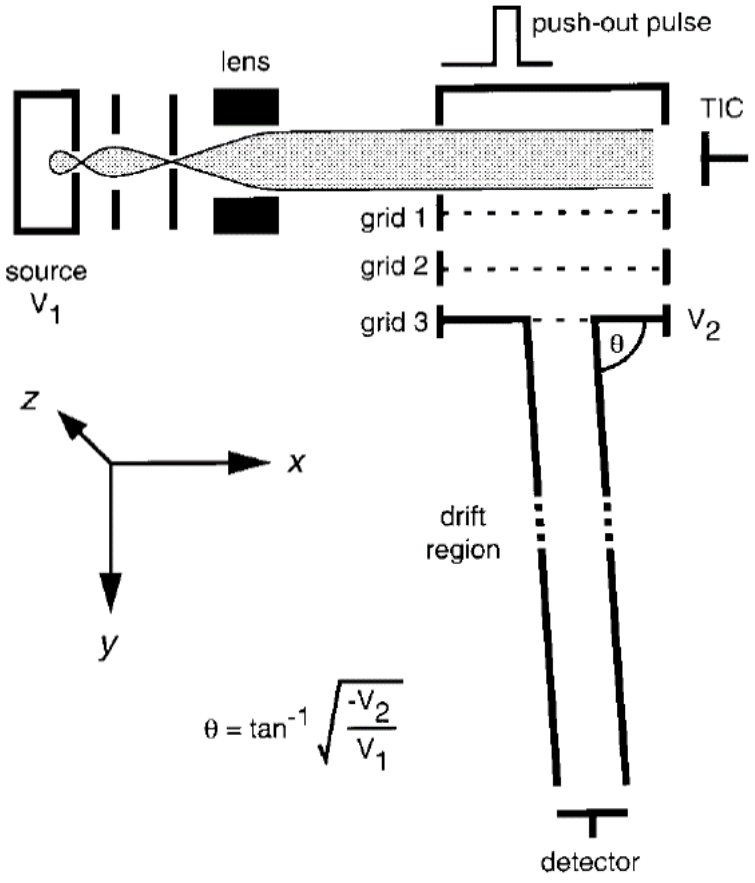

Figure 12: Schematic of an orthogonal TOF mass spectrometer where a continuous beam of ions from an electron ionisation source is periodically pushed-out with a pulsed acceleration field orthogonally towards a TOF drift region and detector ("push-out pulse"). V1 and V2 are the axial and orthogonal accelerating voltages and Θ is the angle of flight after acceleration into the drift region (Reproduced from Dawson & Guilhaus, 1989 with permission from John Wiley and Sons).[63]

In ESI oa-TOF systems the beam of ions is sent orthogonally to its initial direction with a pulsed electric field. The initial ion velocity distribution (in the orthogonal direction) is largely thermal in nature (provided that sufficient collisional cooling has been provided in the adjacent upstream ion guide). The electric field is designed to cause ions of the same *m/z* to arrive at a spatial plane at the same time irrespective of their original spatial locations. The ion detector is placed at the time-focus plane. This is known as spatial focusing and higher-order spatial focusing can be achieved resulting in resolving powers approaching one hundred thousand (FWHM) in commercial systems.[64] Other non-commercial systems utilising multi-reflection of the ions with gridless ion mirrors (reflectrons) have been developed, such systems have significantly longer flight paths and have achieved close to one million resolving power. [65]

1.3.8 Ion detection and mass range considerations

Once ions have traversed the system of electric fields and field-free regions in a TOF mass spectrometer they need to be detected with minimal time aberrations and over a wide dynamic range of ion pulse populations to maintain quantitative performance. A pulse of ions in a TOF mass analyser carries insufficient charge to be easily measured directly with a Faraday plate alone. Therefore, detectors usually incorporate secondary electron multipliers that are able to detect single ions. In these detectors, after an ion impacts a primary emission surface, secondary electrons are released and amplified. Devices such as discrete dynode multipliers[66] and microchannel plates (MCP)[67] are often used because the primary strike surface is very flat and the electron output signals generated are fast (with sub-nanosecond timing aberration). MCP detectors can amplify the electrical signals form the ion charges by gain factors of greater than one million. The output of an MCP or electron multiplier device is followed by high-bandwidth amplification circuitry and digital recording using analogue-to-digital convertors (ADC) or time-to-digital convertors (TDC) detectors. Unfortunately, the secondary electron yield from the primary strike surface reduces very steeply with ion velocity (approximately to

the fourth power) this means that slower moving larger ions produce significantly fewer ion counts than smaller ions. This partly explains why most mass spectrometers do not perform well for the detection of high *m/z* ions. Researchers are attempting to find other types of detectors such as "superconducting tunnel junction detectors" which are not limited by the same electron emission processes.[68]

The other limitation for high *m/z* ions stems from the transmission through RF ion guides. In particular, the depth of the pseudopotential well defining the ion guide can be too low for high *m/z* ions, (as described above). This relatively poor mass spectrometer performance at higher *m/z* underlines one of the aims of this thesis which is to enhance the performance of MALDI by enabling the generation of multiply charged ions (thus lowering the analyte's *m/z* for the same molecular weight).

1.4 Tandem Mass Spectrometry

Tandem mass spectrometry (MS/MS) involves the selection of a precursor analyte ion of interest using a first stage mass spectrometer MS1 (for example the quadrupole in a Q-TOF instrument) followed by a form of ion activation (for example CID) to generate product ions. The product ions are then analysed by a second stage mass spectrometer MS2 (for example the TOF mass analyser in a Q-TOF instrument). The two stages of tandem mass spectrometry can be performed either in the same analyser at different times (such as within an ion trap) or within sequentially coupled analysers, such as the Q-TOF or triple quadrupole (QqQ) systems.

MS/MS is a powerful technique in many applications. For example, in proteomics peptide fragment ions can be used to determine the sequence of a peptide *de novo* by predicting and

matching expected peaks within a spectrum. Alternatively, fragment ion spectra from peptides can be matched against databases to identify the protein of origin.

Product ions produced through MS/MS provide high specificity for the detection or quantitation of analytes often present in low amounts among chemically complex matrices. This specificity is often exploited using triple quadrupole (QqQ) mass analysers. The first quadrupole selects the precursor, the second quadrupole is for ion activation only (usually by CID) and the third quadrupole is programmed to monitor specific *m/z* fragment ions with high sensitivity and is often used for targeted quantitation or trace detection within the pharmaceutical industry.

MS/MS of ions using collision-induced dissociation (CID) is the default type of fragmentation employed in most commercial mass spectrometers. CID provides valuable information about the molecular constituents and sequence/structure of a preselected ion. CID involves one or multiple collisions of the precursor ion with an inert gas (such as argon). During the collision process, the internal energy of the precursor ion becomes high enough to cause fragmentation. Each collision increases the internal energy of the precursor ion. It is a relatively slow heating process, distributing energy across the ion whilst allowing time for rearrangements of the structure often causing cleavage of weaker bonds. Importantly, CID is also assisted by the coulombic repulsion of the charges.[69] Therefore, in CID, higher charged precursors usually provide richer, more informative spectra.

Typically, in ESI-based proteomics workflows, trypsin-digested proteins are identified by LC-MS/MS experiments. A limited number of precursor ions of interest can be determined and analysed automatically via data-directed acquisitions (DDA) on-the-fly, or via pre-programmed targeted lists. More recently, data-independent acquisition (DIA) workflows have been developed to avoid limitations of the DDA algorithms in determining the precursors. One such DIA workflow is termed “SONAR” (provided by Waters on Xevo Q-Tof systems),[70] in

which the quadrupole *m/z* value is very quickly and repetitively scanned during the LC peak elution. In addition, for alternate scans, the CID is switched between low and high energy fragmentation modes (by changing the collision energy). DIA techniques provide a comprehensive and unbiased workflow in proteomics and lipidomics and are more suited to discovery-based analysis and quantitation.

More recently, electron-based fragmentation techniques have been developed, in particular for biomolecule ions, such as electron capture dissociation (ECD)[71,72] and electron transfer dissociation (ETD). [73,74–80] These techniques involve fast, localised transfer of energy to the precursor and generate fragment ions that remain bonded with post-translational modifications (unlike in CID where modifications are often lost from the precursor and product ions). Furthermore, peptide fragmentation data using ETD or ECD are often easier to interpret as the peptide fragment ions are generated from more randomised backbone cleavages often covering the peptide sequence much better. Most importantly, in the context of this research, the singly charged ions generated from conventional MALDI sources are unviable for ETD or ECD because the transfer of an electron to the analyte cation simply neutralises the precursor rendering the neutral products undetectable in the mass spectrometer.

There is also resurgence of interest in techniques such as ultraviolet photo-dissociation (UVPD) and infrared multiphoton dissociation (IRMPD) by illuminating precursor ions with an appropriate source of laser light. [81–83] These complementary ion activation and dissociation techniques can provide the researcher with fragment ions that originate from different pathways that may not be observed using CID.[84] For example, referring to Figure 13, a, b and y type fragment ions are usually generated via CID (and IRMPD), whereas for the electron-mediated techniques, ETD and ECD, c and z ions are predominant. For UVPD, depending on the wavelength, a combination of vibrational and electronic fragment ions may be observed

but the prominent fragment ions are the a and x type ions (but with some b and y type ions present from vibrational activation).[85]

The nomenclature for different fragment ion types of peptides was suggested by Roepstorff[86] and then further modified by Johnson[87] (see Figure 13). Ions need to carry at least one charge to be detected. If the charge is held on the N terminal fragment it is denoted as either a, b or c. If the charge is on the C terminal, the ion type is x, y or z. The subscript indicates the number of residues in the fragment. Apostrophes to the right (or the left) of the letter represent when hydrogens are transferred to (or lost) respectively (for example, y_2" includes 2 additional hydrogens).

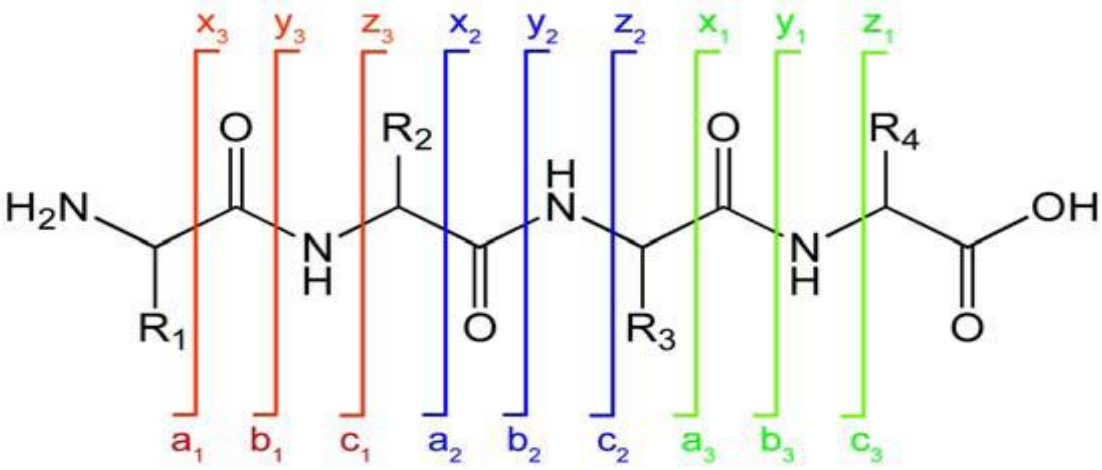

Figure 13: The nomenclature of peptide fragments as suggested by Roepstorff and Johnson.[86,88] a, b and y type fragment ions are often observed from low energy CID whereas c, and z ions are typical of ETD and ECD techniques.

1.5 High-speed sample throughput

One of the earliest TOF mass spectrometers was reported by Stephens in 1946 [89] and at that time he certainly recognised that "rapid analysis" would be one of its advantages compared with other types of analysers. This is still the case today as the mass resolving power obtained per unit time for TOF mass analysers far exceeds other types of modern mass analysers

including orbital trapping instruments ("Orbitrap") or Fourier transformation ion cyclotron resonance (FTICR) instruments that require significantly longer ion trapping times to obtain the same performance.

High-throughput sample analysis is often carried out using either ESI or conventional dried-droplet MALDI ion sources. In MALDI, application areas include bacterial identification [25] and single nucleotide polymorphism (SNP) analysis.[90] The limiting factor with ESI is bringing the samples into the ionisation region. For MALDI, this is less of a problem as the samples and matrix can be robotically prepared off-line, allowed to dry down and automatically loaded into the mass spectrometer. More recently, acoustic mist ionisation (AMI)[91] and desorption electrospray ionization (DESI)[92] techniques have shown promising results for high-speed throughput operating at 3 samples per second with AMI. Ion imaging is also a high-speed technique whereby each pixel represents a separate sample. In ion imaging using conventional MALDI, some systems have been reported to operate at up to 500 pixels per second. [93] Apart from the challenges in loading samples and the speed of the mass spectrometer acquisition system, analysis rates are also determined by the sensitivity of the ionisation source and the ability to minimise carryover from sample to sample.

In this project, the potential to provide increased sample throughput rates approaching 100 samples per second is described using the (liquid) AP-MALDI ion source on the Synapt (with modified acquisition software).

1.6 Aims and Objectives of This Research

The overall aim of this research is to improve the alternative liquid AP-MALDI source for advancing MS and MS/MS analysis. This new source addresses some of the performance limitations of both conventional ESI and conventional solid-state (crystalline) MALDI and thus bridges the gap between the two. Unlike conventional MALDI, liquid AP-MALDI provides advantages in that it ionises directly from liquid droplets and it can generate multiply charged

ions. This project aims to expand on the previously developed liquid AP-MALDI source[41] with specific attention to the efficient coupling to a high-performance commercial mass spectrometer. One aspect involves the optimisation of the gas flow dynamics employed within the ion source transfer capillary interface. Furthermore, the work aims to show for the first time ECD and ETD of MALDI ions on a Q-TOF system using a prototype ECD device installed after an ion mobility cell. The ion source also features a highly precise and flexibly controlled spatial and temporal ionisation event provided by the tight focal point and timing of the laser pulse. This work also aims to show the potential for ultra-high-speed sample throughput offered by the technique as a result of using a laser as the ultimate precision tool for sample desorption.

2. Methods and Materials

2.1 Mass spectrometer and settings used

In this work all data were acquired from a modified commercial hybrid Q-Tof mass spectrometer (Waters Synapt G2-Si) fitted with a traveling wave ion mobility (TWIM) device. A schematic of the standard (unmodified system) fitted with an ESI ion source is shown in Figure 4. Briefly, from the ion source to the detector, the standard Synapt includes an ESI "Z-spray" ionisation source[94] and an intermediate pressure (3 mbar) stepwave RF ion guide for efficient transfer of ions from the ion source into the higher-vacuum regions of the quadrupole mass filter. The quadrupole was used for precursor ion *m/z* selection for subsequent ion activation and fragmentation in the downstream trap or transfer cells.

The "Triwave" region of the Synapt includes three consecutive pressurised travelling wave ion transfer devices between the quadrupole mass filter and the time of flight mass analyser. Briefly, the first device, the trap cell, was used for CID and ion-ion reactions, such as ETD (described below). The cell is also used for trapping and timed gating of *m/z*-selected ions into the next downstream device, the ion mobility separation (IMS) cell, which separates ions according to their size (collision cross section) / charge ratio. The IMS cell can also be used to measure the collision cross section of ions (however this aspect was not covered in this work). Optionally the third cell, the transfer cell, could be used for providing additional CID of ions following IMS as well as ECD (a non-standard modification detailed below).

The TOF mass analyser includes a two stage reflectron, the electric fields are arranged so that ions of the same *m/z* ratio but with higher kinetic energy spend more time within the device and then arrive at the detector at the same time. The TOF default settings were used so that it operated at a resolving power of approximately 20,000 FWHM in "resolution" mode.

The standard commercial version of Masslynx (version 4.2 SCN 983; Waters) was used for controlling the instrument and displaying data. DriftScope (version 2.8; Waters) was also used to visualise ion mobility data. (High throughput data were acquired using modified version of Masslynx as described in 2.10). For most experiments, the Synapt was operated in resolution, ion mobility and positive ion mode with the default settings applied. For the high-throughput data acquired in Chapter 5 (when a modified version of MassLynx software was employed), the system was limited to non-mobility mode of acquisition. The operation in ion mobility mode provided drift time data sets in which the spectra for specific drift times were summed, providing enhancements to the signal-to-noise ratio for peptide analytes. For experiments involving systematic changes to the cone gas flow, Waters Research Enabled Software (WRENS version 2.15.5; Waters) was used. WRENS provided script-based control to override various instrument parameters written in C# code (see appendix).

The collision energy for ions entering the trap cell was optimised and reported for each CID spectrum. All data were acquired with 1 second "scans" in ADC mode, except for the high-throughput data reported in Chapter 5. The capillary voltage was set at 2.5 kV for ESI measurements. However, in liquid AP-MALDI the high-voltage cable was modified to have a crocodile connector clip so it could be easily connected to the target plate and the voltage was increased to 3 kV. The cone gas setting was zero for ESI mode but optimised for liquid AP-MALDI as described in chapter 3. The source temperature was set to 100 °C. Desolvation temperature was set at 250 °C for ESI measurements only (not connected in liquid AP-MALDI mode). The desolvation gas was 200 l/h for ESI measurements (switched off for liquid AP-MALDI). The make-up flow in ETD mode was 20 ml/min. The nebuliser pressure was 6 bar for ESI measurements (switched off in liquid AP-MALDI). The discharge current 55 µA in ETD mode only. The ECD settings and description of the ECD modifications are described below.

2.2 Liquid AP-UV-MALDI source construction and modifications to the standard mass spectrometer

The liquid AP-MALDI source developed in this project was based on the design previously reported by Cramer *et al.* in 2013[41] except that the mass spectrometer (and associated source vacuum characteristics), the laser and the heated capillary were all different. An overall schematic of the setup is shown in Figure 14. For the majority of the data presented in this thesis, the laser used was a diode-pumped solid state UV laser ("Explorer One 349-120" (OEM); Spectra-Physics) with a wavelength of 349 nm (Nd:YLF), see section 2.3. The instrument framework above the ion source region was drilled to provide stable fixing points for an optical table to accurately support the laser and a manually adjustable primary steering mirror (diameter of one inch and UV-enhanced; Thorlabs, UK). The steering mirror was used to direct the laser light vertically downwards towards the ion source assembly. Figure 15 and Figure 16 show photographs of the liquid AP-MALDI source assembly mounted on the Synapt. (Safety considerations for these modifications are mentioned in the Appendix.)

The aluminium housing of the standard commercial nano-ESI source was machined to provide improved access and also drilled to provide mechanical fixtures for a 150 mm focal length plano-convex UV lens (Thorlabs, UK), the associated mounting post as well as an additional UV-enhanced mirror and its mounting post. The laser was guided on to the target plate using the two adjustable mirrors. The spot position and size were visualised using UV-sensitive paper and "ZAP-IT®" (manufacturer) laser alignment paper placed on the sample plate. The laser alignment paper also produced a convenient audible "tick" for each laser shot, the more tightly focused the laser the louder the ticking noise. The laser spot burn diameter was minimised by adjusting the position of the focus lens by up to +/- 15mm. The burn diameters from a thin-film matrix

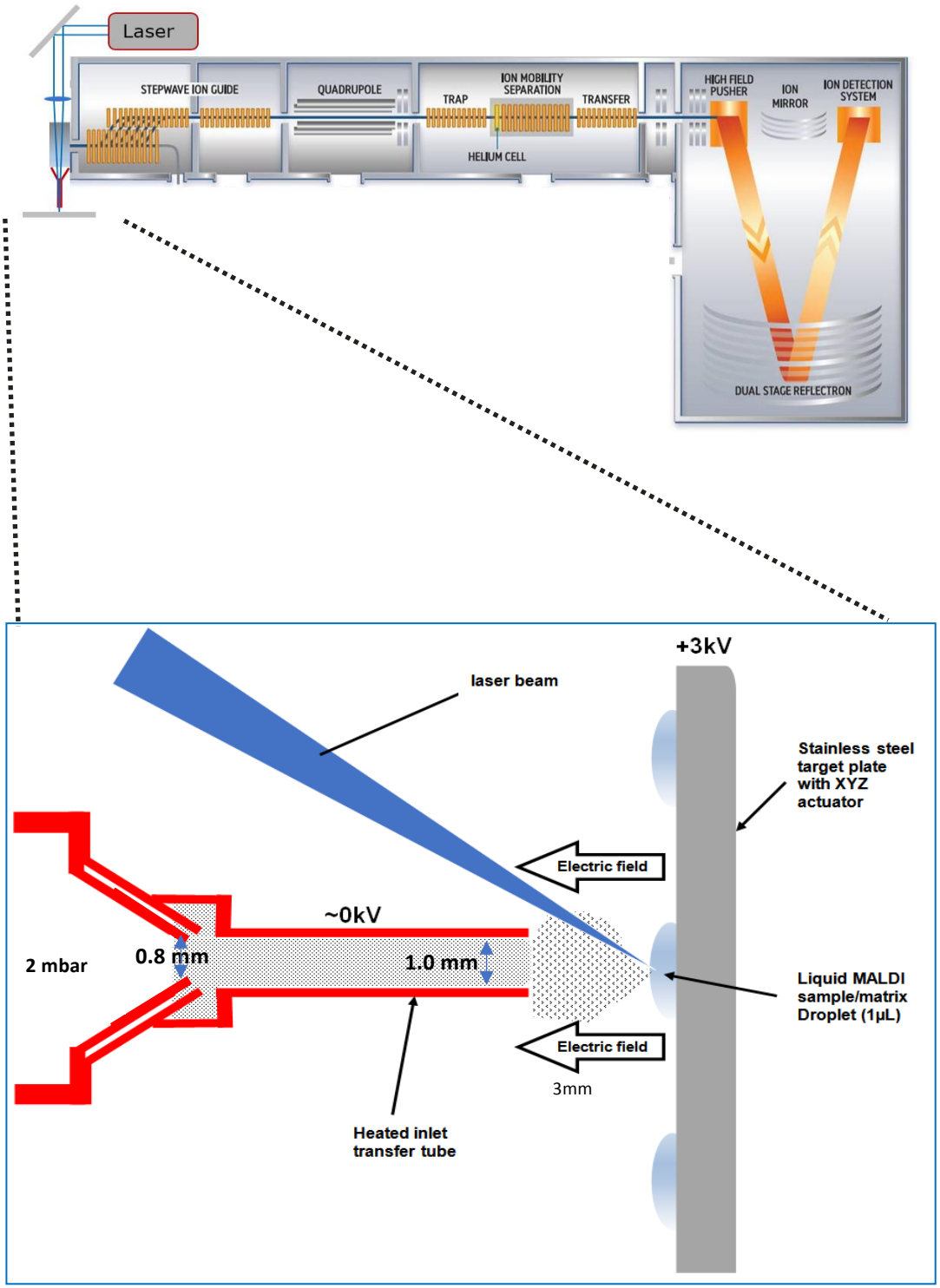

Figure 14: Overall schematic of the modified Synapt G2-Si system with the ESI source replaced by the experimental AP-MALDI source assembly including XYZ sample plate and heated inlet capillary. The capillary was held at 0V and the target plate at +3kV.

deposition[95] were measured with a travelling microscope at approximately 150 µm. In addition, it was also found that the most intense generation of multiply charged peptide ions occurred when the laser spot was as tight as possible with the current optics.

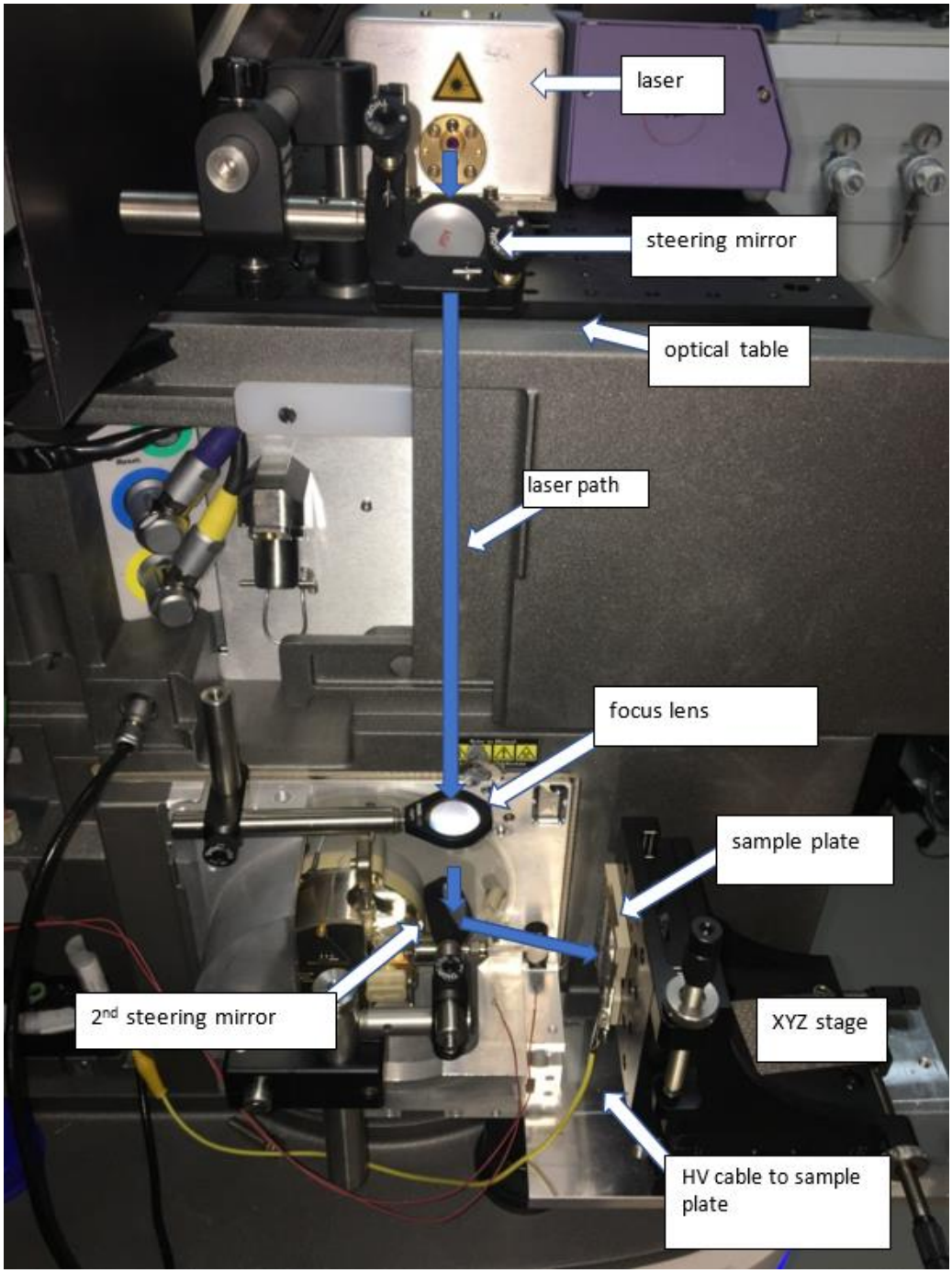

Figure 15: Liquid-AP-MALDI source fitted to the Synapt mass spectrometer illustrating the laser path.

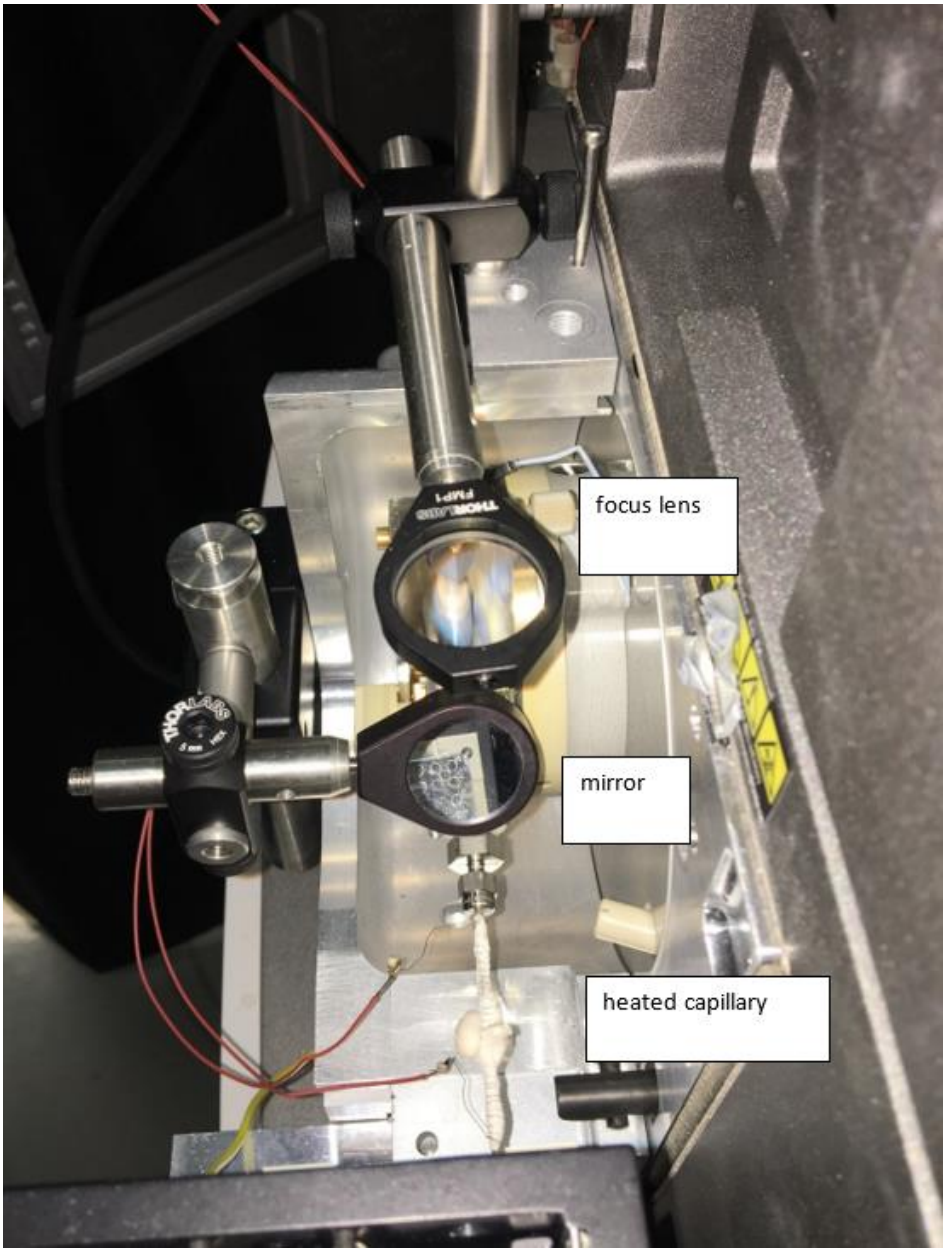

Figure 16: Liquid-AP-MALDI source (side view)

Referring to Figure 15, a ¼ format micro-titre plate format stainless steel MALDI sample plate (described below in 2.5) was held in place with small magnets embedded in a manually adjustable X-Y-Z stage (Thorlabs, UK). The stage was bolted to the modified ESI housing to ensure reproducible positioning between the laser focus position and the capillary inlet. The surface of the sample plate was positioned 3 mm +/- 0.5 mm from the entrance of the inlet capillary. The sample plate was insulated from the grounded X-Y-Z stage using a PEEK plate, this allowed the

application of several kilovolts (typically 3 kV) to the sample plate. The high voltage supply was derived directly from the instrument ESI capillary supply. The absolute potential of the sample cone and the directly connected inlet capillary was set close to 0 V by adjusting the “static offset” control of the Synapt.

2.3 Laser used and control of the pulse repetition rate and pulse energy

As mentioned above, the laser employed was a diode-pumped solid state UV laser with a wavelength of 349 nm (Nd: YLF). A photograph of the laser used in shown in Figure 17 and a summary of the manufacturer’s specifications for the laser are shown in Table 1.

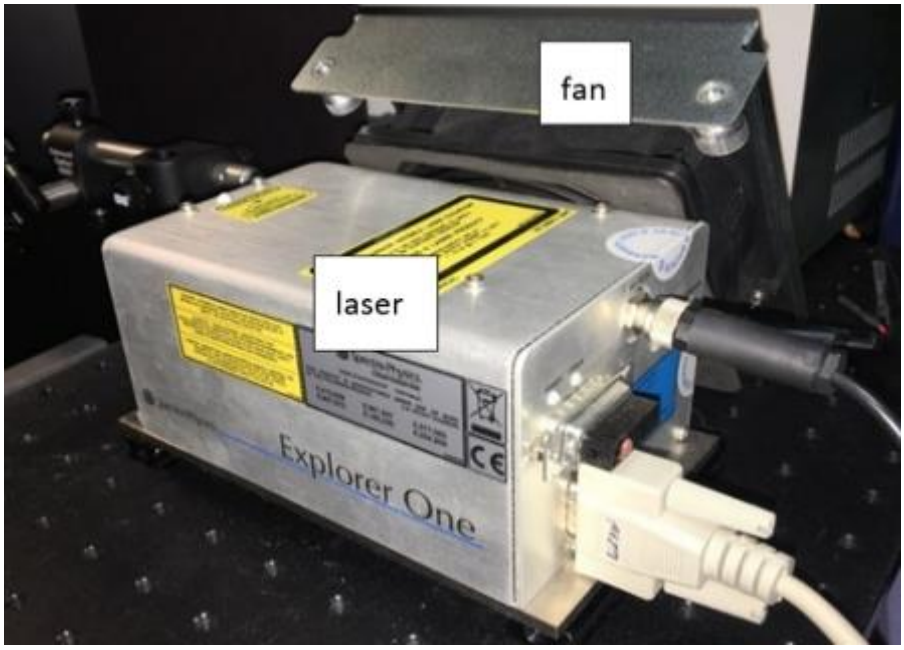

Figure 17: Photograph of the Explorer One UV 349nm laser and cooling fan on the optical bench

Table 1: Manufacturer specifications for the UV laser used for liquid AP-MALDI (Spectra Physics - Explorer One)

Beam quality	M^2 <1.3, TEM00
wavelength (nm)	349 (Nd:YLF)
pulse energy (µJ)*	10 to 80
repetition rate (Hz)	10 to 5000
divergence (mrad)	3.0 +/-0.5
output diameter (mm)	0.5
pulse duration (ns)	<7 (@ 20µJ)

The laser energy was controlled by changing the diode current setting and was usually set between 15 and 25 µJ per pulse (software control panel shown in Figure 18). The pulse energy was measured internally by the laser system and displayed as a readback in the software. The laser energy measurement from the display was compared and corrected using a calibrated energy meter, the LabMax-TOP with Energy Sensor J-10MB-HE (Coherent). The laser repetition rate was set at values ranging from 1 Hz to 5 kHz. For repetition rates above approximately 50 Hz the laser energy per shot reduces for the same bias current. Therefore, for experiments at higher repetition rates the bias current was manually increased to maintain the laser energy per shot (see Figure 19(a) to (c)). Also, worth noting is that the laser pulse duration was also a function of the diode current (as seen in Figure 19(b)), however this aspect was not explored in this thesis although it could be an interesting parameter for future study.

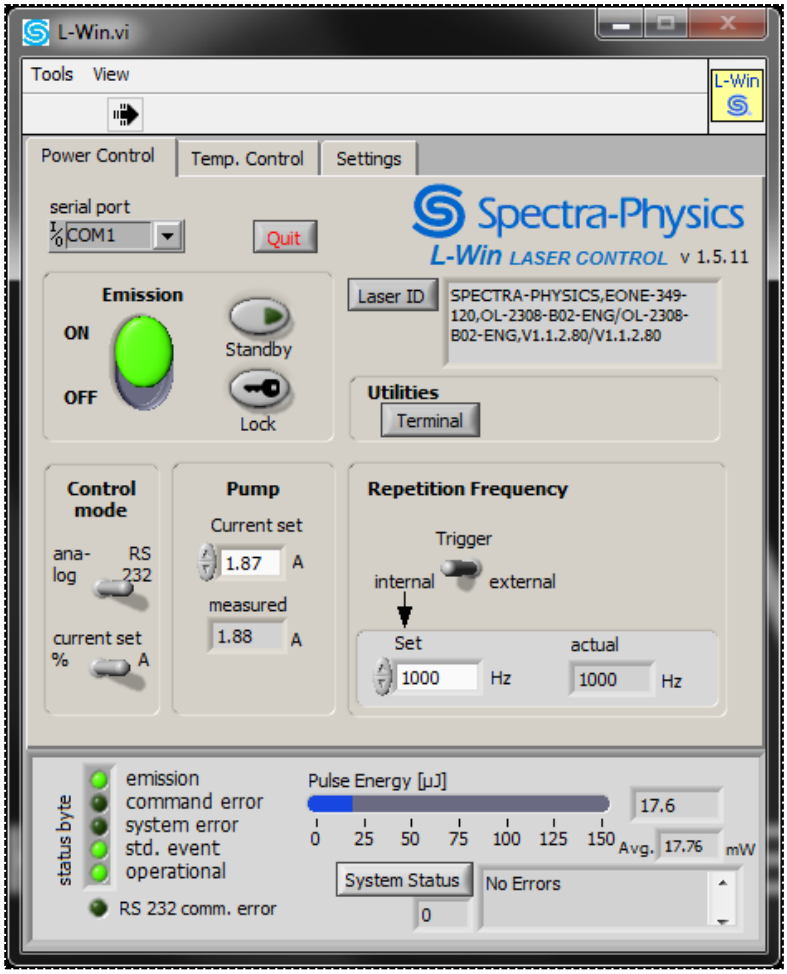

Figure 18: Screen capture from Spectra Physics' L-win laser control software, showing the diode current control, laser repetition rate control and pulse energy read back per laser shot.

(a)

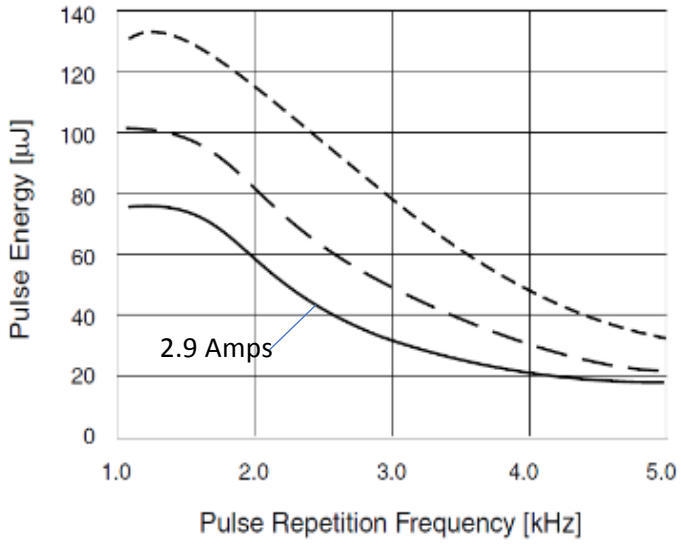

(b)

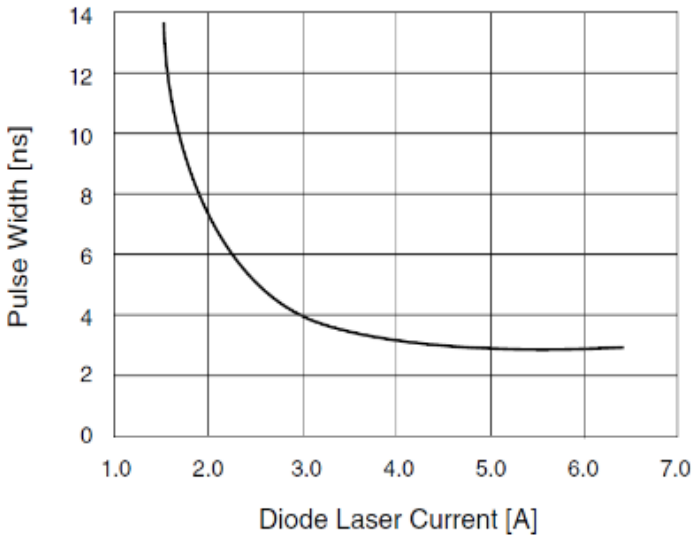

(c)

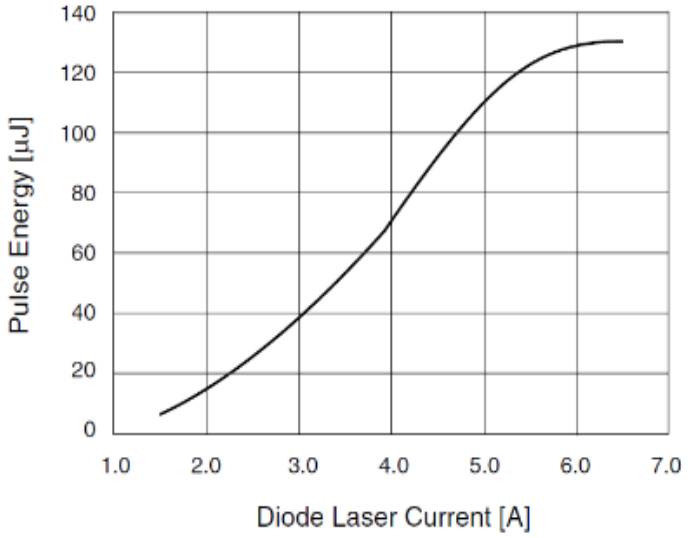

Figure 19: Laser performance characteristics as provided by the manufacturer. (a) pulse energy versus pulse repetition rate (solid line with 2.9A diode current), (b) pulse width (ns) and (c) pulse energy (µJ) versus diode laser current (A). Adapted from the manufacturer's user manual website.[96]

2.4 Heated capillary inlet construction

The heated inlet assembly was constructed around a stainless-steel capillary cut to 6-cm length (1/16th outer diameter and 0.04" (1.0mm) inner diameter from Greyhound, UK). A 1/16th fitting (Swagelock, UK) was welded on to the standard Synapt ESI outer cone assembly as shown in the 3D CAD drawings in Figure 20. The capillary was connected to the 1/16th fitting. The inner cone of this assembly, being the major flow restriction and "choked flow" expansion aperture into the vacuum, was kept at the standard 0.8 mm. The capillary was heated to approximately 250 °C, this was achieved by passing current of approximately 1.1 A through a resistive wire (40 Ω/m, 10 cm long) heating element manually wound around a ~1mm layer of a heat-conductive but electrically insulating ceramic paste cement previously applied to the capillary (OMEGABOND 600 Powder; Omega Engineering Ltd, Manchester, UK). An additional layer of paste was added to the heater element to provide mechanical stability and improve thermal homogeneity along the capillary (see Figure 21) The temperature of the assembly was monitored using a K-type thermocouple embedded in the ceramic paste, the current was manually adjusted to ensure a stable set temperature.

.

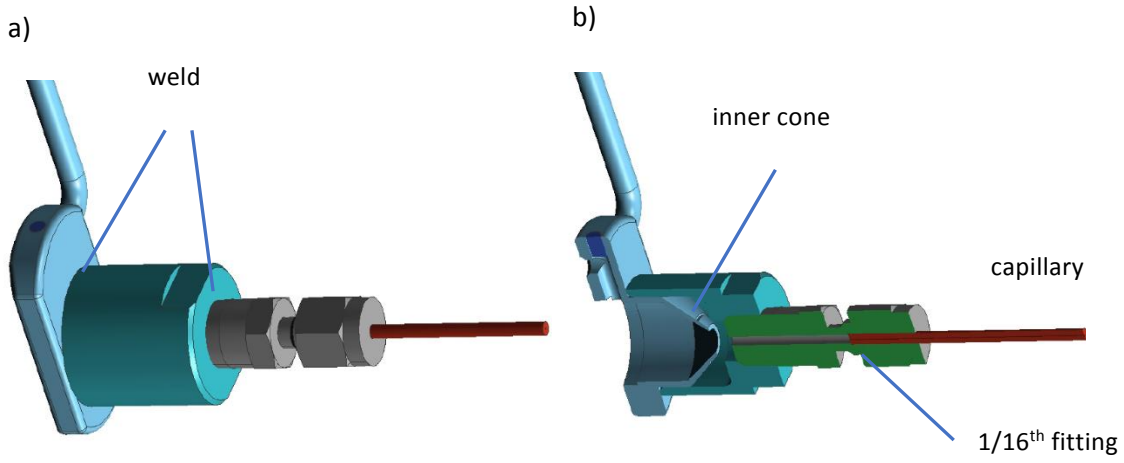

Figure 20: 3D CAD drawings of the modified sample cone with connection to capillary and 1/16th inch fitting, (a) outer view and (b) cross section revealing standard ESI inner cone

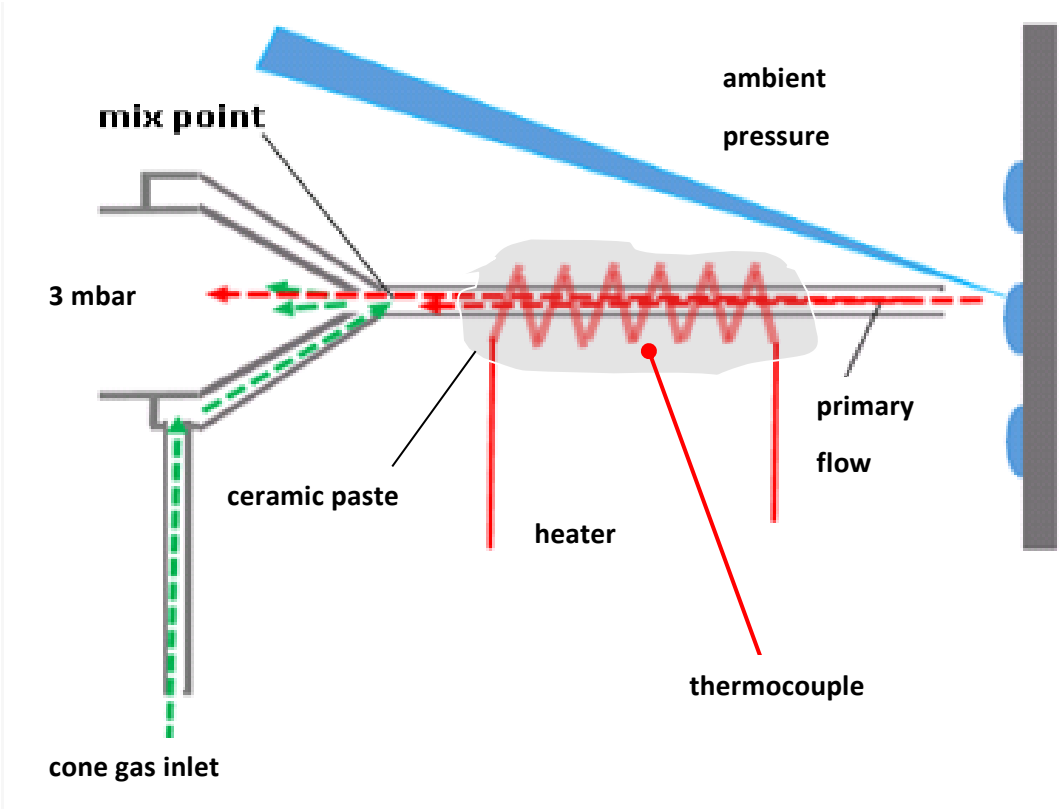

Figure 21: Modified cone inlet assembly illustrating primary and cone gas flow through the 6 cm long, 1 mm inner diameter heated capillary in series with 0.8 mm orifice into the MS vacuum. The primary flow is from atmosphere and carries the droplets and ions generated by the MALDI event. The cone gas also flows into the vacuum and mixes with the primary flow at the mix point. The ceramic paste serves to electrically insulate the heater element from the capillary but also provides mechanical stability as well as improving the thermal conductivity through and along the capillary.

A dual output multi-mode power supply, Model EXT752M by Aim-TTi international (Cambridge UK) was used to provide power to the heated capillary as well as the stand-alone fan to cool the housing of the laser (Figure 22).

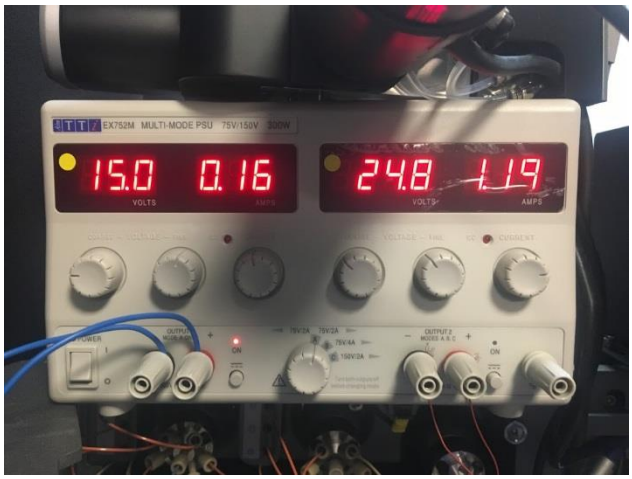

Figure 22: Dual output laboratory power supply was used for the heated capillary (and the 15V laser cooling fan).

2.5 Materials and MALDI sample plate

Unless stated otherwise, the following materials were all purchased from Sigma-Aldrich UK: caesium iodide (CsI) (99.9%; 202134-25G), substance-P (>95%; S6883-1mg), bovine ubiquitin U6253-MG, [Val5]-angiotensin I A-9402, leucine enkephalin hydrate L9133-25mg, angiotensin 2 human A9525-1mg, a-cyano-4-hydroxycinnamic acid (CHCA) C8982, 2,5-dihydroxybenzoic acid (DHB) 85707, glycerol 49771 5ml, bradykinin B3259-10MG, formic acid (Greyhound, Birkenhead, UK), "ZAP-IT®" laser alignment paper (Zap-It Laser, USA). MALDI samples were spotted onto Waters 96 well target plates (Waters part number 405010856). The plates are etched to have 96 sample wells (3.0 mm diameter wells at 4.5 mm pitch), rectangular format with 8 sample rows (A-H) and additional 24 spare wells for near-point calibration. Figure 23 shows a photograph of the sample plates used.

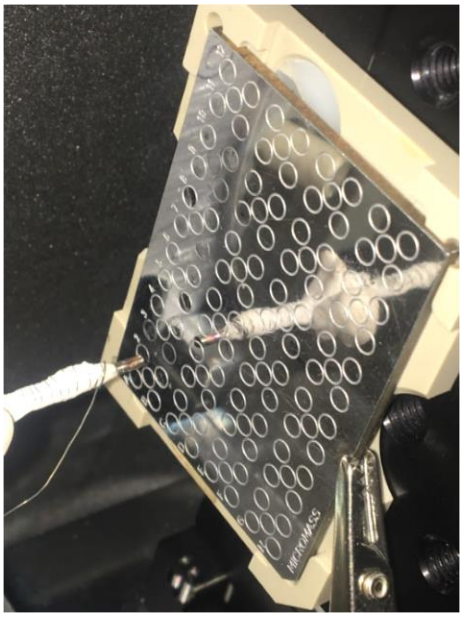

Figure 23: Photograph of 96-well MALDI stainless steel sample plate used for liquid AP-MALDI samples

2.6 Liquid MALDI matrix preparation

Peptides were dissolved in water at concentrations ranging from 100 fmol/µL up to 100 pmol/µL with the addition of formic acid (0.1%). For the liquid support matrix most experiments were carried out using the following recipe:

2,5-Dihydroxybenzoic acid was dissolved at a concentration of 100 mg/ml into a solvent mix consisting of 70:30 acetonitrile: water. An additional 60% by volume of glycerol was added to the solution. This was followed by 10 minutes of sonication.

An alternative matrix solution was prepared using 10 mg of CHCA dissolved in 1 ml of 50:50 water: acetonitrile. To this, 250 µL of glycerol were added.

Typical sample loadings included either 1.0 µL or 0.5 µL of analyte solution mixed with 1.0 µL or 0.5 µL of matrix solution on target. The surface tension of the droplets was high enough to prevent the liquid running down the plate due to gravity when the sample plate is held vertically.

2.7 ETD description and operation on Synapt

For ETD experiments, the instrument was arranged as shown in Figure 24. The standard ETD glow discharge source was utilised as described previously[97]. However, instead of the standard ESI source, the liquid AP-MALDI source was fitted. The ETD reagent was p-nitrotoluene. A few mg of reagent crystals were placed in the sealed reagent chamber and nitrogen make-up gas carries vapour from the reagent through to a hollow glow discharge needle positioned in the low-pressure region of the source block (typically held at approximately 2 mbar). A glow discharge voltage of ~ -300V was applied to the needle for 0.1 seconds to generate radical anions. The anions were selected by the quadrupole to remove unwanted (even electron) species and collected in the trap cell where they are trapped by applying a negative potential of 3V to the exit and entrance plates of the cell. The instrument ion optics cycle between positive and negative ion operation. For the positive part of the cycle (which typically lasts for 1 second), multiply charged analyte cations are introduced from the ion source and selected by the quadrupole for MS/MS, previously stored reagent anions are able to react with the cations within the trap cell. Although the 't-waves' cause ions of both polarities to move through the trap cell the 't-waves' also cause separation of opposing polarity ions. Changing the amplitude and speed of the trap 't-waves' provides a convenient means to regulate the interaction between the opposing polarity ions. This is essential as the excess of reagent anions can completely neutralise the cations should the ions be allowed to mix for too long. Product ions proceed through the ion mobility cell and transfer cell and into the TOF analyser. The trap t-wave amplitude was typically set between 0.2V and 0.3V, the glow discharge current was 40µA and the make-up gas flow was 50 ml/min. Other ETD instrument settings were applied using the default values provided.

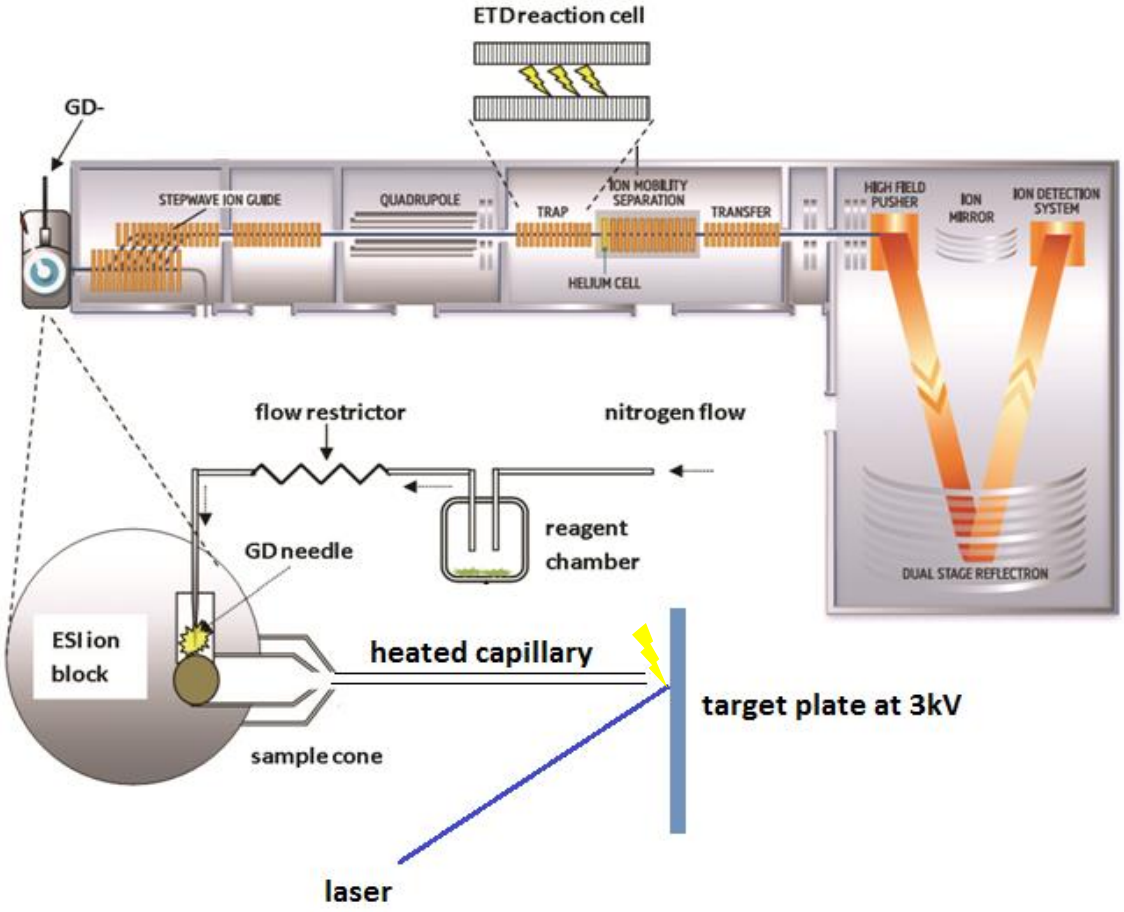

Figure 24: ETD reagent vapour is carried through to the glow discharge (GD) needle. Reagent anions are arranged to mix and react with analyte cations from the liquid AP-MALDI source in the trap cell (adapted with permission from Williams [97] (John Wiley and Sons)).

2.8 Prototype ECD cell on Synapt

For the ECD experiments a prototype ECD cell was purchased from e-MSion (Corvallis, USA) and installed into the Synapt with the assistance of Professor Joe Beckman (one of the cell inventors).[98–100] The cell was custom-designed to fit between the exit of the ion mobility cell and the entrance of the transfer cell. [101] The transfer cell had to be shortened to make space for the ECD cell. Fortunately, a short transfer cell had been previously developed for surface-induced dissociation (SID) studies. Several stacked rings (25mm) from the front of the transfer cell were removed for this modification. [102] The ECD cell was screwed to the exit of the IMS cell and details of the location of the cell are shown in Figure 25(a). The power supply for the ECD cell was also biased (using a direct connection) to the potential of the transfer cell entrance plate. The ECD cell's lens supply unit was controlled using "ExDPowerMangement" software from e-MSion.

The ECD cell is constructed with seven electrostatic ring lenses tuned to transmit cations and their fragments following interaction with the low-energy electrons (<1 eV). The electrons are provided by a rhenium filament (loop) that the ions pass through. A schematic of the cell is shown in Figure 25(b). Two of the electrostatic lens elements are samarium-cobalt alloy ring magnets, the field from the magnets (in conjunction with the electric fields) are designed to entrain electrons to the central axis and overlap with the cations. When operating in IMS mode the ECD settings were as follows: L1=5.7 V, L2= 5.4 V, L3 = 6.0 V, L4 = 5.7 V, Filament bias (FB) = 0.2 V, LM5 = 2.4 V, L6 = -2.4 V and L7 = -7.5 V. The filament current was 2.51 A. All electrodes in the ECD cell were connected to the potential of the Synapt transfer cell entrance voltage of 2.6 V. (All other Synapt settings were default values for IMS mode). The ECD modification was not detrimental to the performance of the standard system as the sensitivity before and after fitting the ECD device was approximately the same (data not shown).

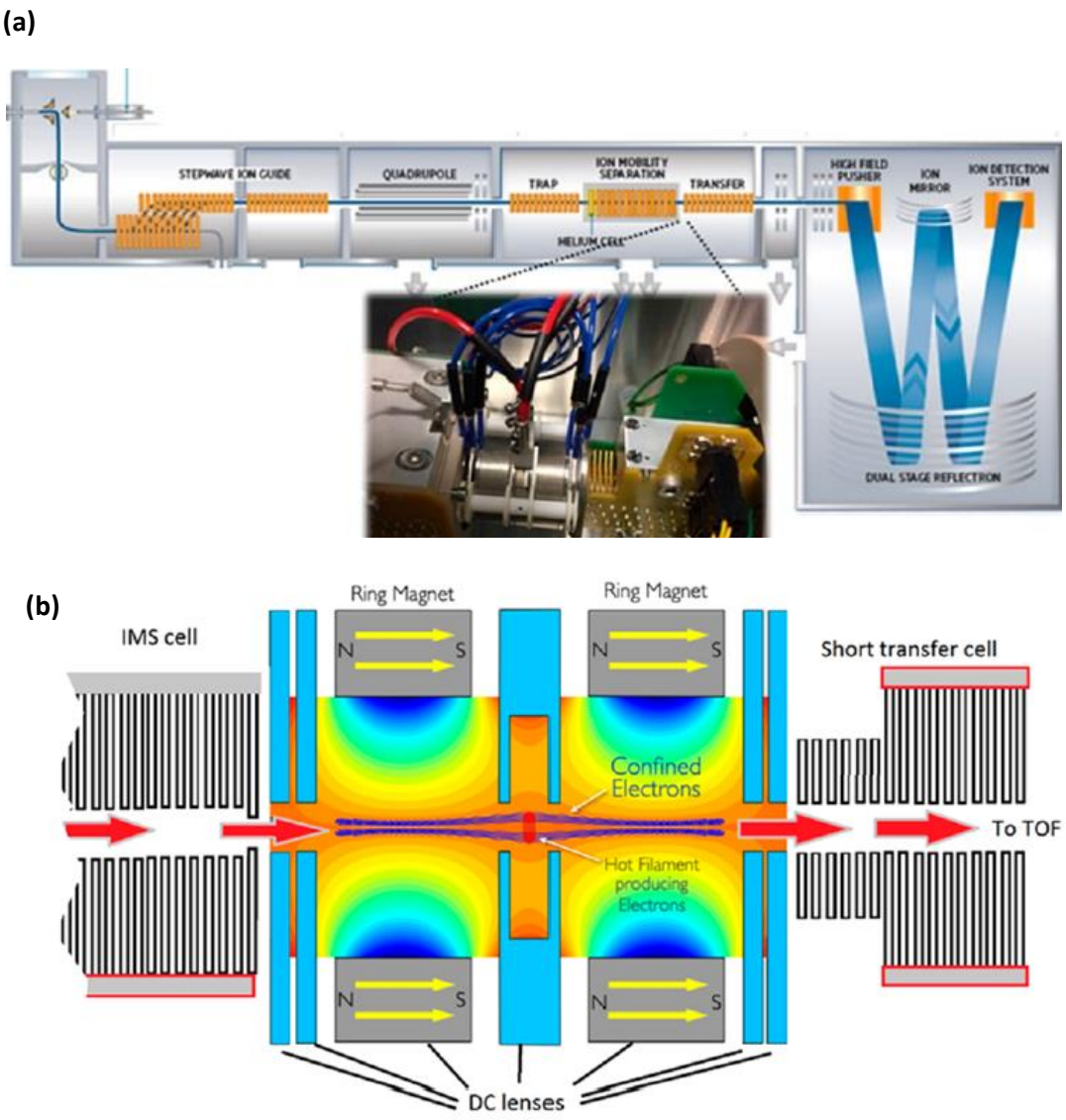

Figure 25: (a) Schematic of Synapt G2-Si with inset photo of the ECD cell mounted between the ion mobility cell and transfer cell. (b) Schematic of the ECD cell, showing the path of peptide ions (red arrows). The cell is comprised of 7 DC lenses including 2 lens elements that are also ring magnets that confine the electrons produced from the hot filament. [Adapted with permission from J. P. Williams, L. J. Morrison, J. M. Brown, J. S. Beckman, V. G. Voinov and F. Lermyte, Top-Down Characterization of Denatured Proteins and Native Protein Complexes Using Electron Capture Dissociation Implemented within a Modified Ion Mobility-Mass Spectrometer, Anal. Chem., 2020, 92, 3674–3681. American Chemical Society.][102]

2.9 Mass Calibration

The calibration of the *m/z* scale of the Synapt was performed manually from a solution of CsI ionised by ESI or via the liquid AP-MALDI source. In ESI, the procedure involves infusing a solution

of CsI at 5 µL/min and accumulating approximately 2 minutes of spectral data over the *m/z* range of interest (typically 100–3000). CsI was dissolved in water: methanol (50:50) (HPLC grade) and used without further purification at a concentration of 50 mg/ml. For MALDI, just 0.5 µL of analyte solution was added to 0.5 µL of liquid MALDI matrix on target.

For liquid AP-MALDI 1 µL of the CsI solution was mixed with the liquid matrix on target. CsI is an ideal calibration compound for TOF mass spectrometers because the cluster peaks observed $(CsI)_nI^+$ are well spaced,[103] thus providing a sufficient number of data points to enable the computer to accurately calculate the polynomial coefficients of the extended TOF equation as follows. Equation 12 is a higher-order version of equation 10 used within the software and caters for minor deviations from equation 10.

$$\left(\frac{m}{z}\right)_n = A + B\cdot\left(Tof_n\right)^2 + C\cdot\left(Tof_n\right)^3 + D\cdot\left(Tof_n\right)^4 + \ldots \quad \text{.....eq 12}$$

During the mass calibration routine utilising the commercial software (MassLynx version 4.2), a multiple number (n) of known spectral peaks $(m/z)_n$ corresponding to time of flight (Tof_n) measurements are used to mathematically determine the coefficients A,B,C,D, etc. of an $(n-1)^{th}$ order polynomial. Once the coefficients are established, the calibration function can be applied to the uncalibrated TOF spectra resulting in a calibrated *m/z* scale. For peptides, mass accuracy can be obtained to approximately 1 ppm (for statistically relevant peaks). Further correction of the calibration may be necessary due to long term (hours and/or days) thermal drift of the mass spectrometer system and can be applied by using an "internal" lock mass. This is a procedure

where a single (or multiple) known mass peak(s) within a spectrum is used to apply a small correction to the existing calibration coefficients.

2.10 High-throughput data acquisition

In order to describe the methods used in Chapter 5 for the ultrahigh-throughput data acquisition experiments acquired on Synapt, it is appropriate to briefly describe the functionality of the TOF mode, ion mobility modes and SONAR modes of acquisition. (N.B. the MassLynx software modifications for SONAR and modified SONAR for high-throughput acquisition were provided by Dr Keith Richardson and are not commercial products supported by Waters at the time of writing).

Within the TOF acquisition system, the oa-TOF pusher electrode fires at several tens of kHz - the rate is arranged to ensure that the ion with the greatest *m/z* value has been detected before firing the next pusher electrode pulse. The acquisition system does not record every spectrum separately from each oa-TOF push. If the scan time is set at 1 second, in TOF-only mode (non-ion mobility mode) several thousand TOF transients are accumulated into one spectrum for the duration of the scan.

In ion mobility mode, ions are briefly stored in the trap cell and are then electrostatically accelerated from the trap cell towards the ion mobility cell where they separate in time according to their cross section and charge. The electrostatic acceleration pulse is the start of IMS arrival time “clock”. The individual TOF transients from the pusher are labelled with the IMS timed index for each ion mobility “bin”. Instead of recording a single mass spectrum as in TOF mode, 200 separate oa-TOF spectra are recorded. However, only bins of the same index are accumulated.

In SONAR mode the quadrupole is scanned very quickly. The ion mobility mode capability is switched off, in that there is no drift gas admitted into the IMS cell. However, each scan contains

200 spectra but from specific *m/z* windows as determined by the quadrupole scan parameters. Each of the 200 spectra generated is from a different quadrupole *m/z* setting.

For the ultrahigh-throughput mode, the SONAR mode was modified so that the quadrupole was set to operate in RF-only mode, all ions were thus transmitted into the TOF. For a 1 second scan, 200 separate TOF spectra were generated with an effective acquisition rate of 200 spectra per second (ignoring a single 14 ms interscan delay applied for every scan). If the scan duration was set at 0.186 seconds (plus the 14 ms interscan delay every scan), the acquisition rate was 1000 spectra per second.

In this mode it was fortunate that the IMS "DriftScope" software designed for ion mobility could be used to visualise the data in a 3D chromatographic form. The horizontal axis represents scan time, and the vertical axis is split into 200 bins for each spectrum stored. The intensity of the heat map represents the TIC of each spectrum. Further details are included with the results in Chapter 5.

3. Results and discussion: The ion source, its construction, optimisation and interfacing to a commercial mass spectrometer

3.1 Initial attempts to generate multiply protonated ions by liquid AP-UV-MALDI

Following construction of the ion source as described in the materials and methods section the first attempts to observe multiply charged ions from a highly concentrated peptide solution (0.5 µL loaded from 100 pmol per µL of substance P) using the CHCA-based liquid matrix proved quite unsuccessful with only fleeting glimpses of doubly charged ions. Very weak singly charged peaks were sometimes seen, usually when firing the laser at the perimeter of the sample spot. In order to observe any ions at all the laser energy had to be raised to above 50µJ per shot which was significantly higher than what was reported by Cramer *et al.,*[41] such high laser energy per shot made the experiments difficult as the sample/matrix droplets were quickly depleted after a few hundred laser shots. However, by preparing the matrix and samples as for conventional dried droplet MALDI with CHCA matrix more reproducible data were observed for the singly charged peptide ions of substance P (see Figure 26). This indicated that the overall system was functioning but not for the generation of multiply charged ions from liquid AP-MALDI. It should be noted that these early attempts were carried out with a heating element simply wrapped onto thin layer of insulating paste on the inlet capillary, so the thermal contact was not ideal. Other parameters such as the laser focal position were also not fully optimised.

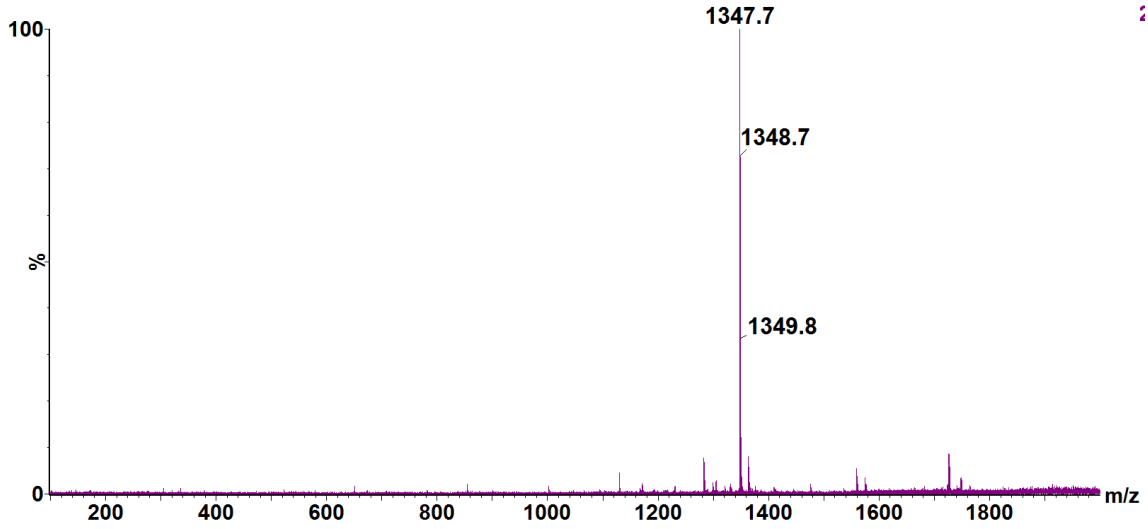

Figure 26: Initial solid-state AP-MALDI mass spectrum of substance P showing predominant $[M+H]^{1+}$ ion at m/z 1347.7. Loading of 0.5 µL solution (50 pmol) co-crystallised with 0.5 µL CHCA matrix (no glycerol added), +3kV on target, 20W applied to heated capillary, zero cone gas, laser pulse repetition rate of 10Hz with 50 µJ laser energy per shot, combined signal from 21 scans at 1 scan per second.

The thermal contact of the heater element to the capillary inlet tube was improved by applying more ceramic paste as described above. Operating at more elevated capillary temperatures (~220 ^{0}C) as measured by the thermocouple embedded in the ceramic paste increased the ion signals observed. Several other peptides were prepared and at least for [Val5] angiotensin I and the bradykinin standards, the observation of doubly and triply charged ions from the liquid MALDI sample became more reproducible (at the time, multiply charged ions from substance P were less abundant until further optimisation later in the project). The observation of multiply protonated ions was clearly evident from the increase in signal observed as the heater was activated and the capillary reached 220^{0}C (see results for [Val5]-angiotensin I in Figure 27 with example mass spectrum shown in Figure 28). On further optimisation, the persistence of the multiply charged ion signals was of sufficient duration to allow the collection of data for up to thirty minutes from a single microliter liquid spot.

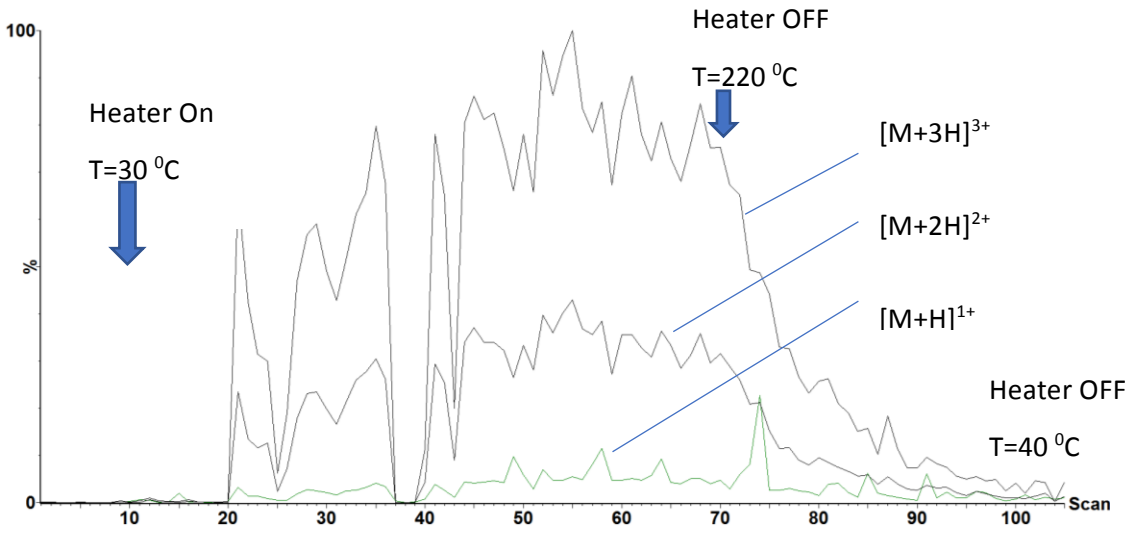

Figure 27: Liquid AP-MALDI preparation. Mass chromatogram traces for $[M+H]^{1+}$, $[M+2H]^{2+}$ and $[M+3H]^{3+}$ ions from [Val5]-angiotensin I as the heater of the inlet capillary was switched on at scan 10 and then off at scan 70. The temperature increased to a maximum of 220 ^{0}C. +3kV on target, 20W applied to heated capillary, zero cone gas, laser pulse repetition rate of 10Hz with 30 µJ laser energy per shot.

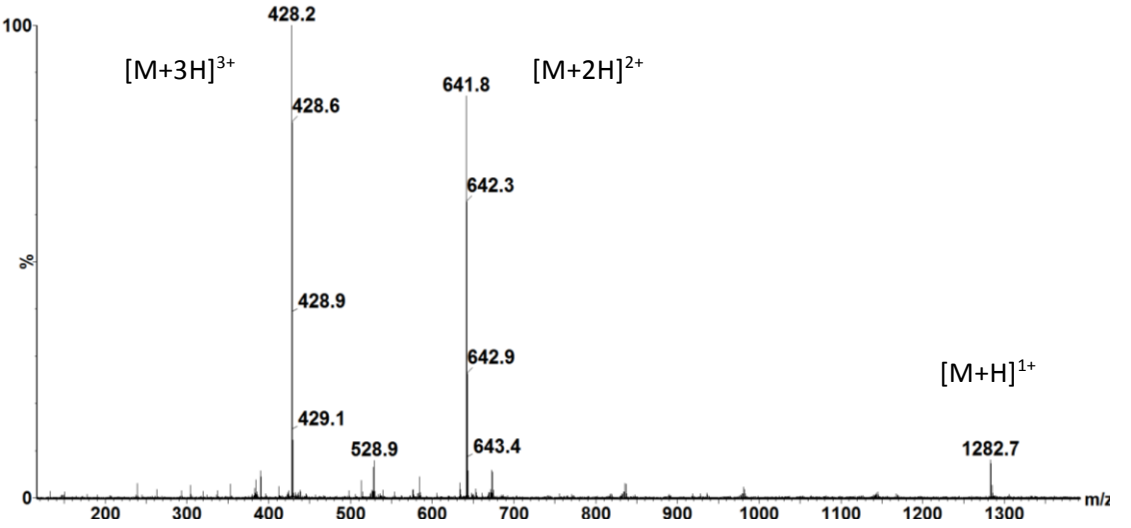

Figure 28: Example of liquid AP-MALDI mass spectrum of 0.5 µL solution of [Val5]-angiotensin I with 0.5 µL CHCA-based liquid matrix showing $[M+H]^{1+}$, $[M+2H]^{2+}$ and $[M+3H]^{3+}$ peaks. 50 pmol peptide loaded, +3kV on target, 20W applied to heated capillary, temperature of the capillary was set close to 220 ^{0}C, zero cone gas, laser pulse repetition rate of 10Hz with 30 µJ laser energy per shot, combined signal from 10 scans at 1 scan per second (spectral data scans 60-69, from Figure 27).

Once the higher charged ion signals were observed, further fine tuning of the position of the laser focus allowed a reduction in the laser energy per shot to approximately 15 µJ, which had the benefit of prolonging the sample and allowing further time for other instrument parameters to be optimised (such as ensuring that the trap and transfer collision energy were low enough (between 1 and 3 V per charge) to prevent fragmentation of the higher charged species). More intense and persistent signals of doubly and triply charged ions became possible from lower concentrations of peptide solutions and by using the DHB-based liquid matrix. However, before further optimisation was carried out experiments to check the laser energy per shot were carried out.

3.2 Laser energy verification

The laser manufacturer's software readback of the energy per laser pulse was a convenient feature within the L-win user interface (Figure 18). In order to verify, the laser pulse energy (as emitted directly from the laser head) was independently measured using a calibrated laser power meter (Coherent LabMax-TOP). 12 measurements of the pulse energy (mean of 10 pulses per measurement) were taken across a range of energies (5µJ to 65µJ). It was found that L-win software was reading approximately 13% higher than the calibrated laser meter (with a standard deviation of 2.7%). The calibrated energy meter specifications also include several errors (1.2µJ thermal noise, calibration uncertainty of +/-2% and linearity of +/-3%), in addition the L-win measurements were stable to +/- 1µJ (+/- 5% at 20µJ). It was considered reasonable to report laser energies in this thesis by dividing the L-win software readback by 1.13 to account for the fact it was reading 13% high. Furthermore, considering the errors, the overall accuracy of the corrected laser energy was better than +/-2µJ at typical values between 10 µJ and 30µJ.

Another factor to consider was that the pulse energy was measured before the two steering mirrors and focusing lens. Measurements taken before and after these lens elements suggested a further 23% attenuation before reaching the sample plate. For consistency, (unless stated otherwise) laser energies reported in this thesis were at the laser output window and not at the sample plate. (Fluence calculations were based on the energy per pulse per unit area at the sample plate.)

For the high-throughput experiments reported in chapter 5, at higher repetition rate settings, the laser diode pump current was increased to maintain approximately the same laser energy per pulse at each pulse repetition rate.

3.3 Multiply charged ion signal versus laser energy

At this stage of the project the multiply charged signals provided by the liquid AP-MALDI source were sufficiently reproducible to be able to measure the ion signal as a function of laser pulse energy. Figure 29 depicts the $[M+2H]^{2+}$ ion signals from a 5 pmol loading of bradykinin peptide within (0.5 µL from a 10 pmol / µL sample solution with 0.5 µL DHB-based liquid matrix). The vertical axis is a measure of the ion signal intensity (arbitrary units) from 100 laser shots when summed, i.e. 10 scans at 1 scan per second and a laser pulse repetition rate of 10Hz. The optimum pulse energy is just below 20 µJ (and approximately 16 µJ at the sample plate when accounting for the optical losses at the two mirrors and the focusing lens).

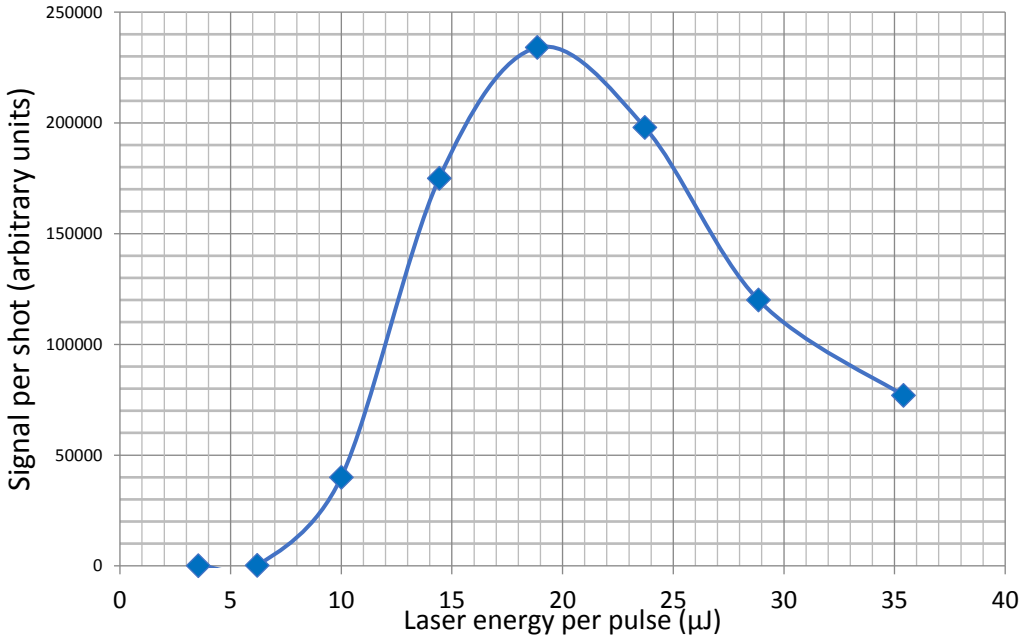

Figure 29:Doubly charged $[M+2H]^{2+}$ ion signals versus laser energy per pulse (µJ) from 5 pmol loading of bradykinin peptide. Spectral signals were summed for 100 laser pulses at each data point. Laser pulse repetition rate was 10Hz. (The pulse energy at the actual sample plate was 23% lower than shown.)

The mean laser fluence for an irradiated spot (defined as the total laser energy incident per unit area) is an important experimental parameter in MALDI.[104,105] For conventional dried-droplet MALDI the laser fluence values providing optimised ion generation only span about a factor of two to three beyond that of the threshold fluence (defined as the onset of ion generation).[106] If the laser fluence is too high, secondary processes become dominant with increased collisions, charge repulsion and fragmentation leading to significant loss of ion signal. The ion signal for conventional MALDI also follows an extremely steep function with laser fluence. In contrast, it can be seen from the plot in Figure 29 that the signal versus laser energy for liquid AP-MALDI of doubly charged ions is fairly smooth function (almost Gaussian in profile) however the range of useful fluence is similar to conventional MALDI. It is also interesting to note that the overall fluence values for liquid AP-MALDI is approximately similar (or within an order of magnitude) as conventional MALDI, whereas laserspray ionisation

requires significantly more fluence (approximately 2 orders more) and thus suffers from reduced practical performance in respect to high sample consumption through inefficient ablation (see Table 2). However, despite the fluence values for liquid AP-MALDI being relatively similar in comparison to conventional MALDI, in this project they were still higher by approximately a factor of 4. It seems remarkable that the fluence was similar, given the many experimental differences (including the matrix itself) that may have contributed to the higher value, such as matrix chromophore density, and thus penetration depth, laser wavelength, laser pulse duration, laser spot homogeneity or systematic differences in the measurement of the laser spot diameter. It is important to note that the conventional MALDI matrix chromophore (DHB) that is part of the liquid matrix formulation was definitely required to generate ion signals for liquid AP-MALDI, and this aspect together with the fluence range similarities were seen as strong evidence that the ionisation process in liquid AP-MALDI has some commonality with conventional MALDI.

Table 2: Comparison of typical laser fluence values reported in the literature and in this project for vacuum MALDI, laserspray ionisation and (liquid) AP-MALDI.

	Laser spot diameter (µm)	**Typical Fluence (J/m^2)**	**Reference**
Vacuum MALDI	125	100	Hillenkamp[104]
Vacuum MALDI	10	1000	Ens[107]
Vacuum MALDI	200	200	Ens[107]
Laserspray ionisation	NA	40,000 to 210,000	Trimpin[108]
AP-MALDI	500	500	Doroshenko [109]
Liquid AP-MALDI	50-100	200	Cramer[41]
Liquid AP-MALDI	150	800	*This work*

3.4. Signal persistence

Measurements of signal persistence were carried out by positioning the laser at the centre of the MALDI sample droplet. After starting the MS acquisition, the laser was continuously fired until the entire droplet was depleted. Initially, data were acquired with the laser energy setting at 25µJ (marginally higher than the optimum sensitivity value determined above). (Figure 30) Other experimental conditions were as follows: [Val5]-angiotensin I dissolved in H_2O (10 pm/µL of) ; Matrix: 100 mg/ml DHB in 70:30 (v:v) acetonitrile: water + 60% glycerol (with sonication); 0.5 µL of analyte solution mixed with 0.5 µL of liquid matrix on target; Laser pulse repetition rate: 10 Hz; ~20W of power were applied to the heater of the capillary (220 ^{0}C); 3kV, applied to sample plate.

It can be seen from the data in Figure 30 and Figure 31 that the conventional MALDI sweet spot problem has been effectively eliminated. This aspect of the technique enhances the analytical robustness and repeatability for most, if not all MALDI applications where liquid format for matrix/samples can be utilised. (Applications such as MALDI imaging would not necessarily benefit since the higher density of pixels would be a problem if the liquid on

adjacent pixels mix). As the laser fires and depletes the droplet, the droplet is shrinking. At approximately 16.5 minutes in Figure 30 a temporary drop-out in the signals from all charge states occurred. This effect was sometimes observed when the remaining liquid droplet was almost completely depleted. For complete consumption of the droplet without drop-out, the laser would have to be positioned exactly at the centre of the droplet and the droplet would have to shrink symmetrically around the laser focus irrespective of any sample plate surface irregularities. In this example, the signal recovered briefly as the droplet re-established its position at the laser focus.

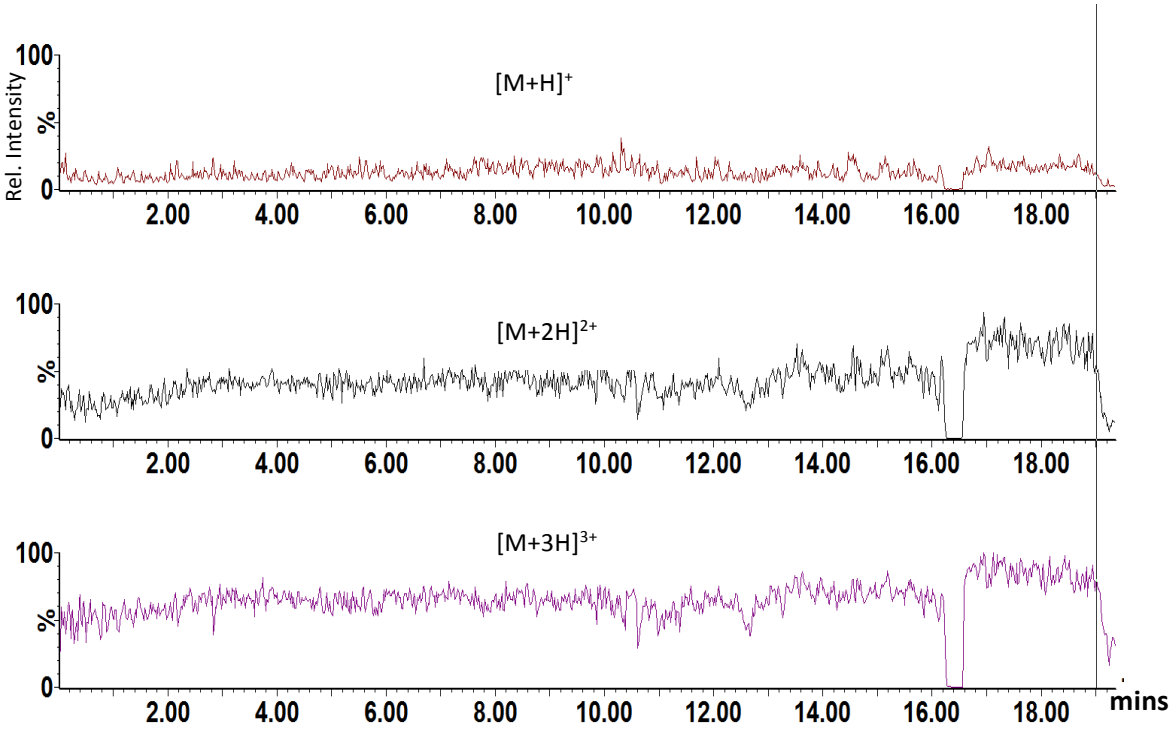

Figure 30: Mass chromatograms collected over 20 minutes from 5 mol of [Val5]-angiotensin I for $[M+H]^+$, $[M+2H]^{2+}$ and $[M+3H]^{3+}$ molecular ions. Vertical scales are linked for comparison. The laser pulse energy was 25 µJ and the sample persisted for approximately 20 minutes before complete consumption.

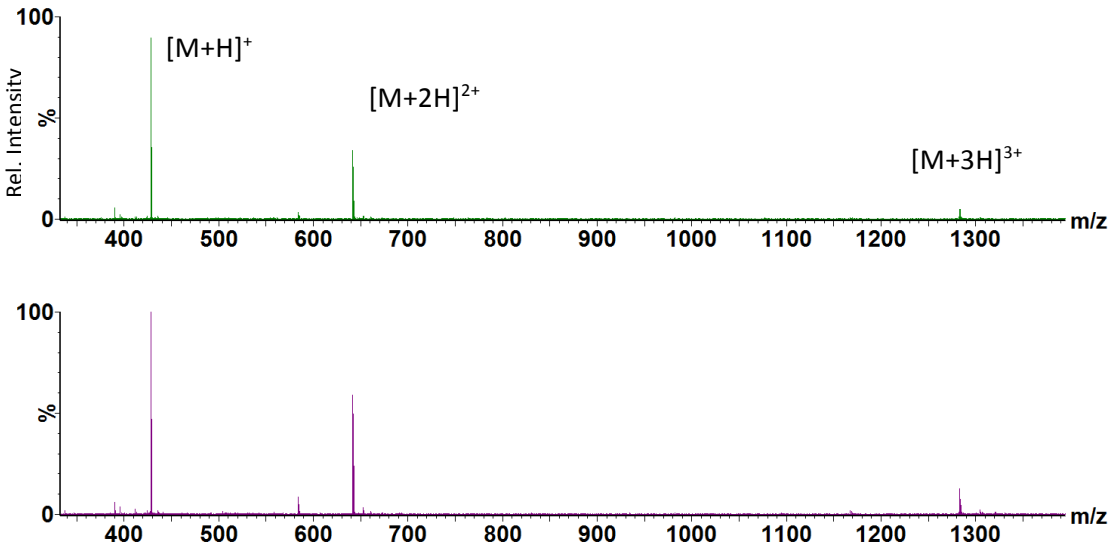

Figure 31: Liquid AP-MALDI mass spectra, depicting the longevity and spectral consistency for the $(M+3H)^{3+}$, $(M+2H)^{2+}$ and $(M+H)^{+}$ signals from a 5 pmol sample loading of [Val5]-angiotensin I in a 1 µL MALDI sample droplet. Top spectrum taken at 1 minute and bottom spectrum after 20 minutes (same data file as in Figure 30). The laser pulse energy was 25 µJ.

Another ion-yield persistence experiment was carried out following optimisation of the cone gas flow within the interface (further details in 3.4.1). For the second example, a different peptide was tested (bradykinin), the laser pulse energy was also reduced to 16 µJ in an attempt to extend the persistence even further than 22 minutes. The results of the second persistence experiment are shown in Figure 32. Both sets of results indicate that the persistence of multiply charged ion signals from liquid AP-MALDI ranges from 20 minutes to 90 minutes for a 1 µL MALDI sample/matrix droplet. The longer duration of greater than 90 minutes was most likely attributed to the lower laser energy per pulse (16µJ versus 25µJ) as in both cases, the droplets were fully depleted irrespective of the peptide used. This corresponded to mean sample consumption rates of approximately 11 nL per minute (or approximately 18 pL per laser pulse), this was comparable with previous in-vacuum liquid MALDI data that showed ~20pL per laser pulse for 2µL matrix/sample droplets (but 1pL per laser pulse from 10nL droplets that had been allowed to dry down to smaller volumes).[38]

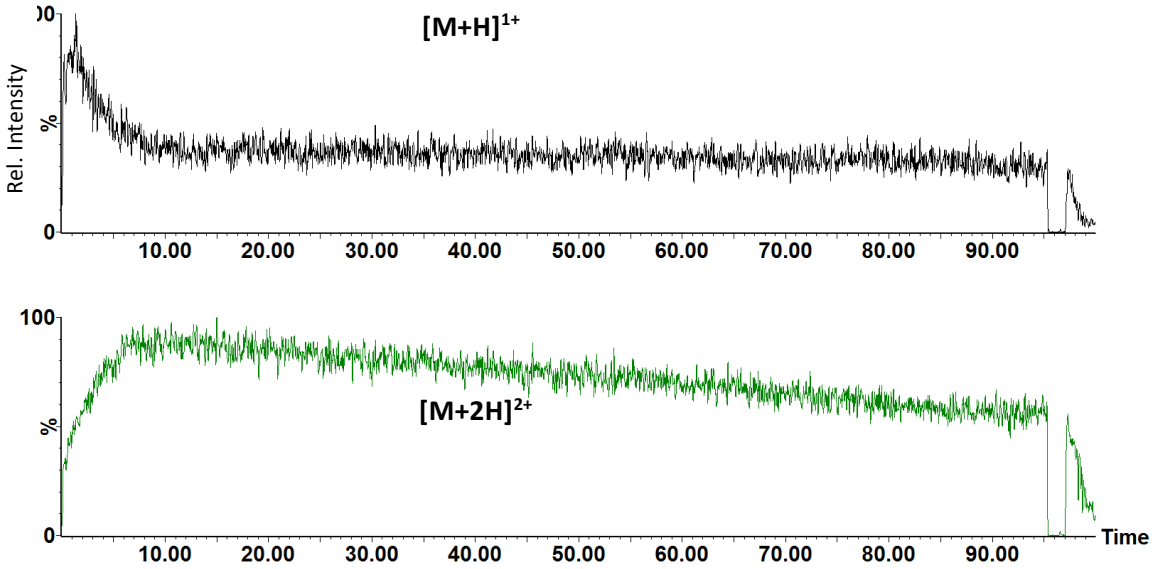

Figure 32: Mass chromatograms collected over 95 minutes from 1 µL of MALDI sample with bradykinin as analyte. (a) $[M+H]^+$ and (b) $[M+2H]^{2+}$ signals when irradiated at 10 Hz laser pulse repetition rate with a laser pulse energy of 16 µJ.

Interestingly, the first six minutes of the chromatographic data showed an increasing signal for the doubly protonated and a reducing signal for the singly protonated ions. This effect was not always observed (see Figure 30) and could be attributed to many factors and further experimentation would be required to ascertain the nature of the effect. Initial changes in desorbed droplet sizes through subtle changes in sample and matrix droplet constituents (possibly via evaporation of volatile components) might have been responsible. Such changes in droplet sizes would affect the optimum desolvation for higher charges. Other factors might have included temperature stabilisation or surface cleanliness phenomena within the transfer capillary affecting the desolvation process. (It should also be noted that similar instabilities have also been seen in previous liquid MALDI preparations even in the vacuum regime.[38])

Liquid AP-MALDI data were also acquired from a small protein (Figure 33). Ubiquitin (40 pmol, DHB-based matrix). Assuming the ~20 pL desorption volume per laser pulse, each laser pulse consumed approximately 1fmol. The top spectrum depicts excellent sensitivity for just 10

laser pulses (10 fmol sample consumed). The lower spectrum was the sum of spectra from 400 laser pulses corresponding to 0.4 pmol consumed. These data, like the multiply protonated peptide data illustrate the "ESI like" spectra that are obtained from liquid AP-MALDI.

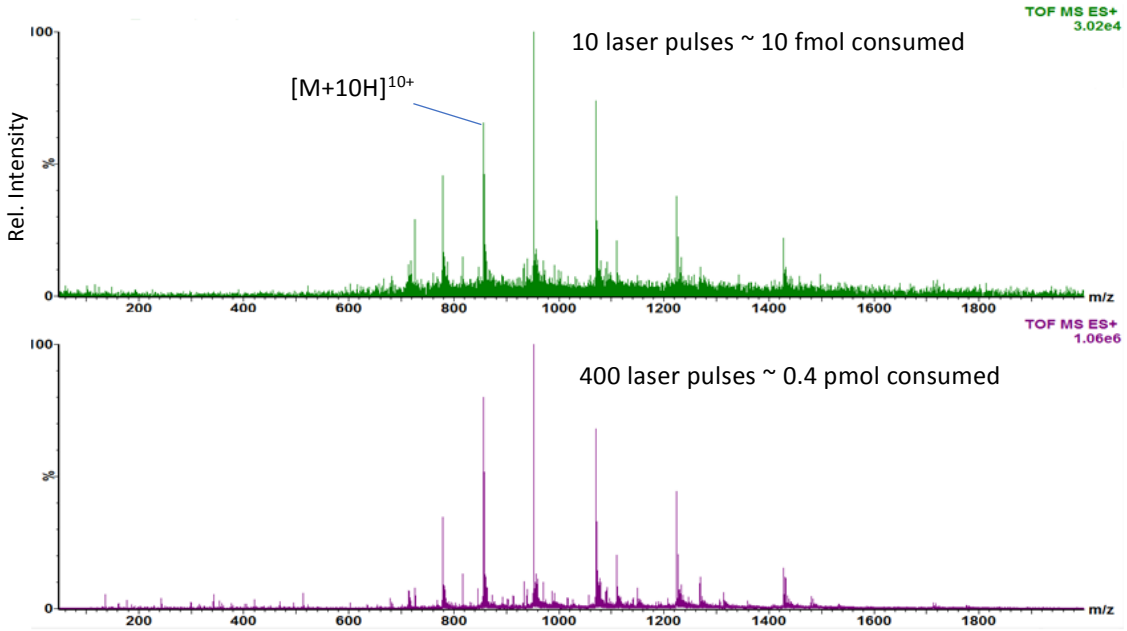

Figure 33: Spectra from 40 pmol of bovine ubiquitin (DHB-based liquid matrix). For 20pL desorption per laser shot 10 laser pulses consumes approximately 10 fmol (top) and 400 pulses consumes 0.4 pmol (bottom).

Following the acquisition of this data over long time scales, experiments to increase the laser pulse repetition rate were contemplated to increase the ion signal generated per unit time from a given MALDI sample droplet. This aspect was explored in Chapter 5 in the context of high-throughput sample rates.

3.4 The effect of gas flow on liquid AP-MALDI ion production

3.4.1 Cone gas flow effect on the signal intensity of multiply protonated peptides

Previously, it was shown that the temperature of the inlet capillary had a strong effect on the signal intensity of multiply protonated ions obtained from liquid AP-MALDI. In this chapter, the effects of the gas flow through the capillary are reported and discussed. The nitrogen "cone gas" or "curtain gas" that is normally used in ESI to deflect uncharged droplets, matrix and neutral molecules away from the entrance into the vacuum region of the ion source was left in place during the modifications for the liquid AP-MALDI source. A schematic of the gas flow within the system is shown in Figure 34. The primary flow which includes the generated MALDI sample plume passes through the 1.0 mm (ID) heated capillary towards the 0.8 mm cone aperture where it expands into the low pressure region of the mass spectrometer. The cone gas (hashed green line in Figure 34) passes around the outside of the inner cone and joins the primary flow of gas (hashed red line in Figure 34) just upstream of the 0.8mm cone orifice that normally separates the ambient pressure from the vacuum region. The cone gas flow was controlled from an N_2 calibrated Bronkhurst mass flow controller (MFC) via the MS software.

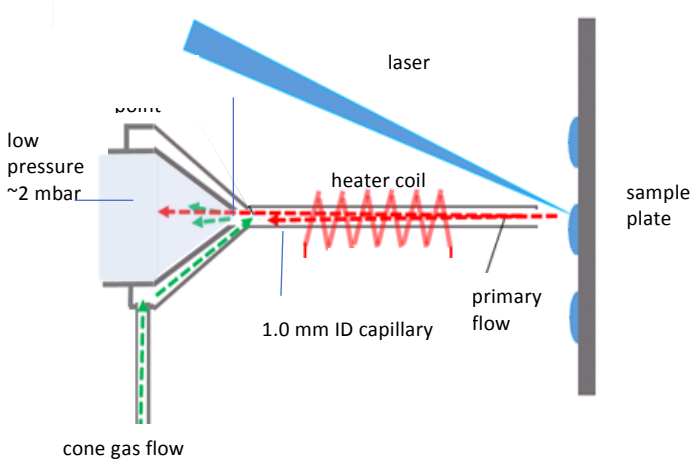

Figure 34: Schematic illustrating the path of primary gas flow (red dashed arrows) from the MALDI sample plate via the heated 1.0-mm (ID) capillary where it mixes with the cone gas flow (green dashed arrows). Mixing occurs upstream of the 0.8-mm orifice of the sample cone prior to expansion into the first low-pressure region of the mass spectrometer (typically operating at approximately 2 mbar).

Whilst trying to obtain improved ETD performance for liquid AP-MALDI ions (see Chapter 4), experiments involving the use of cone gas were carried out. It was noticed that by increasing the flow of cone gas, there was an increase in the ion abundance for the multiply protonated peptides. Further investigations into this effect were carried out. Figure 35 shows the mass chromatograms of $[M+H]^+$, $[M+2H]^{2+}$ and $[M+3H]^3$ ions from a 5-pmol loading of substance P. Experimental parameters were the same as previously described in the signal persistence experiments above. However, during the course of the acquisition the cone gas was linearly increased from 0 to 150 L/h (using the WRENS script in the appendix). It can be seen from the data that the triply charged ions have an optimum cone gas flow at approximately 70 L/h, the doubly charged optimum was at 120 L/h and the singly charged at approximately 140 L/h.

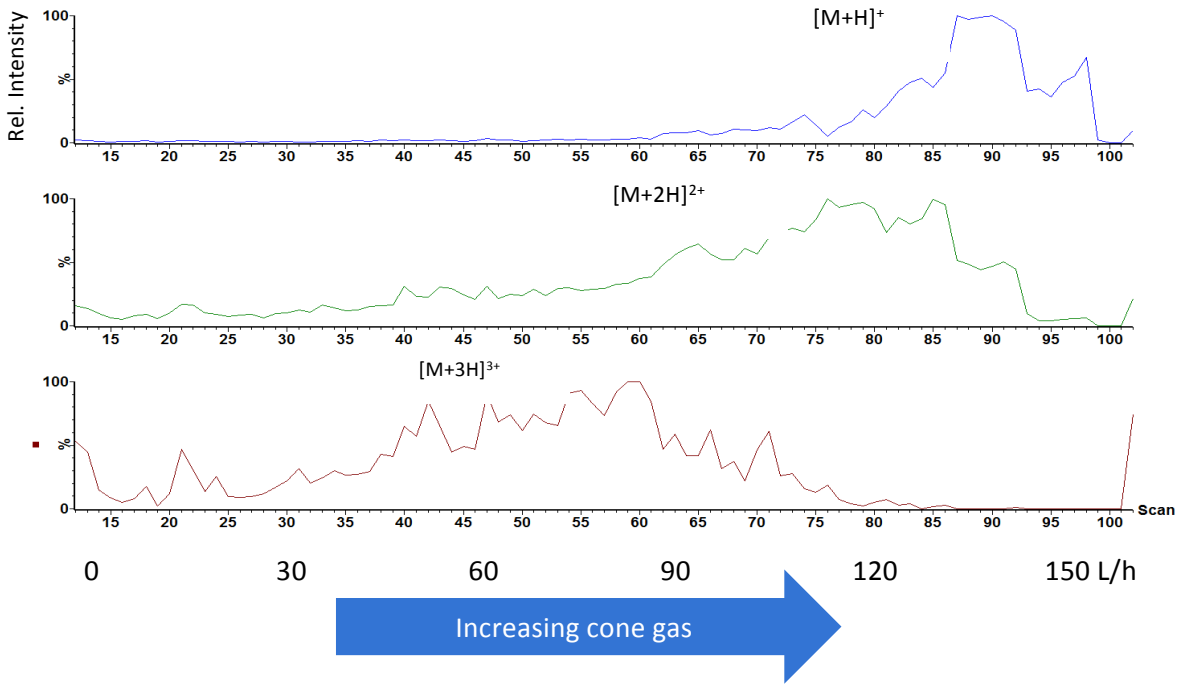

Figure 35: Liquid AP-MALDI mass chromatograms for the different charge states of protonated substance P, $[M+H]^+$, $[M+2H]^{2+}$ and $[M+3H]^{3+}$, as a function of the cone gas flow which was increased over the course of the acquisition.

An example of the spectra for 140 L/h versus no cone gas flow are shown in Figure 36. With the cone gas applied, the abundance of the doubly charged ion signal from substance P has increased almost by a factor of 40 compared with no cone gas.

A thermocouple was placed within the capillary and it was noted that the temperature increased significantly from 220 ^{0}C to beyond 500 ^{0}C as the cone gas was increased. This would be expected as the reduced flow of primary gas through the capillary would have significantly lowered the cooling effect on the capillary walls and heater element. (For very high cone gas flows (beyond approximately 200 L/h) it was interesting to see that the liquid sample/matrix droplets on the target plate were evaporated by a reversed flow of hot cone gas towards the sample plate.)

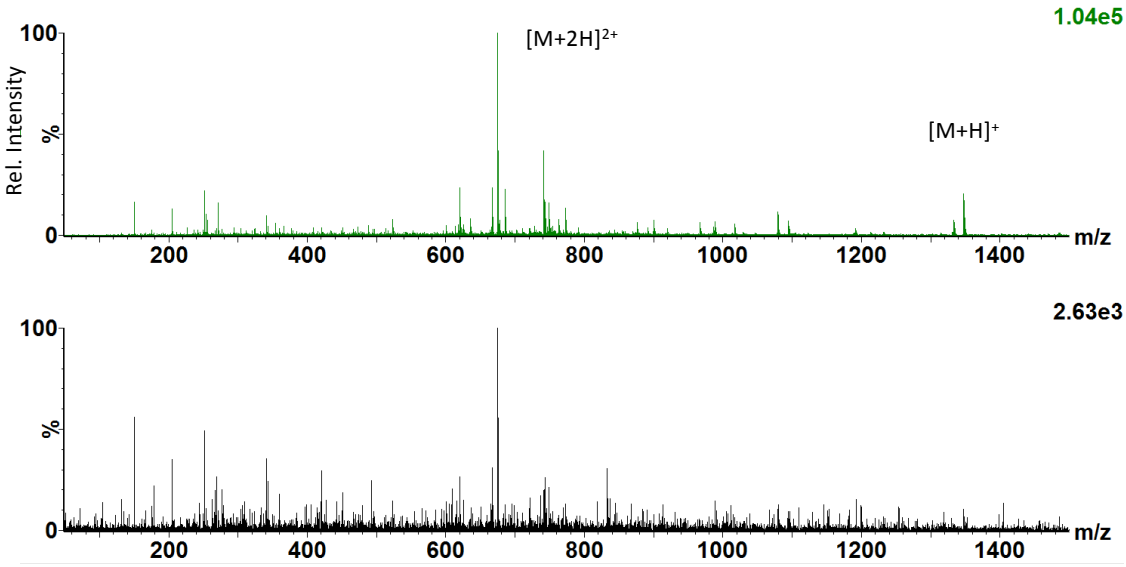

Figure 36:Liquid AP-MALDI mass spectra of substance P comparing the effect of 140 L/h cone gas flow (top) versus no cone gas (bottom) on the abundance of the $[M+2H]^{2+}$ and $[M+H]^{+}$ molecular ions. The cone gas flow at 140 L/h increased the abundance of the $[M+2H]^{2+}$ signal up to 40 times.

Within the same data set, the mass chromatograms of the sodium-adducted ions are shown in Figure 37. The optimum cone gas flow for transmission of the $[M+H+Na]^{2+}$ and the $[M+2H+Na]^{3+}$ was similar to the non sodiated species.

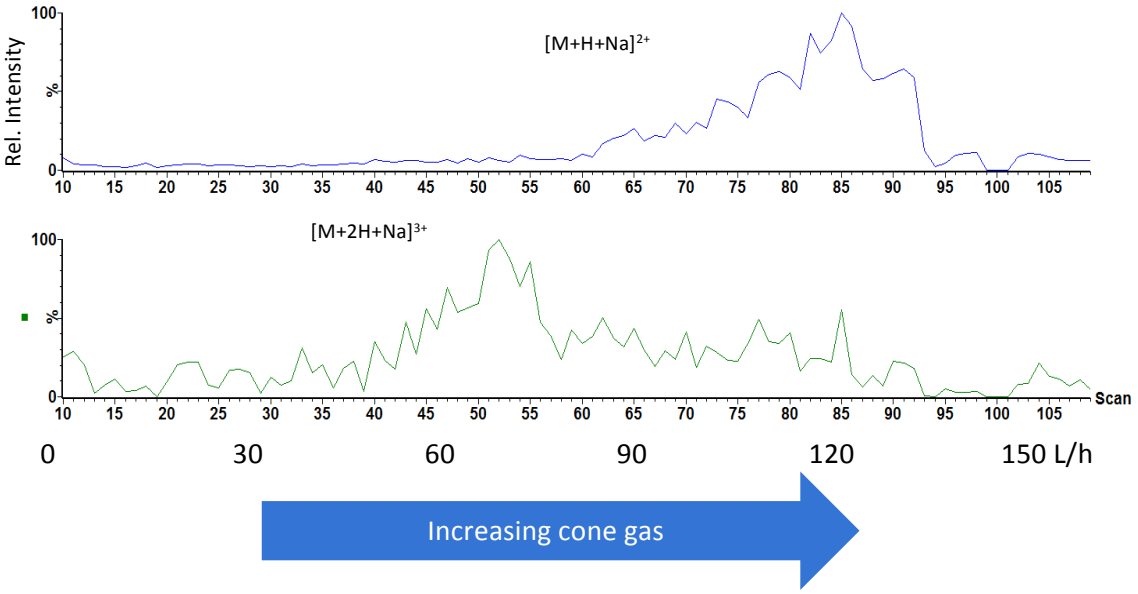

Figure 37: Liquid AP-MALDI mass chromatograms for the molecular substance P ions $[M+H+Na]^{2+}$ and $[M+2H+Na]^{3+}$ as a function of the cone gas flow which was increased over the course of the acquisition.

At the elevated cone gas settings, and thus higher interface temperatures, additional singly charged ion peaks appeared in the spectra. These were identified as fragment ions, they were matched and annotated as y type ions that would be typically observed by CID, surface induced dissociation (SID) and/or thermal decomposition (see Figure 38). The y-type fragment ions also included a single sodium adduct. Interestingly, their chromatographic profile closely matched the singly protonated molecular ion with respect to the optimum cone gas setting (see Figure 39). One explanation is that these ions became sodiated after fragmentation of the singly protonated ion. In addition, another effect of the cone gas is that the speed of the primary gas is slowed, possibly allowing more time for fragmentation, desolvation and adduct formation.

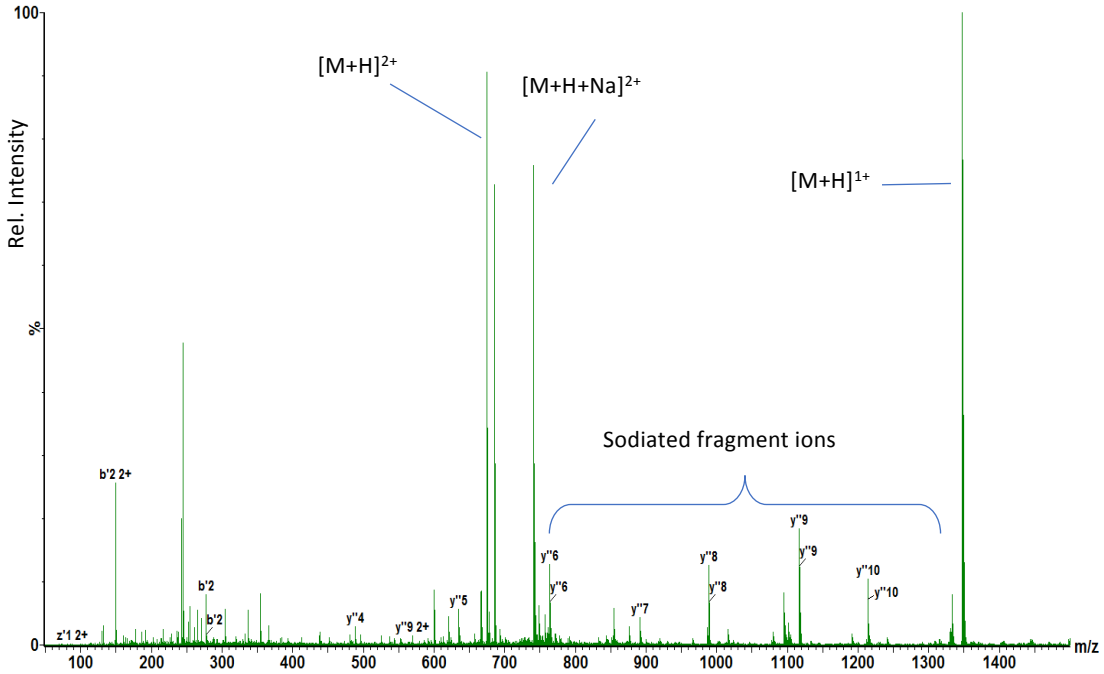

Figure 38:Liquid AP-MALDI mass spectrum. All of the y type product ions include an additional sodium (annotated using BioLynx software) from thermal dissociation within the heated transfer capillary for substance P with a cone gas flow of 140 L/h.

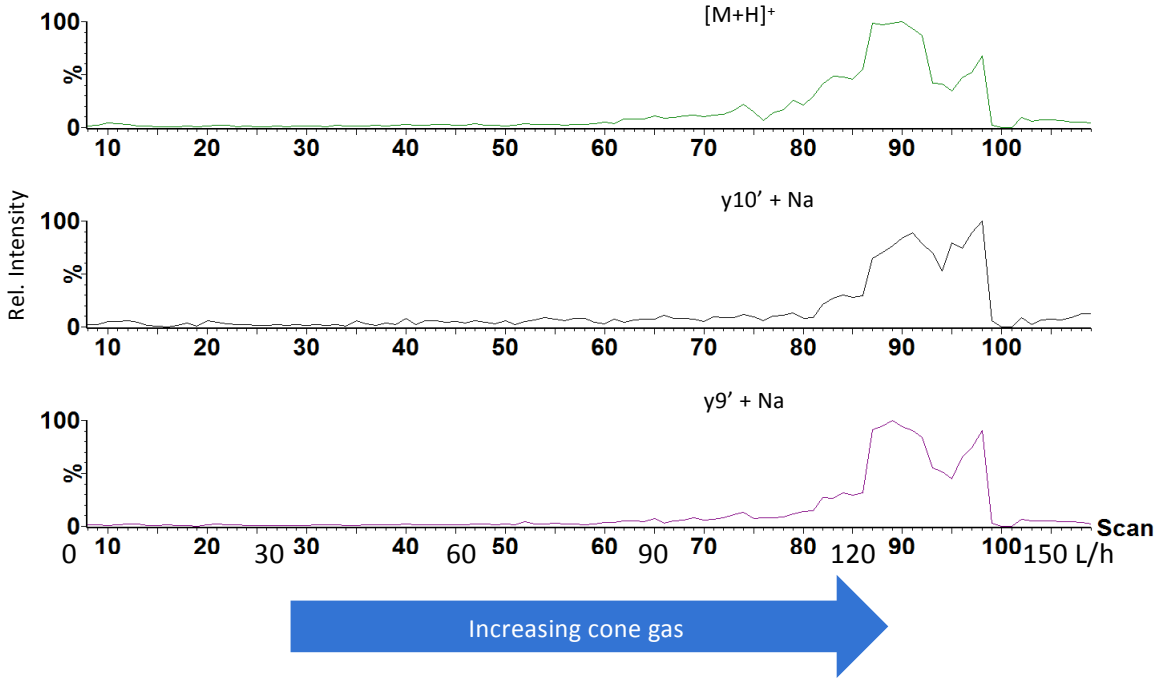

Figure 39: Liquid AP-MALDI mass chromatograms for the protonated molecular substance P ion $[M+H]^+$ compared with the singly charged sodiated fragment ions [y10' + Na] and [y9' + Na) at elevated cone gas flow settings.

3.4.2 Gas flow and desolvation time scale

In order to estimate the transit time of droplets within the heated capillary, it was necessary to know the flow rate of the primary gas. A simple experiment to measure the flow was devised in which the input of the heated capillary was blocked using a gas chromatography (GC) septum (Restek, UK). After blocking the flow of primary gas, the pressure in the first pumped region of the ion source dropped to $2x10^{-2}$ mbar from its normal value of 2.4 mbar (when cold at room temperature). The cone gas flow was then increased in steps of 50 L/h whilst the pressure in the source was measured, results were plotted (see Figure 40) and the curve was approximated with a polynomial fit (2^{nd} order). From the curve, it was possible to calculate the approximate flow of primary gas into the ion source vacuum (assuming minimal differences between air and N_2).

In Figure 40, line A (2.14 mbar) represents the measured source pressure with the capillary unblocked at 220 ^{0}C. To obtain the same pressure using the cone gas with the capillary blocked required 135 L/h (37 cc/sec).

Line B (2.4mbar) represents the measured source pressure with the capillary unblocked at 20 ^{0}C. To obtain the same pressure using the cone gas with the capillary blocked required 156 L/h (43 cc/sec).

Line C (2.6mbar) represents the measured source pressure with the capillary removed, i.e. only the 0.8-mm inner cone aperture restriction, at 20 ^{0}C. To obtain the same pressure using the cone gas with the capillary blocked required 173 L/h (48 cc/sec). It appears from these measurements that the capillary itself only restricts the flow of gas by an extra 17 L/h (5 cc/sec), thus confirming that the 0.8-mm cone orifice is the main restriction in the gas flow path.

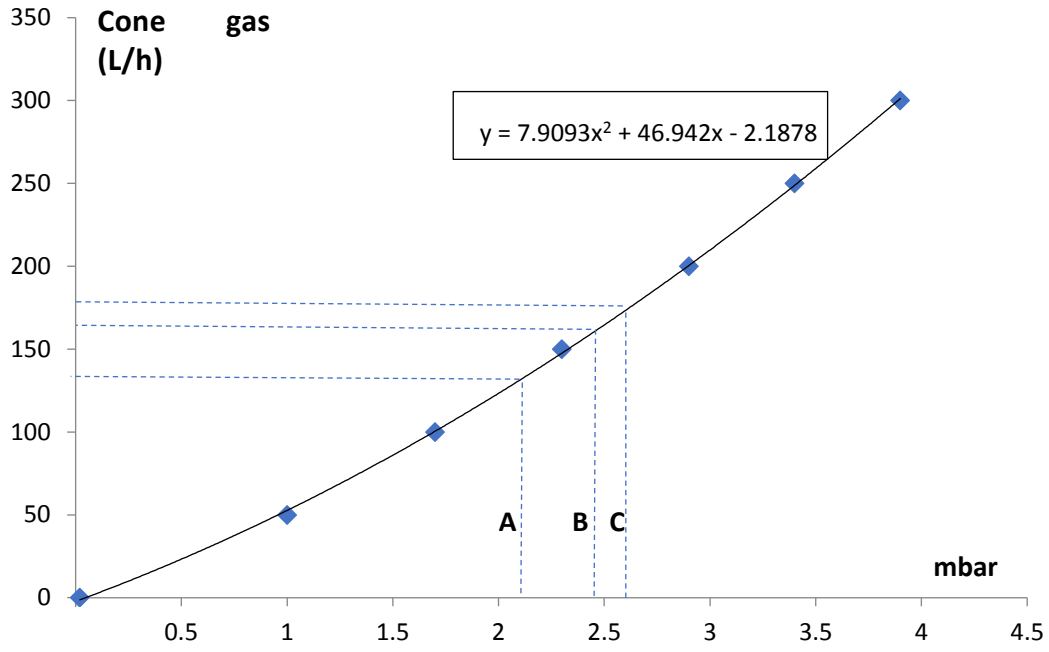

Figure 40: The curve shows the cone gas flow rate (L/h) versus source pressure (mbar) with the capillary blocked at the input end. From the curve equation (inset) it was possible to estimate the gas flow rate into the capillary at 135 L/h when unblocked, based on a source pressure of 2.14 mbar (line A) when the capillary was at 220 ^{0}C. Line B represents the source pressure when the capillary was unblocked and at room temperature, and line C represents the source pressure at room temperature when the capillary was removed.

Droplet desolvation, usually associated with ESI, is the process whereby the solvents, within the charged droplets emanating from the emitter are depleted through heating within the gas they are entrained. The aim of desolvation is to dry the droplets to bare gas phase ions. The drying down of droplets causes an increase in the concentration of salts and other impurities in the sample resulting in cationisation of analyte as well as the addition of non-covalently bound water, other molecules, and salt ions. Also, once the gas phase ions are relatively free of solvent, non-covalently attached solvent adducts can be further removed through supplementary electrostatic acceleration which causes ions to collide with the neutral gases thereby increasing their internal energy and propensity for decomposition.[110,111] As mentioned, sufficient solvent depletion is required to obtain ions via protonation or

deprotonation. This must be achieved early enough in the mass spectrometer system to ensure that the electric fields for ion manipulation become effective. If there is insufficient desolvation the analytes will be heavily adducted with solvent molecules ("wet")[112] leading to reduced analyte ion detection. The residence time of the ESI droplet whilst exposed to the heat in the source gases (and possibly direct interactions with the inlet surfaces) during evaporation is an important factor in the generation of multiply charged ions. With liquid MALDI, it is also anticipated that droplets of liquid matrix and analyte are generated in the desorption process, and it appears from the cone gas experiment that appropriate desolvation is required to generate increased abundance of multiply charged ions. However, the constituents of the liquid-phase droplets, as well as the surface tension of any droplets might require a more powerful desolvation regime to ESI.

Unlike the commercial ESI "Z-spray" ion source, the cone gas in the experimental set-up is sealed at the junction with the inlet capillary. Therefore, increasing the flow of cone gas causes a corresponding decrease in the flow of the primary inlet carrier gas carrying the desorbed droplets and ions. The mean velocity of the gas reduces, this in turn increases the temperature of the primary gas through increased heat transfer from the capillary walls. This also results in an increased transit time for desolvation to occur and the increased abundance of triply and doubly charged ions (Figure 35). This observation partially agrees with a publication by Fenn, in which he describes the higher charges appear after longer evaporation times and are more likely to be present with more effective desolvation. [113] However, as the cone gas was further increased there was a decrease in their abundance at which point more singly charged ions (and their sodiated fragments appeared). This could also be an indication that the multiply protonated species started to lose their protons through thermal dissociation.

The droplet lifetime during evaporation should be less than the transit time, the lifetime is known to be proportional to the square of the droplet diameter (approximately). [114] It has

been observed previously that glycerol droplet diameters increase with the laser fluence [115], therefore requiring greater desolvation (more cone gas), further experimentation would be needed to explore this concept.

With no cone gas flow, the mean gas velocity of the primary flow through the capillary is the volumetric flow rate divided by the cross-sectional area. The measured flow rate was 134 L/h (or 37cc/sec) and the area was 0.00785 cm^2. Therefore, the gas velocity in the capillary was approximately 47 ms^{-1}. Given the length of the capillary, this equates to a mean transit time in the capillary of approximately 1.3 milliseconds. By increasing the cone gas flow, the transit time could be significantly increased above this value, thus allowing for more desolvation and hotter primary gas as required. For example, with 100L/hr cone gas the transit time would the primary gas flow speed reduces to 34 L/h. (i.e. about a factor 4 times slower) thus increasing the transit time by a factor 4 to ~ 5 ms.

Another consideration is the flow regime. The characteristic quantity defining the viscous flow state is the dimensionless Reynolds number Re. Turbulent flow occurs when Re is above 4000, whereas below 2400, laminar flow will occur. The Reynolds number is calculated in a circular pipe for air at 20 ^{0}C in equation 13 [116].

$$\mathrm{Re} = 261.5 \cdot \mathrm{Q}/\pi \cdot \mathrm{D} \ldots\ldots\ldots\ldots\ldots\ldots\ldots\ldots\ldots\ldots\ldots\ldots\ldots\ldots\ldots\ldots\ldots\ldots\ldots\ldots\ldots\ldots\ldots\ldots\ldots eq.13$$

Where Q is the volumetric flow in mbar litre s^{-1}, and D is the inner diameter in mm. For the geometry presently in use, the measured primary gas flow rate was 135 L/hr (or 37 cc /s) and Re was ~ 3100. This indicates that without additional cone gas the flow is turbulent. By providing additional cone gas at levels for optimum generation of doubly or triply charged ions the flow regime becomes laminar. A laminar flow would involve a radial and axial distribution in temperature [117] within the inlet possibly causing a range of desolvation effects.

3.6 Calibration of the time of flight mass scale

An example of a CsI mass spectrum used for calibration is shown in Figure 41. The liquid AP-MALDI source was used to generate ion signals from CsI clusters over the mass range of interest. One µL of CsI solution was mixed on target with one µL of DHB-based liquid matrix solution. The laser was operated at 200 Hz and spectral data were accumulated for approximately 3 minutes.

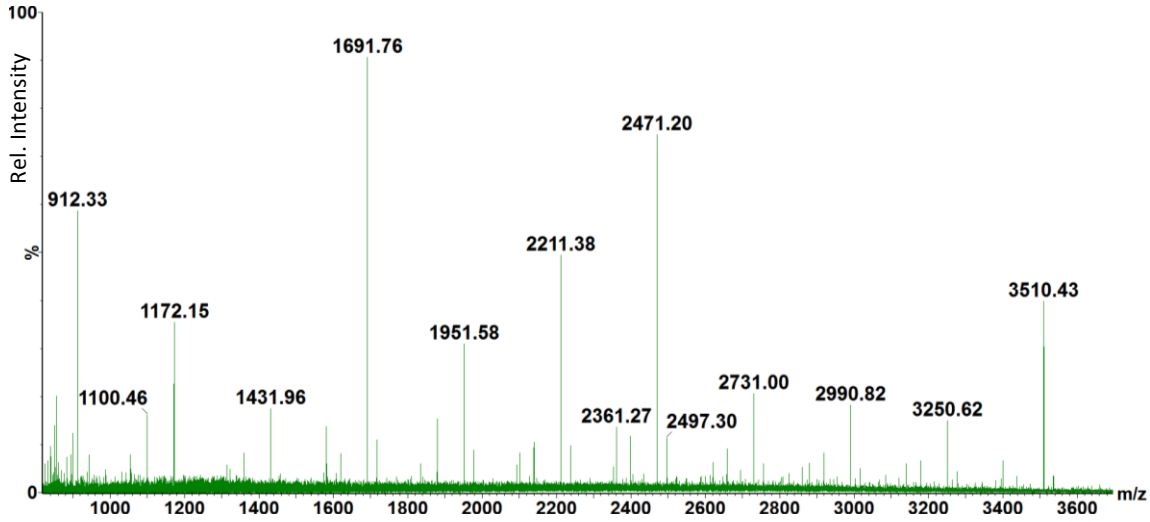

Figure 41: Liquid AP-MALDI mass spectrum of CsI used for mass scale calibration.

For the data shown in Figure 41, the system was in IMS mode and the ECD filament was in use (ready for an ECD experiment – see Chapter 4) but with a low current setting of 1.0 A. Despite some chemical interferences from the filament at lower *m/z* a confident calibration was achieved with residuals being approximately 1.3 ppm over the mass range from 100 to 4000 Th see Figure 42.

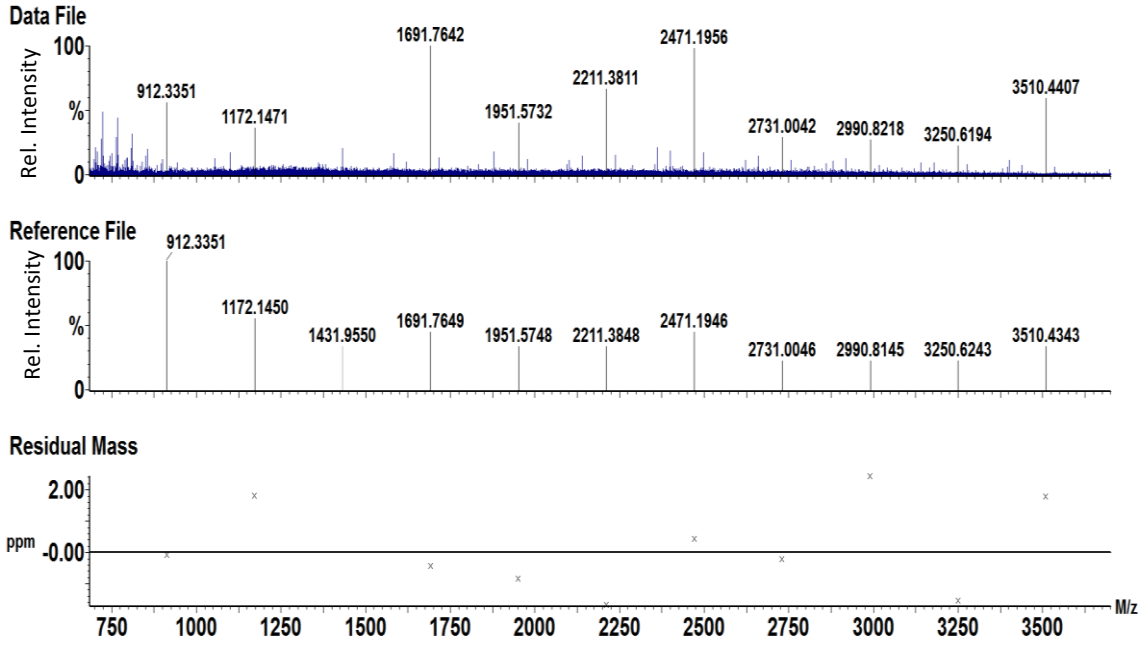

Figure 42: Calibration example in which a third-order polynomial function was fitted. Peaks were manually selected. The top spectrum was the acquired data, the middle spectrum was the reference file and the lower graph the residual errors after applying the calibration. A residual number of 1.31 ppm for this data represented the root mean square of the m/z differences between the observed data and the calibrated data after the calibration function was applied.

Although other standard compounds are often used for calibration, the use of CsI by this method provided sufficient abundance of ions within each spectral peak to generate a robust calibration function. The use of alkali halide clusters, such as CsI clusters, provides a relatively simple mass spectrum to match as there are no C_{13} isotopes to be concerned with in terms of erroneous peak determination and centroiding. It is also interesting to note that previous work with conventional dried-droplet crystalline MALDI reported that CsI was difficult to ionise over a wide mass range.[118] As such these calibration data suggest that ESI like ionisation is occurring, which also tends to generate predominantly singly charged ions from such compounds.

3.7 Use of ion mobility filtering to enhance the signal:noise of higher charge state ions

Ions generated by liquid AP-MALDI were separated by their mobility as they were propelled through the ion mobility cell of the Synapt. The Driftscope plot shown in Figure 43 is an example of an ion intensity "heat map", the x-axis represents the ion mobility drift time in milliseconds and the y-axis represents the *m/z* of the ions. It can be seen from the heat map that there are bands of ions for different charge states. The software allows the selection of regions of drift time. Once selected the data was reconstructed as a filtered spectrum. By selecting the band of IMS data corresponding to the desired charge state (for example 3+ ions), the singly charged chemical background ions were removed. Filtering by ion mobility significantly enhances the signal-to-noise ratio, providing a much lower limit of detection for the multiply charged ions of interest. Figure 44 illustrates the filtering effect. Figure 44(a) is the unfiltered spectrum as would have been obtained without ion mobility. Figure 44(b) is the spectrum obtained when only the singly charged band of ions as seen in Figure 43 are selected. Figure 44(c) shows the spectrum obtained when reconstructing the doubly charged mobility section. Similarly, Figure 44(d) shows the spectrum for the mobility filtered triply charged ions.

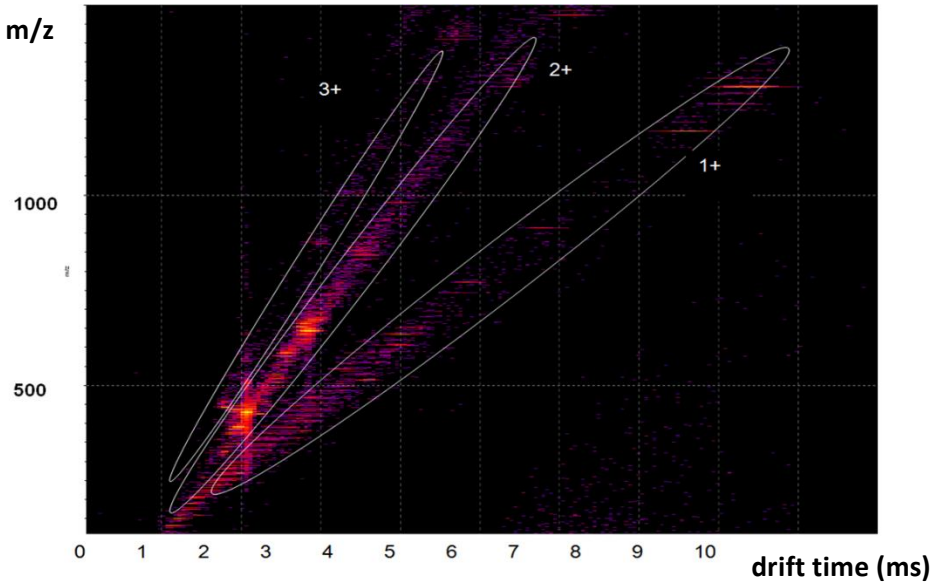

Figure 43: Example of a heat map plot depicting ion intensities for drift time and m/z. The data were acquired from a 5-pmol loading of [Val5]-angiotensin I with the CHCA-based liquid matrix. The laser pulse repetition rate was 20 Hz and the laser energy per pulse was 18 µJ.

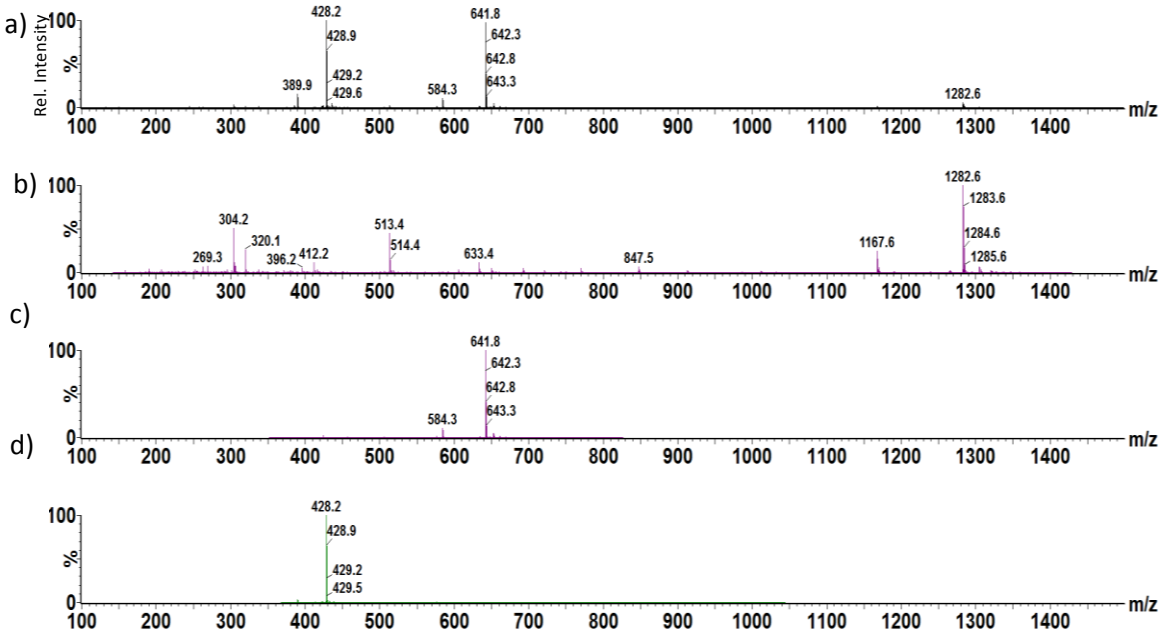

Figure 44: By filtering the data shown in Figure 43 for the bands of different charge states, the spectral peaks for each charge state are enhanced. a) is the full spectrum with no drift time filtering, b) is the spectrum for a singly-charged band of ions, c) is the spectrum for the doubly charged band of ions and d) is the spectrum for the triply charged band of ions.

A similar experiment was carried out using bradykinin, however only 1 pmol was loaded. Figure 45 depicts a clear enhancement of the triply protonated molecular ion when drift time filtering was employed. The data were acquired for 3 minutes using a laser pulse repetition rate of 20 Hz.

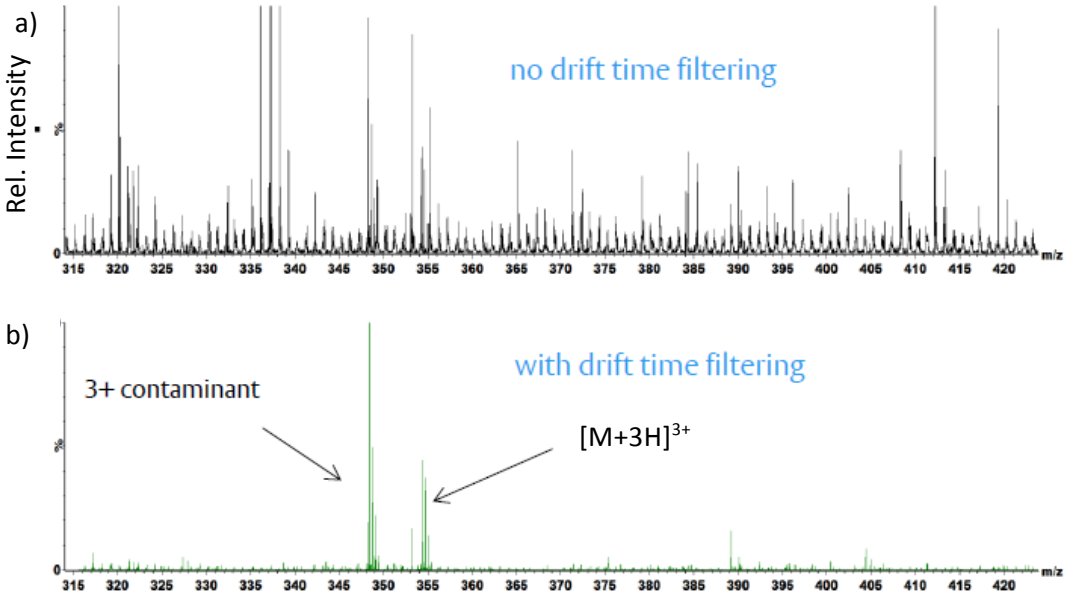

Figure 45 :Liquid AP-MALDI mass spectra of bradykinin a) without and b) with drift time filtering. 1 pmol of bradykinin was loaded. After removal of singly charged ions from the spectrum, the $[M+3H]^3$ions were significantly enhanced.

Figure 46 shows the spectra of bradykinin with and without IMS filtering where the 2+ ions have been selected. The signal:noise ratio was also significantly enhanced to >500:1.

The data shown in Figure 46 were acquired and summed for 3 minutes using a 20Hz laser repetition rate. As an estimate, the sample consumed was less than an order of magnitude of the full MALDI sample droplet. i.e. less than 100 fmol of bradykinin were consumed producing the signal:noise ratio of >500:1.

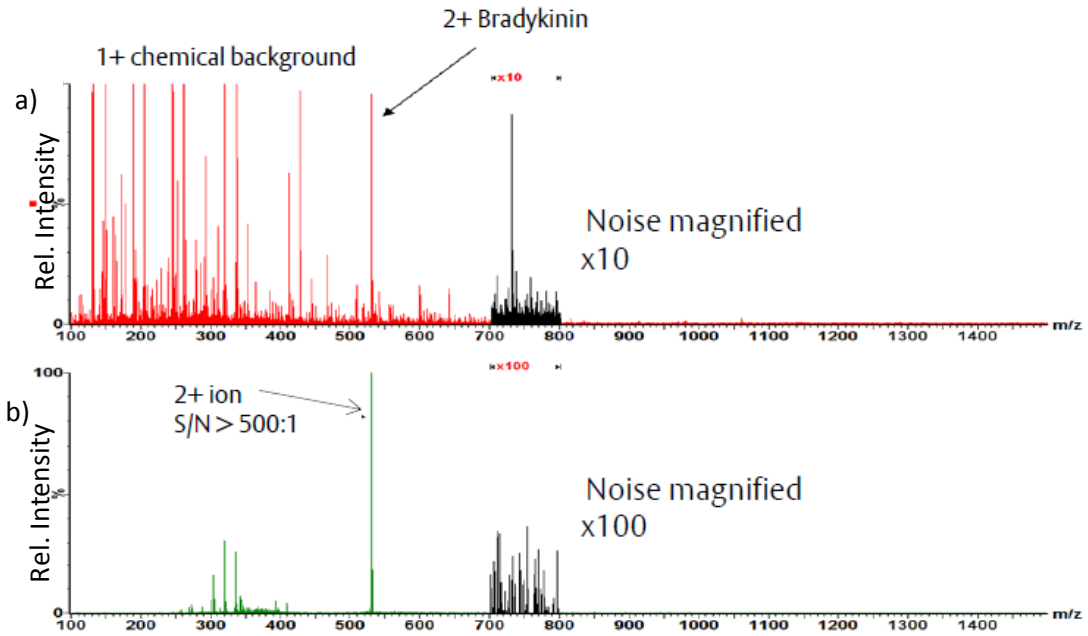

Figure 46: The $[M+2H]^{2+}$ ion signals of bradykinin were enhanced by removing both the $[M+H]^{+}$ ion signal and the $[M+3H]^{3+}$ ion signal from the spectra by drift time filtering, a) is the spectrum without and b) with drift time filtering. The signal:noise was enhanced to approximately 500:1 from the 1 pmol sample of bradykinin. These data were acquired over 3 minutes.

For comparison, the commercial MALDI Synapt G2-Si[119] with conventional crystalline MALDI (at an intermediate pressure of 2 mbar) has a signal:noise ratio specification of 90:1 for a 10 fmol sample loading of Glu-fibrinopeptide, the noise in such experiments originates from chemical background ions. Although this is not the same peptide as was used here, it would indicate that the sensitivity of the liquid AP-MALDI ionisation (with ion mobility drift time filtering) is approaching a similar level of sensitivity (signal:noise ratio) to the commercial MALDI product, but with the added advantage of being able to generate multiply protonated ions for improved MS/MS and with the convenience and simplicity of operating from ambient pressure

4. Results and discussion: Tandem mass spectrometry of multiply protonated MALDI ions

4.1 Electron transfer dissociation (ETD) of liquid AP-MALDI peptide ions

Initial attempts to obtain MS/MS data of peptides from liquid AP-MALDI by ETD generated poor signal-to-noise ratio data with charge-reduced precursor ions rather than informative product ions (as would have been expected from ESI). It became apparent that the ETD reagent anion from p-nitrotoluene from the glow discharge source was very low in abundance compared to the required level. Furthermore, for effective ETD it is necessary to use an reagent anion that is a radical species with low electron affinity so that the electron is more freely available to transfer to the cation analyte.[120] Inspection of the glow discharge reagent spectra revealed that an intense even-electron anion at *m/z* 136 $[M-H]^-$ was being produced and that it was more intense than the required reagent anion at *m/z* 137. Some of the interfering anions were being allowed through into the ETD reaction cell (trap cell) by the quadrupole even though the quadrupole was set for *m/z* 137. The generation of this anion is detrimental to the ETD reaction as the even-electron anion is more likely to extract a proton from the analyte cation than donate an electron to it. Proton transfer in this context, simply reduces the charge of the analyte without fragmentation.[121] In previous work carried out during the development of the commercial ETD system within Waters, it was observed that the diminished radical signal $[M]^{\cdot-}$ as well as the increased $[M-H]^-$ non-radical signal appeared to correlate with air influx into the glow discharge source via the sample cone. Presumably reactions with ambient water vapor and/or oxygen were occurring in this region (data not shown). The detrimental effect is now eliminated on the commercial ETD product by increased

purging of the ESI source inlet housing with dry nitrogen. Unfortunately, the AP-MALDI configuration did not lend itself easily to having an external cover to avoid the intake of ambient air past the glow discharge region. With the liquid AP-MALDI source, experiments were undertaken to ascertain the effect of the cone gas on the generation of the reagent radical. This experiment also ultimately led to the enhancement of liquid AP-MALDI-generated doubly and triply charged ions as their abundance increased with the cone gas flow. This aspect was detailed in the third chapter.

Figure 47 depicts the effect of the cone gas flow on the relative abundance of the radical (*m/z* 137) and even-electron (*m/z* 136) anions from p-nitrotoluene, using negative ion mode and the glow discharge ionisation source. In this experiment, the nitrogen cone gas was increased by 10 L/h every 5 scans (1 second scans). Ultimately, at 200 L/h the radical anion was extremely intense and dominated the even-electron species. Having found an optimum level for the generation of the radical species from the glow discharge source, attempts to observe the higher charge states from liquid AP-MALDI were repeated. As detailed above, the use of cone gas provided a significant enhancement in the sensitivity of the doubly and triply charged ions. Figure 48 (top) shows the glow discharge mass spectrum when acquired with no cone gas, showing dominant even-electron reagent anion peak at m/z 136.1 (loss of hydrogen). The bottom mass spectrum was acquired with 100 L/h cone gas, showing dominant radical reagent anion at m/z 137.1.

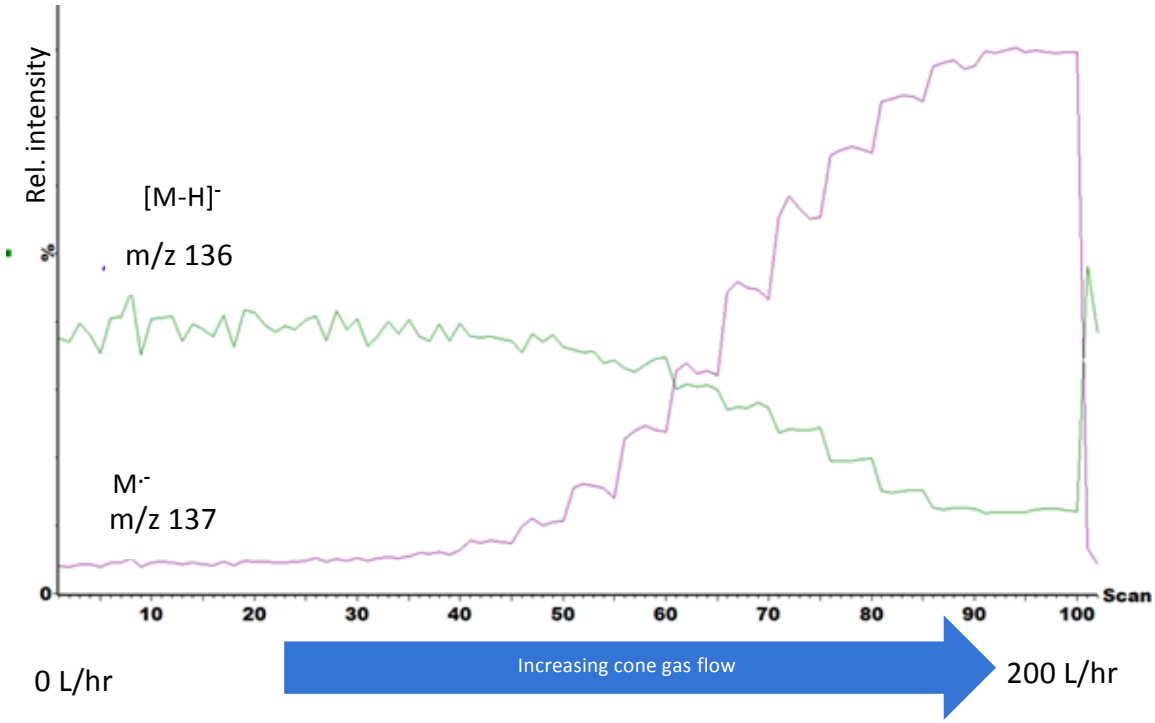

Figure 47: Mass chromatograms of glow discharge anions at m/z 136 (even-electron species) and m/z 137 (radical) from p-nitrotoluene. The cone gas flow was automatically increased by 10 L/h every 5th scan using a WRENS script (example shown in the appendix).

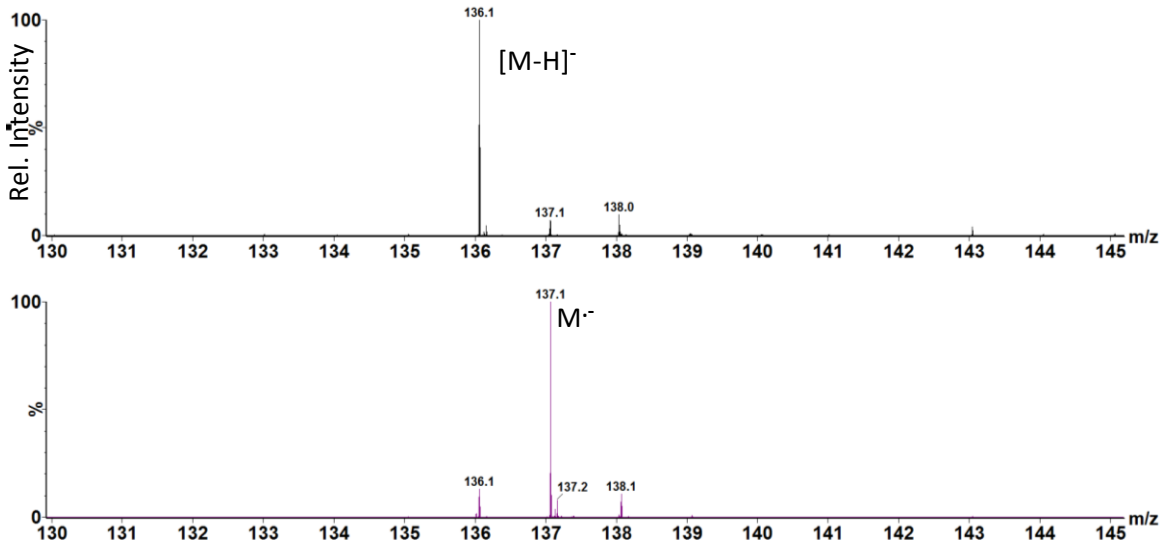

Figure 48: Glow discharge-generated anions. Top mass spectrum was acquired with no cone gas, showing dominant even-electron reagent anion peak at m/z 136.1 (loss of hydrogen). Bottom mass spectrum was acquired with 100 L/h cone gas, showing dominant radical reagent anion at m/z 137.1.

Once the reagent anion abundance was increased using a cone gas setting of ~100 L/h (>10^6 ion counts per second) ETD fragmentation spectra could be more easily obtained with the characteristic c and z ions being generated. Figure 49 shows an ETD MS/MS spectrum from the $[M+3H]^{3+}$ precursor ion of [Val5]-angiotensin I generated by liquid AP-MALDI (15 pmol, CHCA-based liquid matrix) with 200 scans summed. The ETD product ions were annotated using the BioLynx software within MassLynx.

Despite obtaining the ETD MS/MS spectrum shown in Figure 49, the reagent ion generation continued to be problematic and the optimum cone voltage that was required to suppress the even-electron reagent anion changed from day to day, which in turn affected the abundance of higher-charged species from the liquid AP-MALDI source.

Previously ETD has been performed on multiply protonated ions generated by Laserspray,[42] however the laser fluence values reported for the Laserspray technique are very high compared to liquid AP-MALDI. Further development of the liquid AP-MALDI-ETD technique presented here would seem beneficial in order to take advantage of the more efficient sample desorption regime. Further work to isolate the ion source region from ambient air with a purged atmosphere of inert gas should be beneficial in providing a more stable anion reagent current from the glow discharge source.

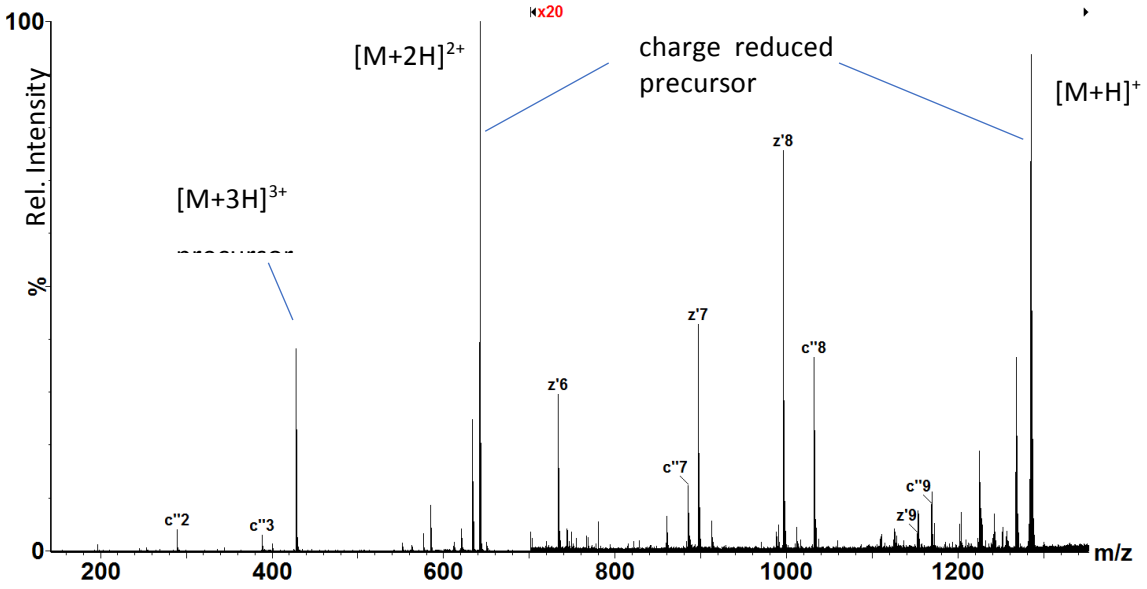

Figure 49: ETD MS/MS spectrum of the $[M+3H]^{3+}$ precursor ion of [Val5]-angiotensin I generated by liquid AP-MALDI (using the CHCA-based liquid matrix) with 200 scans summed. The characteristic c and z ions are annotated.

For comparison to the ETD data, a CID spectrum was acquired from the same triply protonated precursor ion of [Val5]-angiotensin I (using the same CHCA-based liquid matrix). The characteristic b and y type ions were observed in the spectrum (see Figure 50).

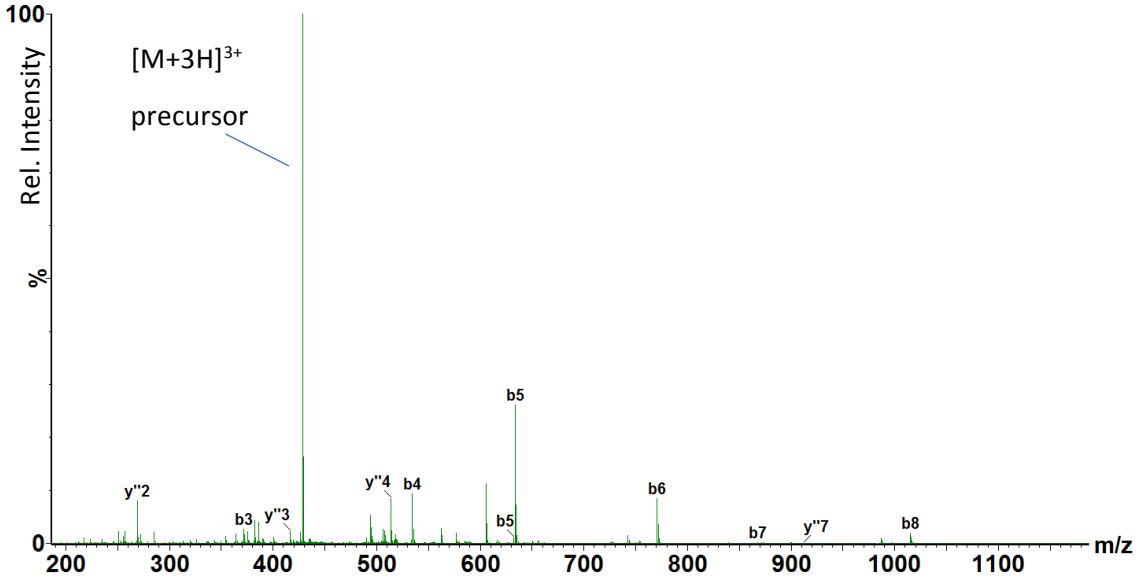

Figure 50: CID MS/MS spectrum of the $[M+3H]^{3+}$ precursor ion of [Val5]-angiotensin I generated by liquid AP-MALDI (using the CHCA-based liquid matrix) with 70 scans summed. The characteristic b and y fragment ions are annotated.

In summary, for ETD, the cone gas improved the radical reagent ion signal, thus allowing more effective ETD to be recorded from liquid AP-MALDI samples. However, optimal conditions changed from day to day probably because of changes in the ambient air. Further development to isolate the ion source from ambient air would be beneficial.

4.2 Electron capture dissociation (ECD) of liquid AP-MALDI peptide ions

One of the drawbacks of the ETD arrangement on the Synapt is that it is only feasible to carry out the ETD reaction before the ion mobility cell because the ion-ion reactions occur over several tens of milliseconds which is incompatible with IMS separation times. Recent developments with a filament-based in-vacuum ECD device suggested that the time scales required for the ECD reaction are only a few microseconds.[102] ECD therefore provides the possibility to perform ECD post IMS and "on the fly" whilst retaining IMS separation. Given the

potential simplicity of the new ECD device, research focus shifted from ETD-IMS to IMS-ECD for the liquid AP-MALDI source. Substance P (25 pmol, DHB-based liquid matrix) was analysed, using the quadrupole in RF-only mode. Ions were allowed to separate in the ion mobility cell and afterwards, were exposed to electrons from the filament of the prototype ECD cell. The heat map of the IMS-ECD data is shown in Figure 51. The band of ions within the region A were singly charged ions that were produced within the ion source or were possibly generated in the trap cell (despite the collision energy being set at a low level of 2 V per charge). Many of the singly charged ions would have been neutralised by the electrons within the ECD cell so the ions in A are the remaining ions that did not interact with the electrons. The region B depicts the doubly charged ions that were generated in the ion source. Within band B is an intense doubly charged ion at $[M+2H]^{2+}$ labelled C at *m/z* 674.4. Region D, being vertical, has the same drift time as the ion at C and these ions are singly and doubly charged product ions from the ECD process. The data also include a set of ions (E) that appear to originate directly from the ECD cell as they are present at all drift times.

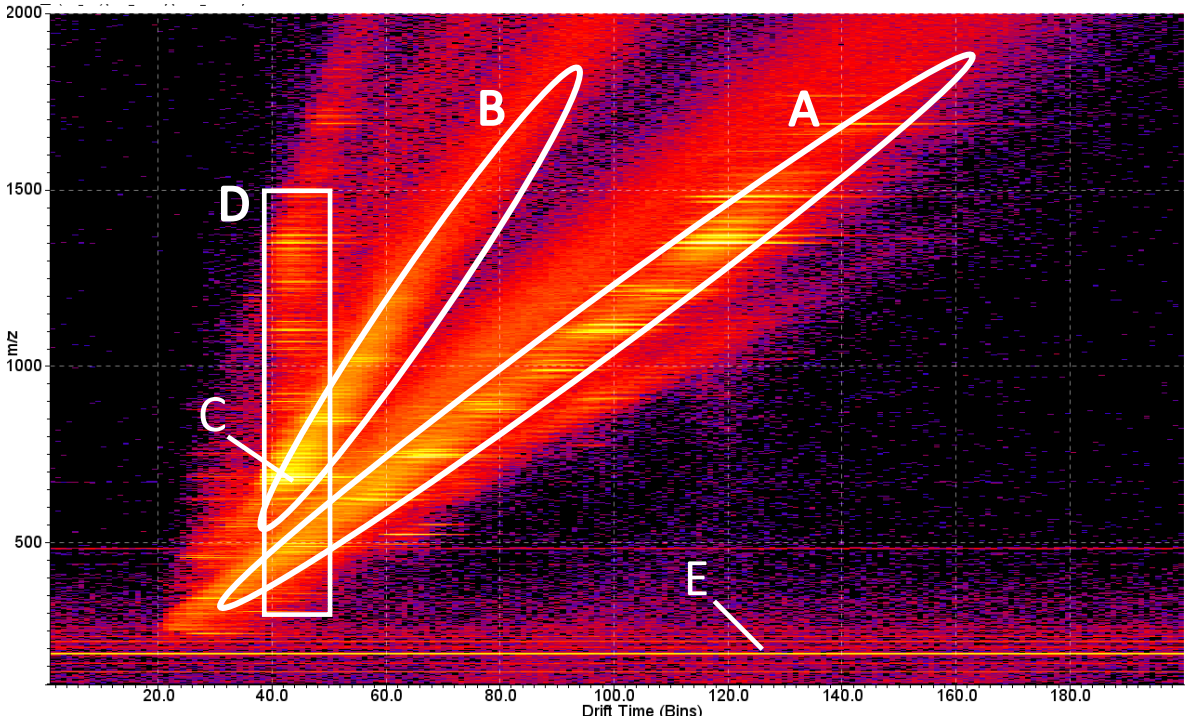

Figure 51. Heat map data from liquid AP-MALDI ion mobility with ECD cell active. The amount of substance P loaded was 25 pmol in a 1-µL MALDI sample droplet. The quadrupole was operating in RF-only mode, the laser pulse repetition rate was 200 Hz. In region A are the singly charged ion signals and in region B are the signals of the doubly charged ions (separated by mobility). The doubly charged $[M+2H]^{2+}$ ion at m/z 674.4 (labelled C), was the most intense ion and produced a vertical band of ECD product ions (region D). In addition, several lines of ions which were not separated by IMS can be observed (E), see Figure 52.

Further analysis revealed that the E ions originated directly from the rhenium filament as their *m/z* values matched within 0.2 mDa and had isotope abundances within 10% of the theoretical values of the natural rhenium isotope distribution. The obtained mass spectrum of the rhenium ions is shown in Figure 52. Furthermore, these ions were only detected when the ECD filament was switched on. Fortunately, their *m/z* values are quite low and did not interfere with the product ion data.

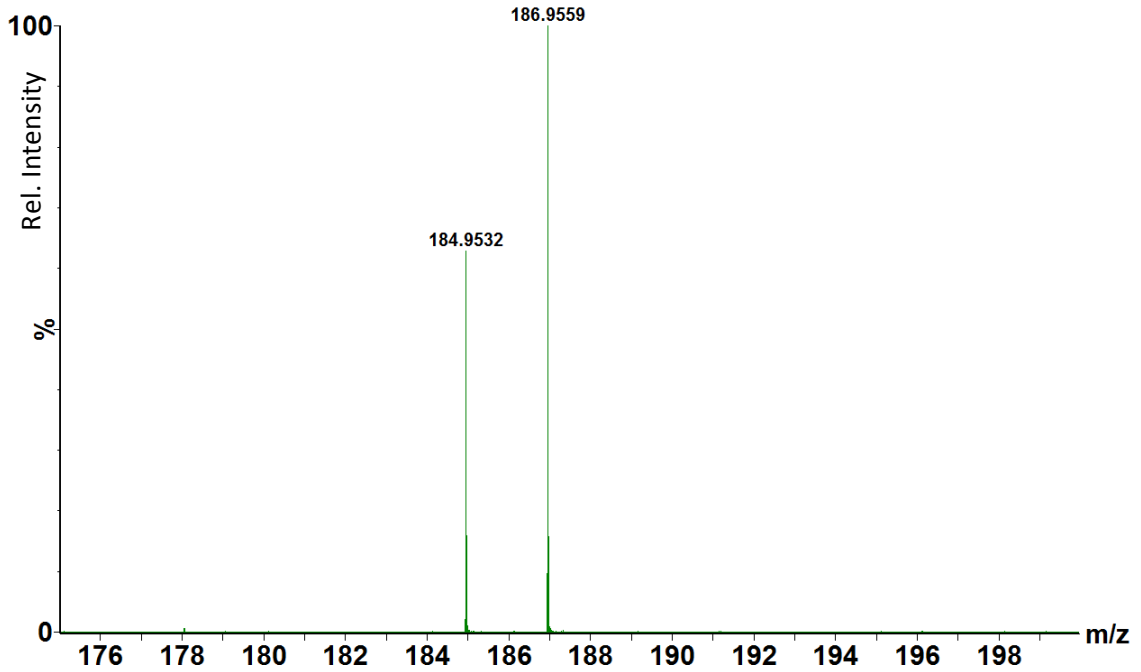

Figure 52: Selection of the lower m/z region, displaying ions that were not separated by ion mobility, revealed that they originated from the rhenium filament of the ECD cell. The m/z values of 184.95 and m/z 186.96 matched the theoretical m/z values within 0.2 mDa. Furthermore, their isotope abundances were within 10% of the theoretical natural isotope distribution of rhenium.

Figure 53 displays a mass spectrum for the ions from band D of Figure 51. Several c and z type ECD product ions can be seen. However, due to the overlapping drift times for ions of singly and doubly charged origin, all the ions observed in the product ion spectra cannot be directly attributed to the particular $[M+2H]^{2+}$ precursor of substance P as would have been expected in a true MS/MS experiment in which the quadrupole selects the precursor. To simplify the experiment, and improve the ECD data, the quadrupole was set to select the $[M+2H]^{2+}$ ions from substance P (true MS/MS). The quality of the ECD product ion data was substantially improved as can be seen in the spectrum of Figure 54.

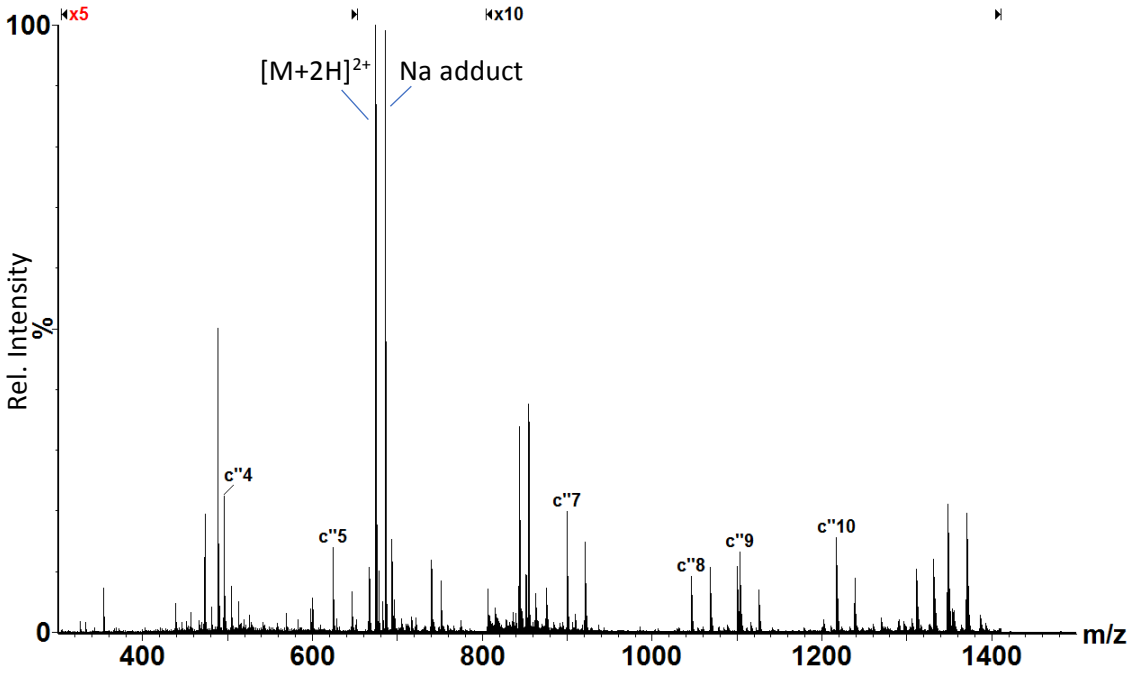

Figure 53: Mass spectrum of the extracted mobility range of band D from Figure 51. Several c'' ions were observed indicating that ECD of the liquid AP-MALDI ions was occurring. However, in addition, interferences from other ions that had the same drift time are seen in the spectrum.

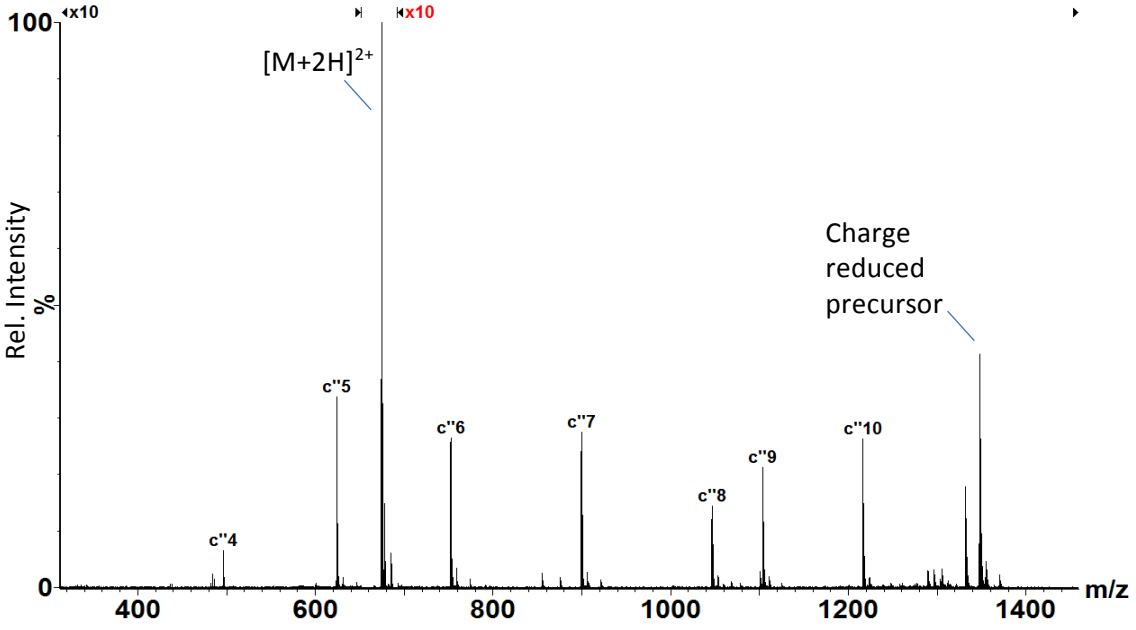

Figure 54: ECD MS/MS data of the quadrupole-selected $[M+2H]^{2+}$ substance P ion at m/z 674.4. After passing through the ion mobility cell these precursor ions were subject to ECD. The experimental difference between this figure and Figure 53 was that the quadrupole was used to select the precursor ion which removed many of the interfering ions.

It was observed that the efficiency of the ECD reaction would change significantly when the filament bias voltage was changed. The efficiency was not fully quantified in these

experiments as further carefully controlled experiments were required (and it was not the focus of this thesis). However, as an approximation for the $[M+2H]^{2+}$ ions of substance P (by ESI or MALDI), the sum of the fragment ion intensities divided by the precursor ion intensity was typically 5%. However, some tuning parameters were quite critical in terms of their effect on efficiency (for example, filament bias - see Figure 55). It was also observed that when the ECD fragments were most efficiently generated, there was some slight tailing of the precursor and product ion drift times suggesting that the ions were being slowed during their trajectories through the ECD device.

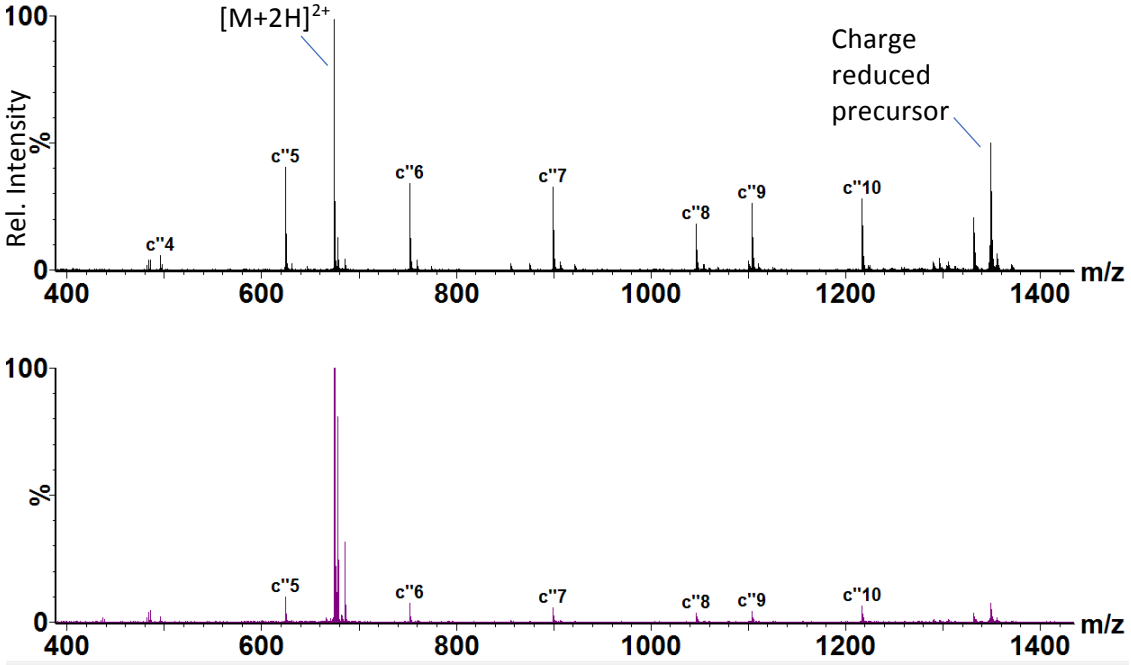

Figure 55: Liquid AP-MALDI MS/MS spectrum of substance P after selection of the $[M+2H]^{2+}$ ion at m/z 674.4 followed by IMS then ECD. The top spectrum was acquired with the ECD cell filament bias at 0.2 V whereas the lower spectrum was with the bias at 1.0 V. The sum of 60 scans was used for each spectrum. For comparison, 100% ion signal intensity is based on the signal intensity of the $[M+2H]^{2+}$ precursor ion in the top spectrum.

4.3 Comparison of ESI with liquid AP-MALDI with respect to ECD and CID of peptide ions

Both post-IMS ECD and pre-IMS CID product ion data for several peptides were recorded from both ESI and liquid AP-MALDI sources. The quadrupole was programmed to select the $[M+2H]^{2+}$ precursor ions for substance P and bradykinin and the $[M+H+Na]^{2+}$ sodium adduct ion for [Val5] Angiotensin 1. Peptide sample loadings were 25 pmol in a 1-µL sample droplet for liquid AP-MALDI (using the DHB-based liquid matrix). The laser pulse repetition rate was set at either 200 Hz or 400 Hz and approximately 3 minutes of spectra were accumulated. Drift time filtering was applied to select the parent and product ions and a cone gas flow of 140 L/h was employed in ECD mode. In ESI, default tuning settings were applied, and the infusion flow rate was 5 µL/min using a 2.5pmol/µL analyte solution. Approximately 1 minute of spectral data were accumulated.

4.3.1 ECD MS/MS data from ESI and liquid AP-MALDI ions

Figure 56, Figure 57 and Figure 58 display the post-IM ECD MS/MS spectra for ESI (top spectra) and liquid AP-MALDI (bottom spectra).

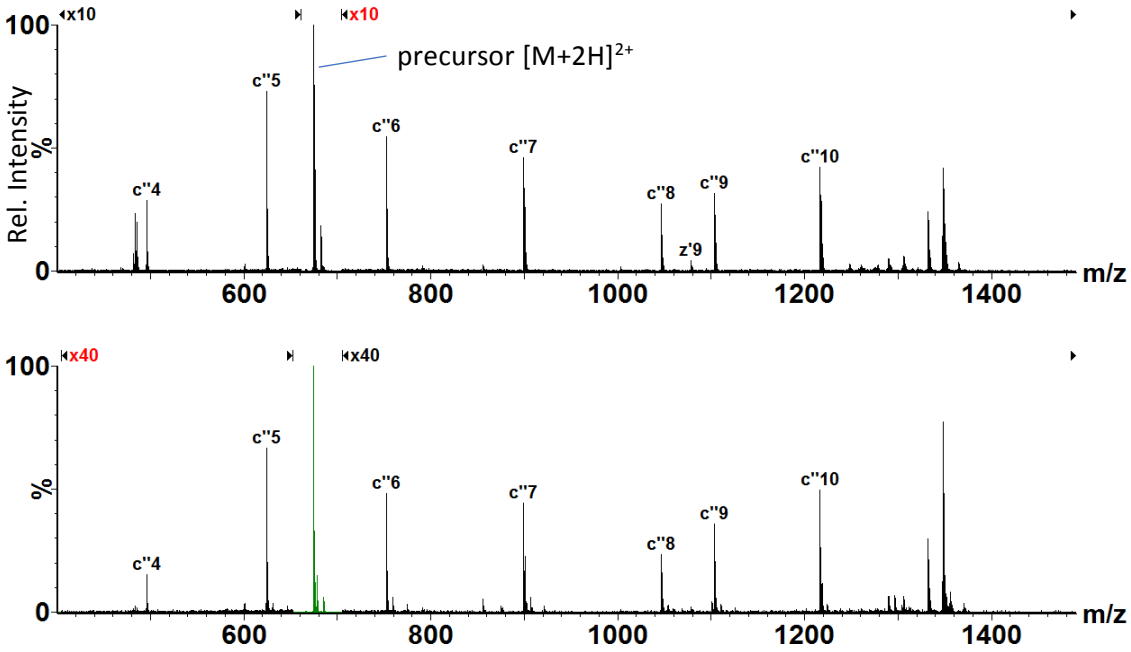

Figure 56: IMS-ECD-TOF MS/MS spectra of the substance P $[M+2H]^{2+}$ ion by ESI (top) and liquid AP-MALDI (bottom).

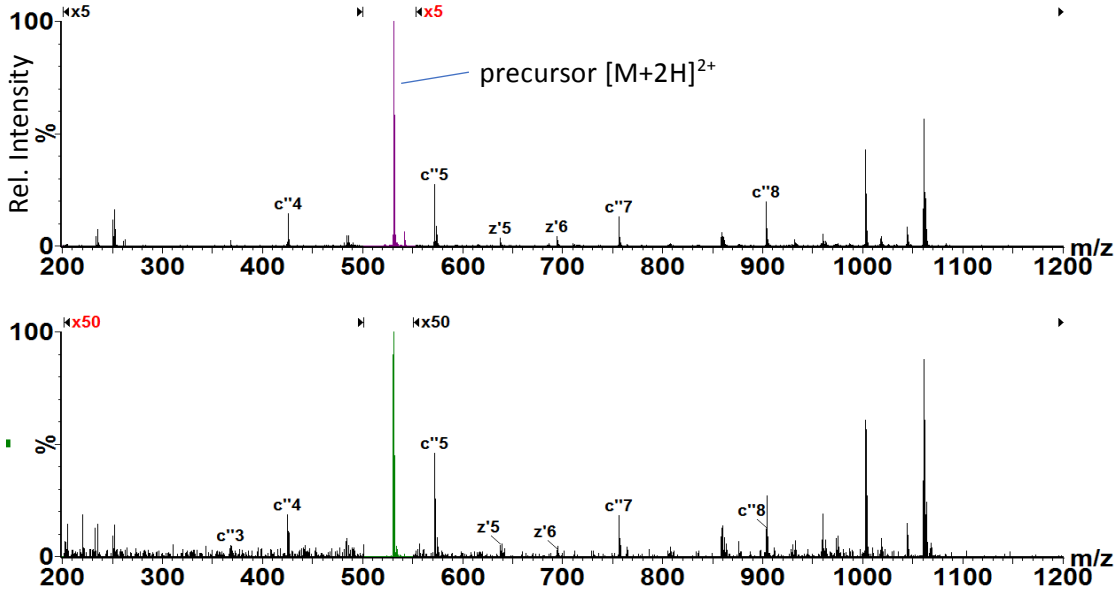

Figure 57: IMS-ECD-TOF MS/MS spectra of the bradykinin $[M+2H]^{2+}$ ion by ESI (top) and liquid AP-MALDI (bottom).

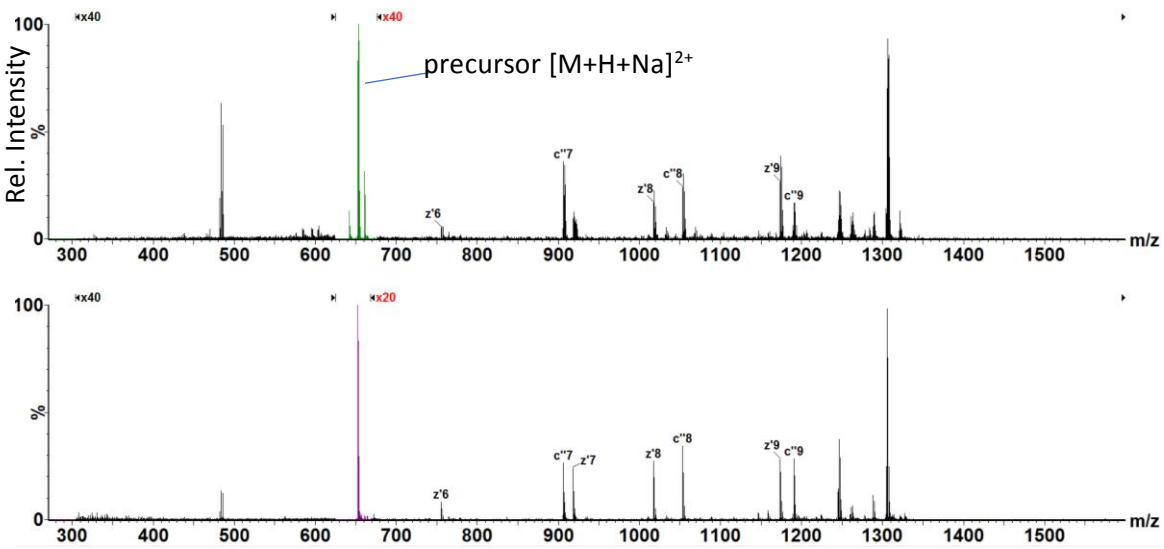

Figure 58: IMS-ECD-TOF MS/MS spectra of the [Val5] angiotensin $[M+H+Na]^{2+}$ ion by ESI (top) and liquid AP-MALDI (bottom).

For each spectrum, magnification factors were applied to similar *m/z* regions so that the overall distribution of product ions can be easily compared. Although there were differences in magnification factors between ESI-ECD and liquid AP-MALDI-ECD these differences were related to detector saturation of the precursor ions when using ESI as well as sub-optimal tuning of the ECD device. (N.B. the ECD device was a research prototype and further development is underway to develop an autotune algorithm). From the data, it appears that the type of c'' or z' ECD product ions and their relative abundance were remarkably similar between ESI and liquid AP-MALDI generated ions.

Overall, it can be noted that there is virtually no qualitative difference between ESI-ECD MS/MS and liquid AP-MALDI-ECD MS/MS, indicating that no memory effect with respect to ion formation is evident.

4.3.2 CID MS/MS data from ESI and liquid AP-MALDI ions

For the CID experiments, the trap collision energy was manually adjusted in order to produce a balance of CID fragments across the *m/z* range. Figure 59, Figure 60 and Figure 61 display the pre-IM CID MS/MS spectra for ESI (top spectra) and liquid AP-MALDI (bottom spectra).

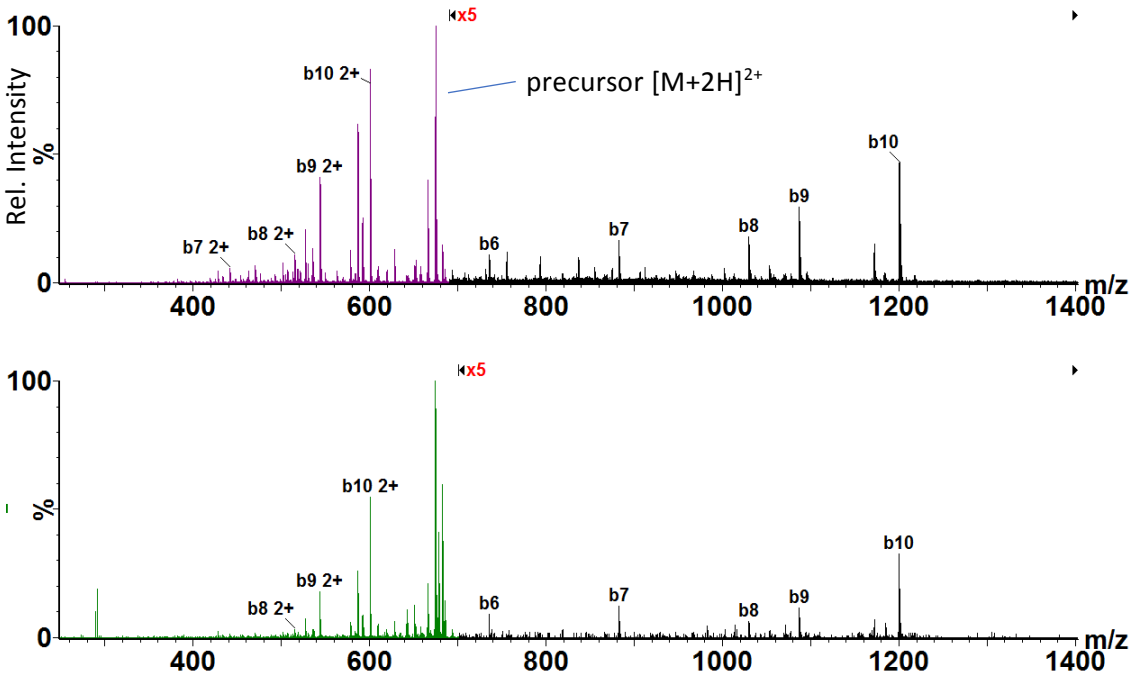

Figure 59: CID-IMS-TOF MS/MS spectra of the substance P $[M+2H]^{2+}$ ion by ESI (top) and liquid AP-MALDI (bottom). A trap collision energy of 27 V was applied.

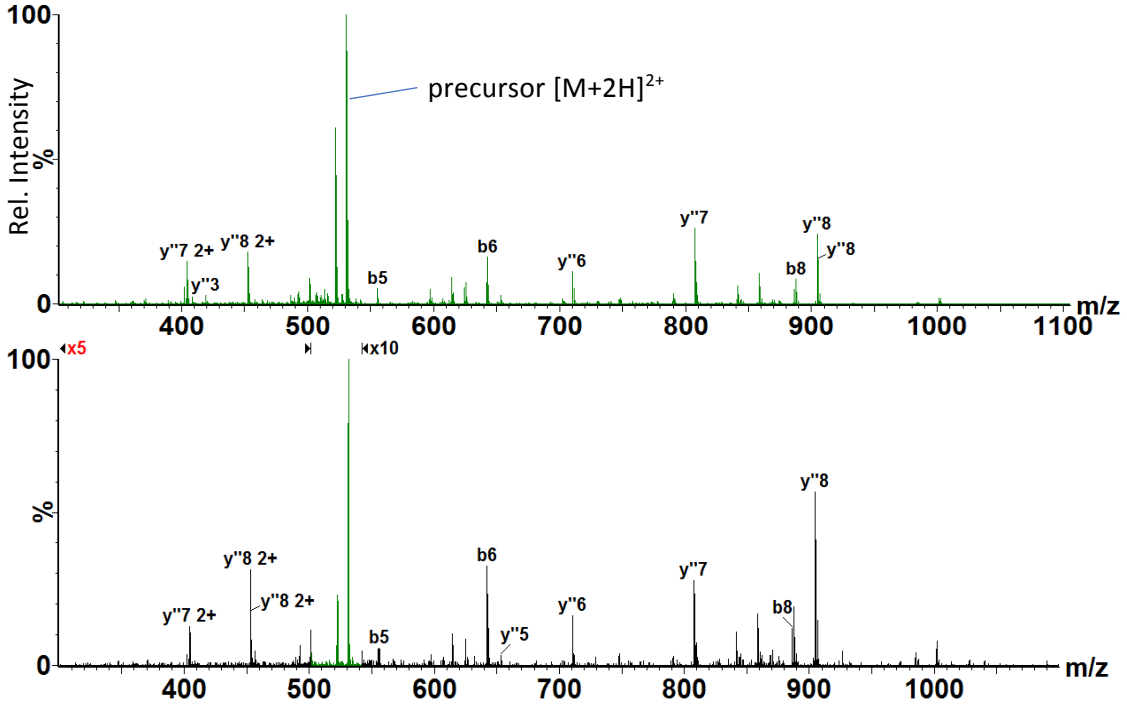

Figure 60: CID-IMS-TOF MS/MS spectra of the bradykinin $[M+2H]^{2+}$ ion by ESI (top) and liquid AP-MALDI (bottom). In both cases a trap collision energy of 20 V was applied.

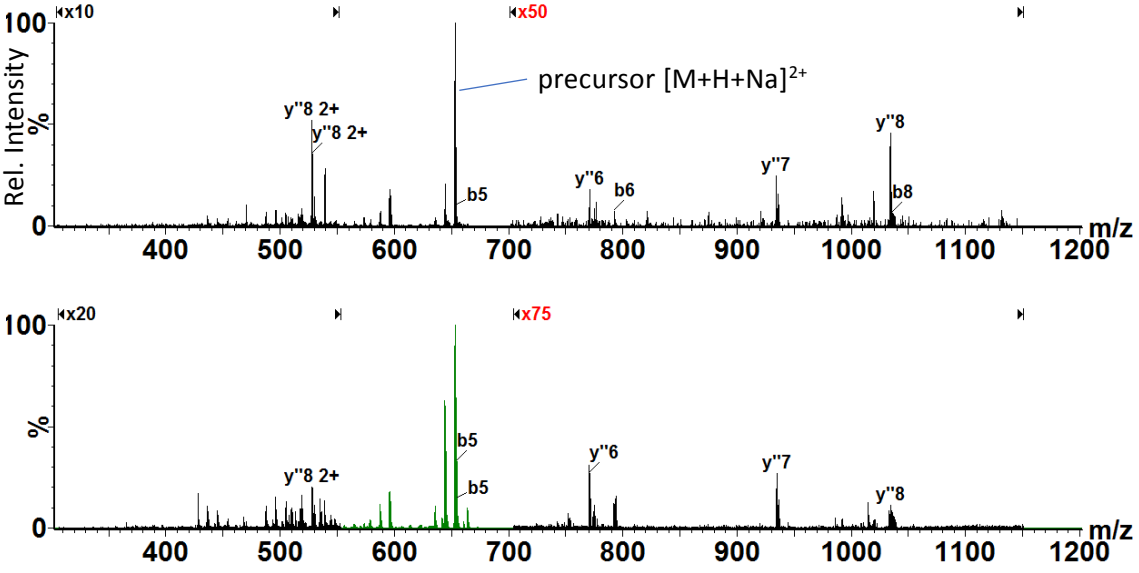

Figure 61: CID-IMS-TOF MS/MS spectra of the [Val5] angiotensin $[M+H+Na]^{2+}$ ion by ESI (top) and liquid AP-MALDI (bottom). In both cases a trap collision energy of 20 V was applied.

Just like the ECD data above, the type of b or y'' CID product ions and relative abundance were very similar between ESI and liquid AP-MALDI-generated ions. As in the ECD spectra, the

magnification factors for the fragment ions within the spectra are generally higher for the liquid AP-MALDI spectra compared with the ESI spectra. Again, this was attributed to detector saturation effects which caused the ESI MS/MS fragmentation to appear more efficient. (i.e. the intensity of the precursor ions were not underrepresented in comparison to the fragment ion intensities). Overall, the fragmentation data obtained by both ECD and CID suggests that the liquid AP-MALDI ion source may be used as an alternative to ESI for MS/MS analyses of peptides.

Although not described above, the acquisition of ECD data from higher charged peptides presented some difficulties in that the ECD spectra were often "polluted" with CID fragment ions due to inadvertent collisional activation (with the argon collision gas from the transfer cell) whilst ions were leaving the ECD cell. To mitigate this, helium buffer gas (rather than argon) within the transfer cell to reduce the centre of mass collision energy should be beneficial.

The data presented in this thesis is not the first report of ECD of MALDI generated ions, as previously, Frankevich[122] showed that a sufficient quantity of multiply charged ions could be generated from an electron-free PEEK substrate to provide an ECD spectrum. However, the experiment was performed with an FTICR mass spectrometer and required 3 seconds of electron irradiation. In this thesis, the combined experiment of liquid AP-MALDI-IMS-ECD-TOF has been demonstrated (for the first time) and was fast enough to generate fragmentation data "on the fly" after ion mobility. Although the efficiency of the ECD fragmentation data is low (~5 percent) further optimisation and development of the cell is likely.

5. The potential of liquid AP-MALDI for ultra-high throughput sample acquisition rates

5.1 Effect of laser pulse repetition rate on the generation of liquid AP-MALDI ion signals

It was shown in chapter 3 that there was an optimum laser pulse energy producing the highest ion signal per pulse. For high sample throughput, the laser repetition rate needs to be increased whilst maintaining this optimum laser pulse energy to obtain the maximum sensitivity per sample. However, if the concentration of analyte is low, the number of laser pulses per sample will also need to be increased to obtain adequate signals, potentially reducing the sample throughput rate. For such applications it might be necessary to completely deplete the sample droplet to record as many analyte ions as possible before moving to the next sample.

Liquid AP-MALDI MS experiments were carried out to characterise the effects on performance when operating the laser at higher pulse repetition rates (up to 5kHz). For simplicity, these experiments were carried out on the same sample droplet without the added complexity of moving the sample plate. Figure 62 shows the mass chromatogram for the $[M+2H]^{2+}$ ion signal from bradykinin at increasing laser pulse repetition rates of up to 1 kHz. The data were acquired from a 1 µL MALDI sample droplet using the DHB-based liquid matrix (5 pmol total loading of bradykinin). The laser energy was set at 17 µJ per shot and the laser diode current was manually increased for the rates above 300 Hz to ensure that the energy per laser pulse remained constant throughout the experiment. It can be seen from the chromatogram that

the ion signal per unit time increased linearly with the pulse repetition rate. To further illustrate this relationship, at each laser pulse repetition rate setting, 20 seconds of spectra were summed and the intensity of the $[M+2H]^{2+}$ ion was plotted against the laser pulse repetition rate (see Figure 63). A straight line fit of ion signal per unit time versus laser pulse repetition rate had an R^2 fit of 0.9919. (Error bars were approximated at +/-15% based on the signal variation of the mass chromatogram in Figure 62.)

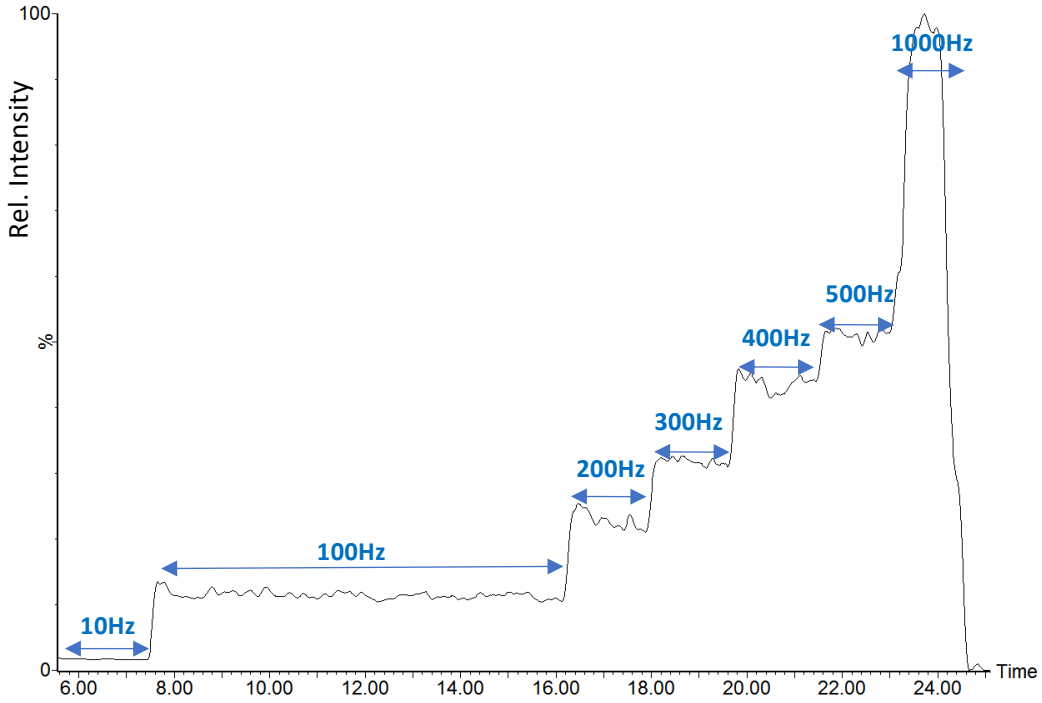

Figure 62: Mass chromatogram for the $[M+2H]^{2+}$ bradykinin ion signal for increasing laser pulse repetition rates between 10Hz to 1kHz from a 1 µL sample droplet.

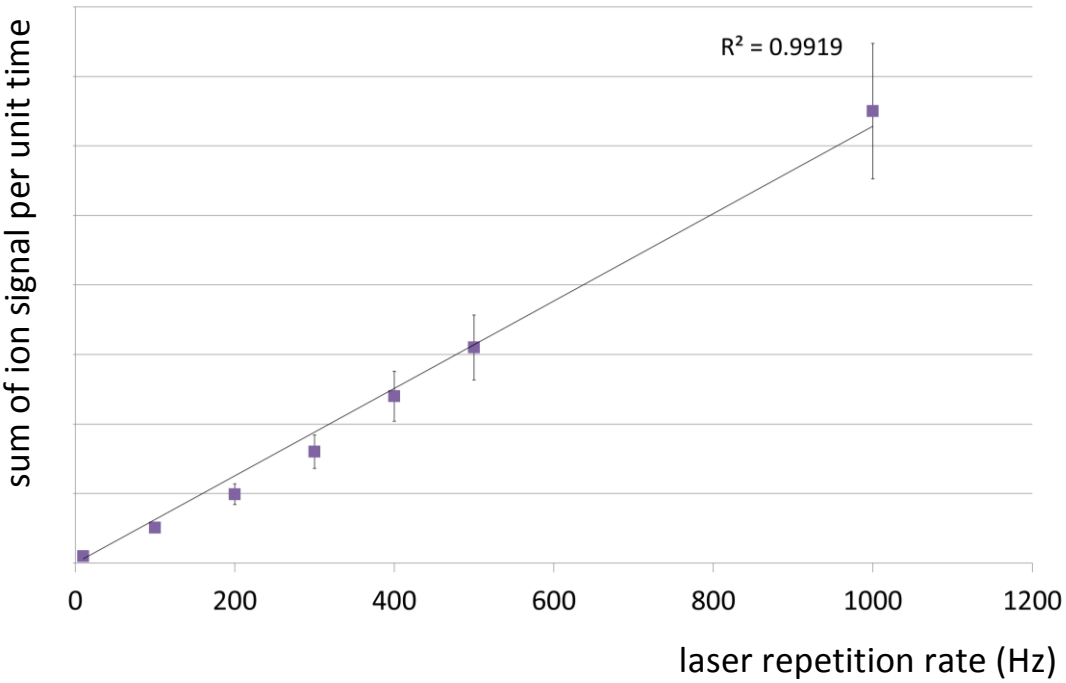

Figure 63: $[M+2H]^{2+}$ bradykinin ion signal per unit time (arbitrary units) as a function of laser pulse repetition rate up to 1kHz (at 16 µJ per shot). For each data point 20 seconds of data were summed. Data were obtained from Figure 62. A linear fit had an R^2 value of 0.9919

For a bradykinin loading of 5pmol, Figure 64 shows a comparison of the combined ion signal from 1000 successive laser pulses obtained with laser pulse repetition rates of 10 Hz, 100 Hz and 1 kHz. The vertical scales for each of the three spectra were the same and there were no apparent differences in the signal and noise levels at these differing rates.

Unfortunately, systematic measurements above 1kHz, for more than a few minutes, were less practical due to the higher sample consumption rate. To avoid the excessive depletion limiting the measurements, larger matrix/sample volumes (~10 µL) were loaded (with the same analyte concentration).

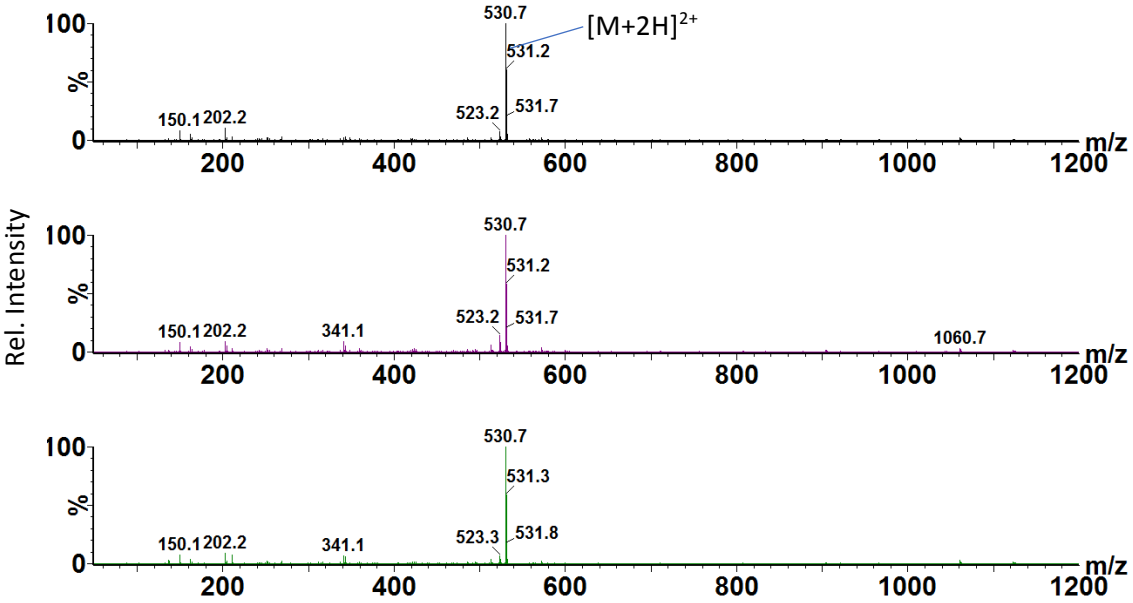

Figure 64: Bradykinin mass spectra acquired at different pulse repetition rates. The ion signal from 1000 successive laser pulses for each spectrum. In the top spectrum - 100 scans were summed when running at 10Hz laser pulse repetition rate. In the middle spectrum - 10 scans summed when running at 100Hz and in the bottom spectrum a single scan is displayed when running at 1kHz. The vertical scales for each spectrum were the same indicating very similar counts for the base peak for each repetition rate. (The same raw data as used as in Figure 62 and Figure 63.)

Figure 65 shows the mass chromatogram signals of the $[M+2H]^{2+}$ bradykinin ion as the laser pulse repetition rate was (a) increased from 1 kHz to 5 kHz and then (b) reduced from 5 kHz to 1 kHz in 1 kHz steps. The ion signals of 20 seconds of this data were summed, i.e. 10 seconds from the increasing and 10 seconds from the reducing laser repetition rates.

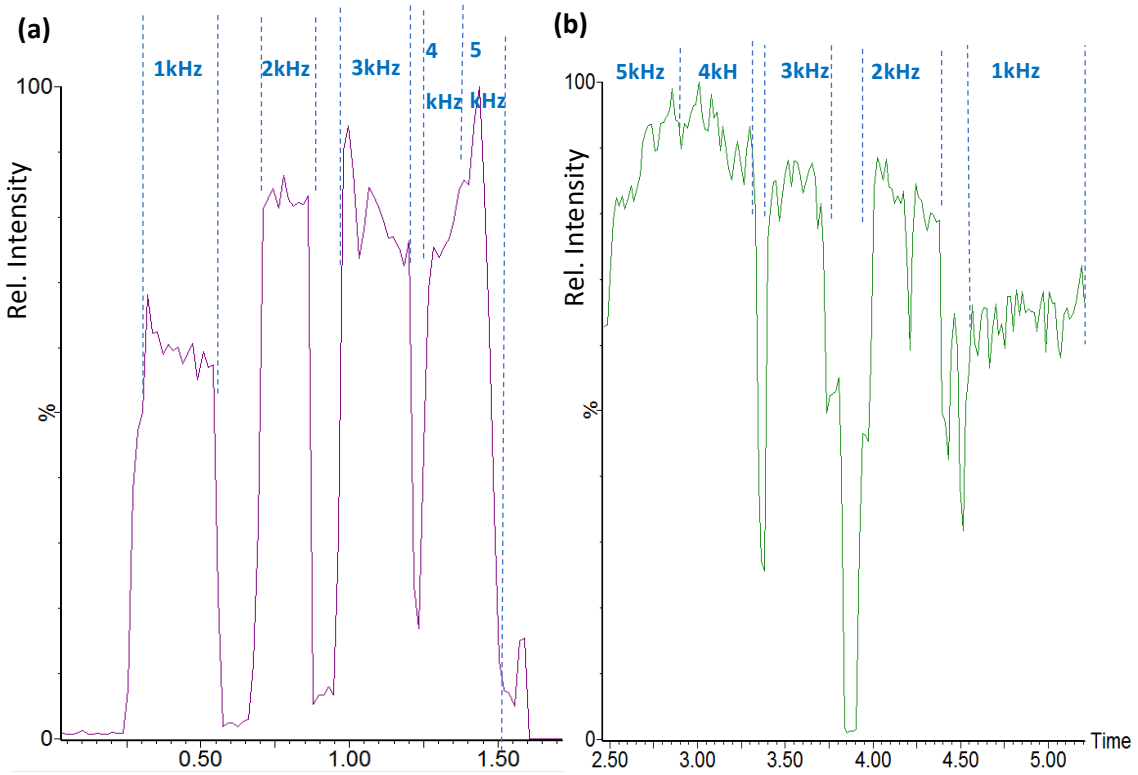

Figure 65: Mass chromatogram for the $[M+2H]^{2+}$ bradykinin signal when (a) increasing laser pulse repetition rates between 1 kHz to 5kHz and (b) when reducing repetition rate from 5kHz to 1kHz. Note the excessive signal fluctuation compared to Figure 63.

The summed ion signals per unit time for 1 kHz to 5 kHz are plotted in Figure 66. Error bars were approximated from the chromatographic variation in Figure 65 of less than +/-15%. Similar spectral data were obtained between 1 kHz and 5 kHz (not shown). As can be seen from this data (Figure 66), for laser pulse repetition rates beyond 1 kHz up to the maximum of 5 kHz, the doubly protonated bradykinin ion signal became less reproducible and reached a plateau (i.e. the ion signal per unit time stayed approximately constant beyond 2 kHz).

Although the ion signal per unit time increased linearly up to 1kHz, it was relatively flat in profile above this value (see Figure 66). One factor to consider is that the laser pulse duration reduces with increasing diode current. As described in chapter 2, the laser energy per pulse was kept constant by manually increasing the laser diode current. Therefore, reduced laser pulse durations could have been a factor affecting ion and/or droplet size and yield during

desorption. Another factor may have been that the MALDI sample droplet was being physically changed in a way that resulted in a less efficient self-healing process. It would be of benefit for high throughput sample acquisition research to further understand the possibilities of using laser pulse repetition >1kHz. Despite the limitations, operating the laser at 1000 Hz rather than 20 Hz increased the signal per unit time by 50 times which will be advantageous when acquiring at higher sample throughput rates.

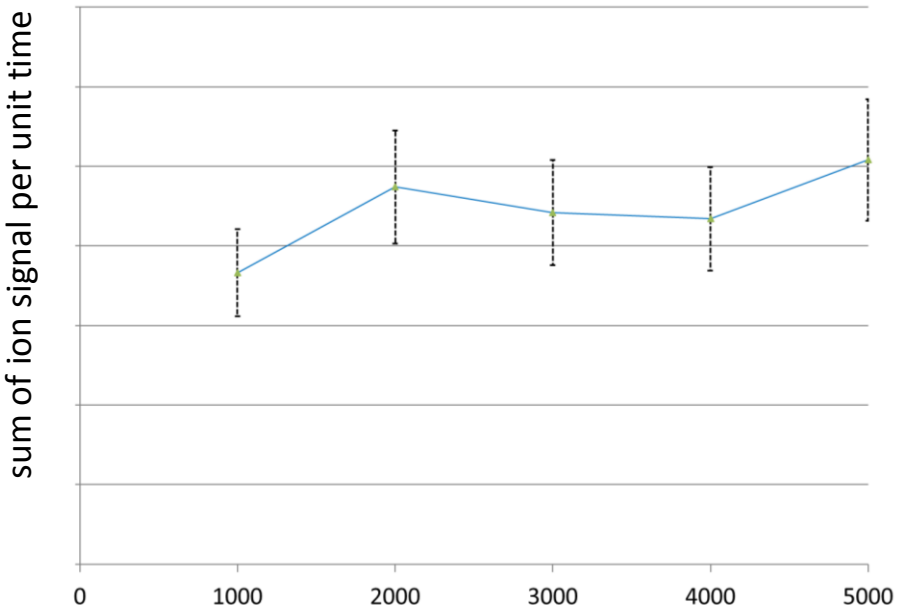

Figure 66: The doubly protonated bradykinin signals generated between 1 kHz and 5 kHz laser pulse repetition rate. Between 2kHz and 5kHz signal per unit time was approximately constant (error bars +/- 15%).

5.2 Fast data system acquisition from the same sample/matrix droplet

High throughput analysis using mass spectrometry is of great interest to the pharmaceutical and biotechnology industries as well as for health and disease monitoring. Furthermore, MS based approaches being highly informative, have the potential to reduce the number of false

positives or negatives whilst avoiding the use of some (sometimes costly) fluorescence-based dyes and reagents.[123]

Even though TOF mass analysers are very well suited to the measurement of high-speed processes, the data system must be able to cope with the higher volumes of data per unit time. In addition, the spatial position of the sample plate, and the indexing of data files must be well synchronised so that each data file can be indexed to a sample. At higher sample throughput rates, small delays or timing inconsistencies can be problematic. Fortunately, ion imaging by conventional MALDI has already addressed this problem to a certain extent, as each pixel may be considered as a separate sample. For liquid MALDI sample droplets there are differences in terms of the optimum XY sample plate format (sample distribution density), the plate movement control as well as the number of laser pulses per sample.

The DIA "SONAR" software was modified to work with the Synapt G2-Si. The software was modified to acquire repeating streams of 200 spectra separated by one "inter-scanning delay" of ~10ms (prior to the modification there would have been 200 interscan delays, i.e. one per spectrum). In this software, 1 "scan" therefore consists of 200 separate spectra. Unlike conventional SONAR mode, the quadrupole scanning functionality was disabled to allow conventional MS/MS or RF only full *m/z* range transmission. Each set of 200 spectra could be acquired over timescales as short as 0.1 seconds thus allowing effective spectral rates of up to two thousand per second (with minimal data losses during the single inter-scan delay). The extra speed afforded by the software modifications allowed observation of the time profile of liquid AP-MALDI signals from single laser pulses.

Figure 67 shows data presented within the Synapt user interface whilst operating the laser at 10 Hz and acquiring 200 spectra every second from a 1 µL MALDI sample droplet of bradykinin

(17 pmol loaded). Figure 67(a) is the accumulated spectrum from the 10 laser pulses. Figure 67(b) shows the *m/z* chromatogram for the $[M+2H]^{2+}$ signals seen over the second.

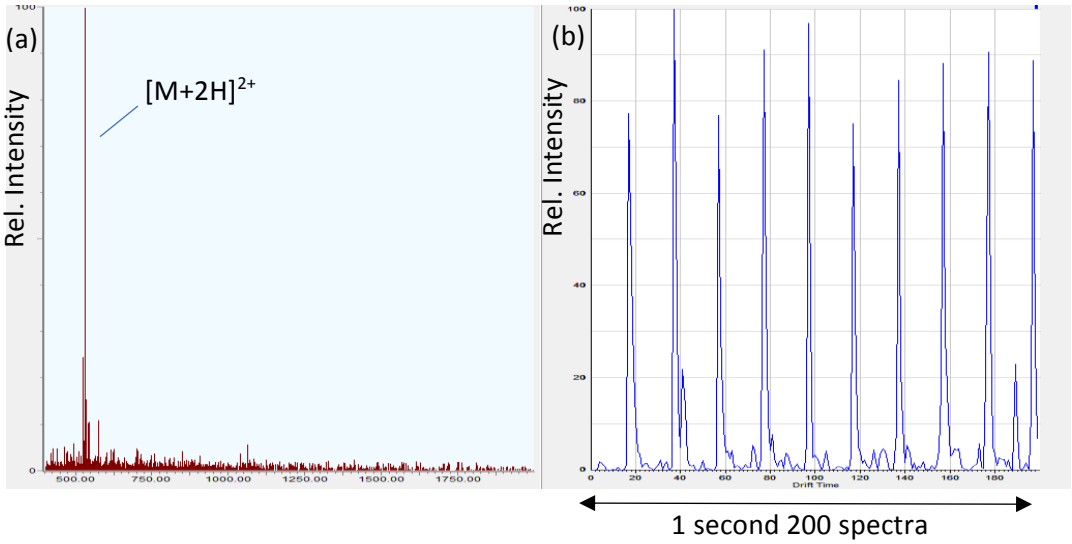

Figure 67: Synapt user interface screen shot of the modified SONAR software: (a) a spectrum from the ion signal accumulation of 10 laser pulses (per second) from bradykinin (17 pmol loaded) from a 1 µL MALDI sample using the DHB-based liquid matrix and (b) the $[M+2H]^{2+}$ bradykinin ion signal chromatogram over 1 second, clearly showing the 10 individual laser pulses (200 spectra in 1 second).

Figure 68 shows the Synapt user interface when operating the laser at 50 Hz whilst acquiring 200 spectra every second from a 1 µL MALDI sample droplet of bradykinin (17 pmol loaded). Figure 68(a) is the accumulated spectrum from the 50 laser pulses. Figure 68(b) shows the m/z chromatogram for the $[M+2H]^{2+}$ signals seen over the second. It appears from the data that also at 50 Hz individual laser pulse signals provided separated signals.

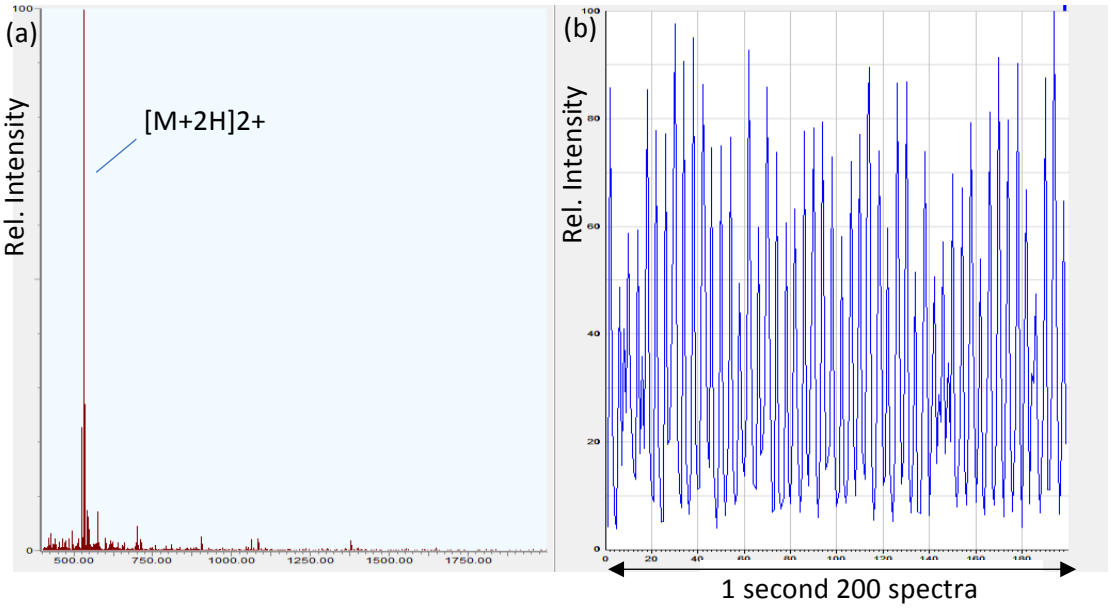

Figure 68: Synapt user interface screen shot of the modified SONAR software: (a) a spectrum from the accumulation of 50 laser pulses (per second) from bradykinin (17pmol loaded) from a 1-µL MALDI sample using the DHB-based liquid matrix and (b) the $[M+2H]^{2+}$ m/z chromatogram over 1 second, showing the 50 individual laser pulses (200 spectra in 1 second).

The Driftscope software (previously used for IMS data) was used to visualise the acquisition of data at increasing laser pulse repetition and spectral acquisition rates (see Figure 69). Areas with different laser pulse repetition rates are separated by dashed lines. The x-axis shows the MS scan number in seconds. The MS system was recording at 1 scan per second (0.986 scan with 0.014 ISD), on the y-axis, each scan was split into 200 spectra (i.e. 1 spectrum every 5 ms). The ion abundance lines are not horizontal because of slight differences between the laser pulse repetition rate and the data system acquisition rate. At this data acquisition rate, it was possible to see discrete separation of the ion signals for each laser pulse at approximately 50 Hz.

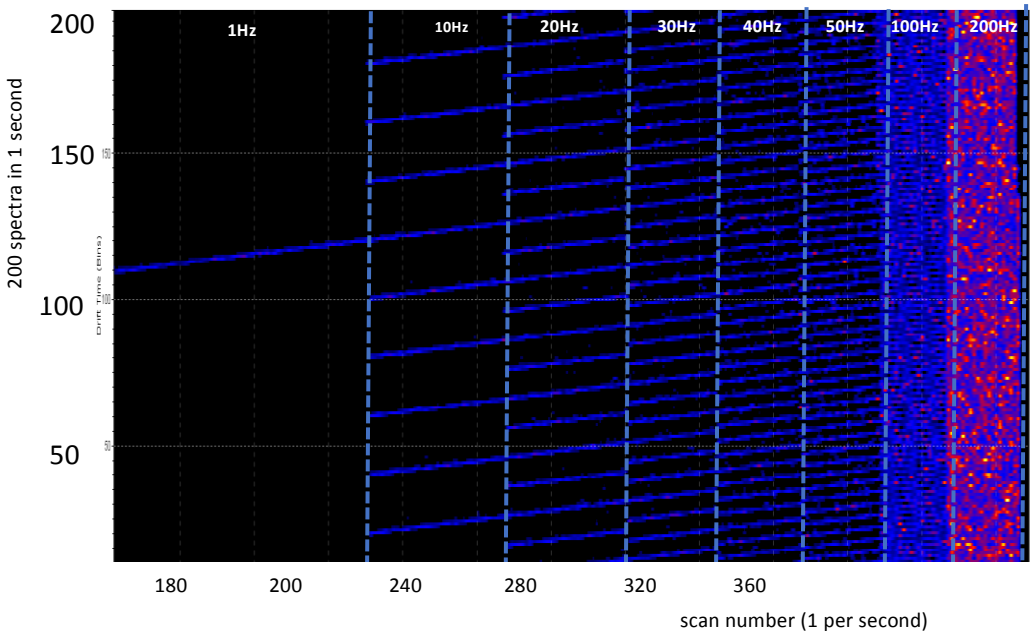

Figure 69: Heat map of the $[M+2H]^{2+}$ bradykinin ion signals for increasing laser pulse repetition rates. Regions of differing repetition rates are separated by dashed vertical lines. The x-axis represents the scan number (0.986 second per scan with 14 ms ISD) and the y-axis represents the spectra 1 – 200 (i.e. ~200 spectra/second). Discrete separation of ion signals was still seen with a laser pulse repetition rate of 50 Hz; at 100 Hz signals were overlapping.

In Figure 70 the spectral acquisition rate was increased to approximately 1000 spectra per second, with the vertical scale corresponding to 200 spectra every 186 ms and the horizontal scale to 186 ms per scan with a 14 ms ISD. With the higher spectral acquisition rate, more definition of the MS signal from each laser pulse was seen, especially at 100 Hz laser pulse repetition rate. Increasing the MS transfer cell traveling wave (twave) amplitude from 1.0 V to 1.4 V also reduced the ion pulse widths and some degree of peak separation was apparent even at 200 Hz laser pulse repetition rate.

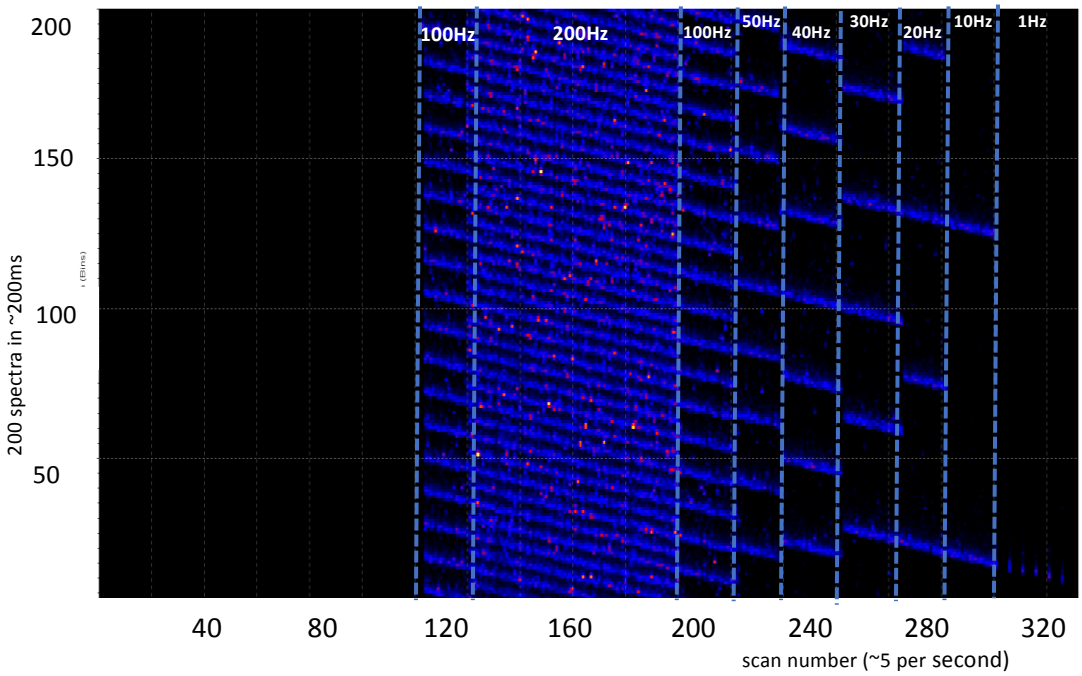

Figure 70 Heat map of the $[M+2H]^{2+}$ bradykinin ion signals, as in Figure 69 except for 186 ms per scan plus 14 ms ISD, the y-axis represents the spectra 1 – 200 (i.e. ~ 1000 spectra /sec). Separation of ion signals were seen at 100Hz and 200 Hz. The twave amplitudes were also increased to reduce signal broadening.

Figure 71(a) shows the total ion current (TIC) chromatogram of the data from Figure 70 when the laser pulse repetition rate was set at 100Hz. The signals are well separated however in (b) when the laser repetition rate was 200 Hz some overlap was occurring. The spectral acquisition rate for Figure 71 was 200 spectra in 186ms plus 14ms ISD (i.e. ~1000 spectra per second with only 1.4% data loss during the ISD period). The time interval per spectrum was 0.93 ms. It should be noted that the heat map lines in Figure 69 and Figure 70 are not exactly horizontal due to minor differences in the spectral rates and the laser repetition rates. It appears from Figure 71b that the separation of signals from individual laser shots was less obvious at 200Hz compared to the displayed heat map data of Figure 70. This may stem from user interface limitations during the selection of the data from the heat map (difficulty in selecting just one scan).

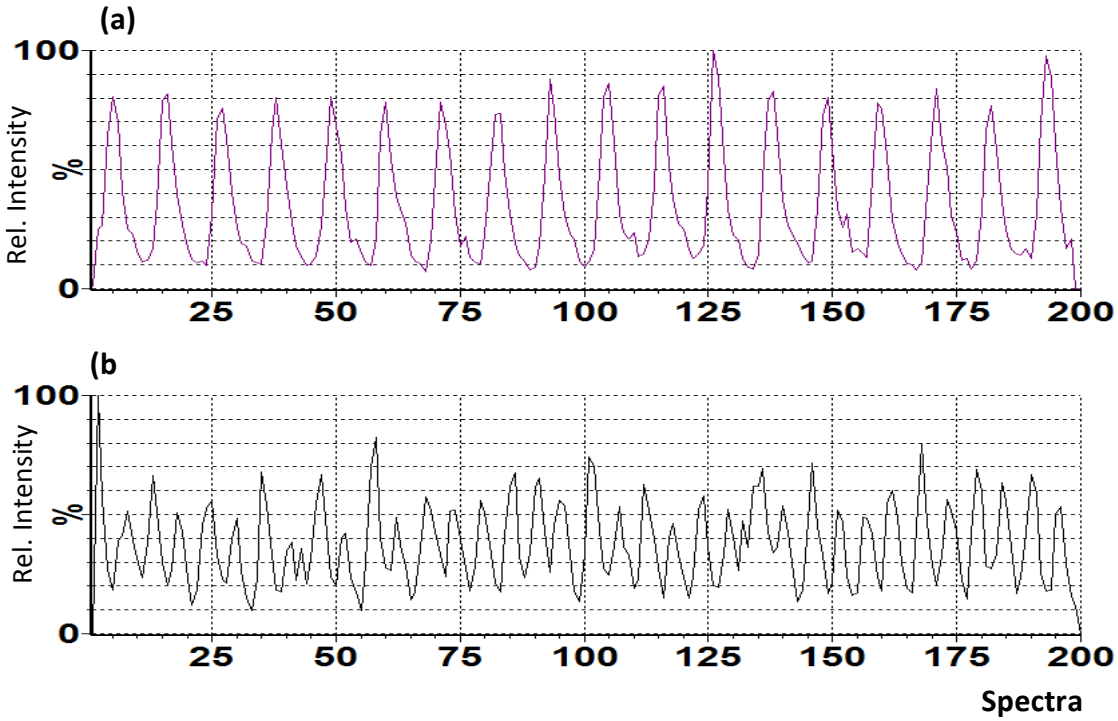

Figure 71: Total ion current (TIC) chromatograms of the experiment for Figure 72. Spectra were acquired at a rate of 1000 spectra per second (200 spectra in 186ms + 14 ms ISD). The laser was firing at 100 Hz in trace (a) and 200 Hz in trace (b). At 100 Hz the ion signals are well separated however at 200Hz, overlap was significant.

The FWHM of the 100Hz ion pulses can be seen in Figure 72 at approximately 3 ms (i.e. FWHM of ~3.2 spectra x 0.93 ms per spectrum).

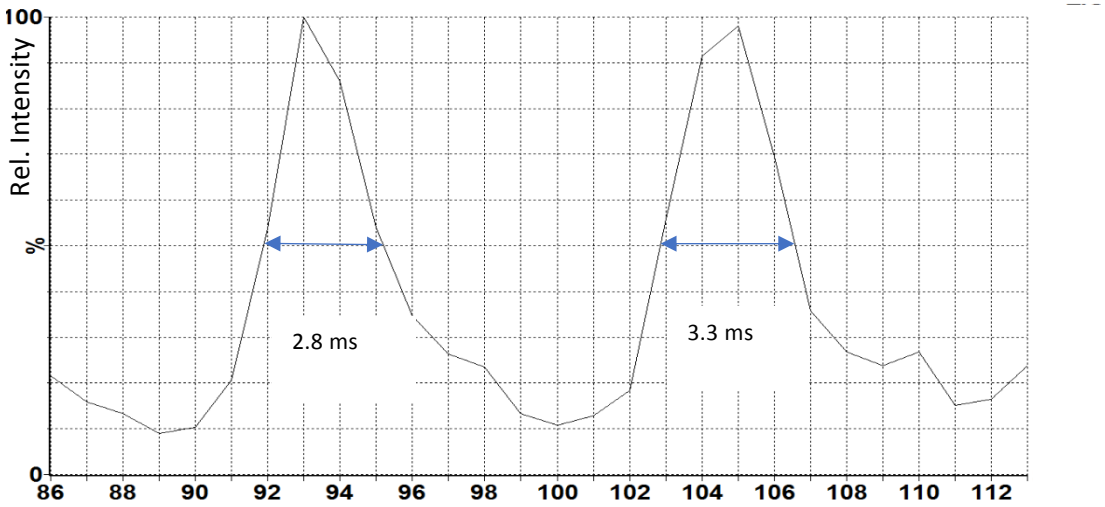

Figure 72: Close up of two ion signal pulses when the laser pulse repetition rate was 100Hz. The FWHM of the ions signals was approximately 3ms.

To investigate the degree of carry over between laser pulses, Figure 73 shows a comparison of the sum of spectra 92 to 95 (top), versus the sum of spectra 100 to 101 (bottom) from Figure 72. The bottom spectrum illustrates that very little carry over is occurring between adjacent laser pulses when the repetition rate was 100Hz (i.e. less than 5% as the vertical scales are linked).

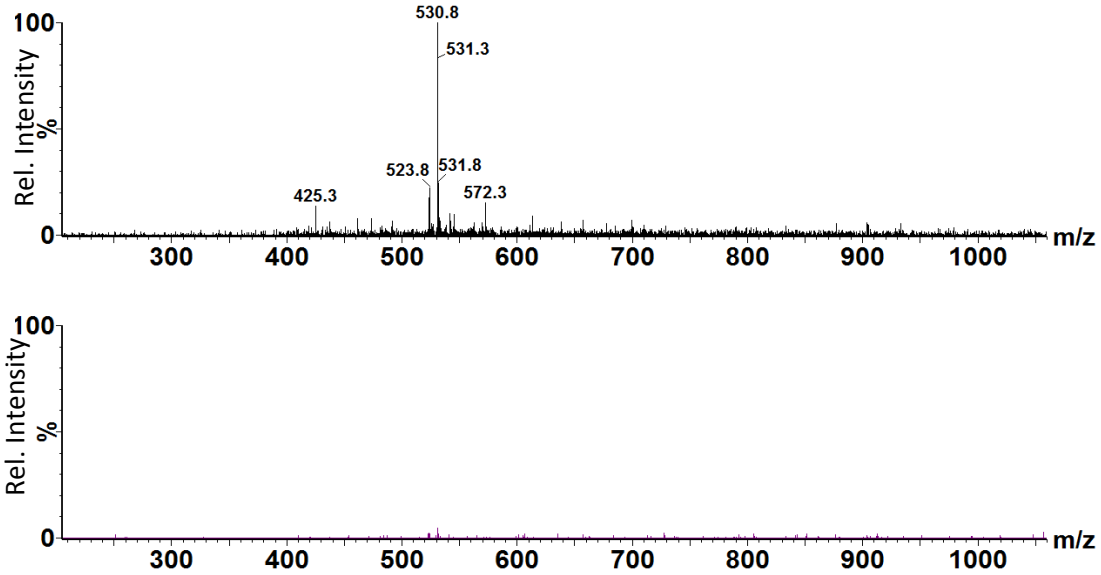

Figure 73: Comparison of data for the sum of spectra 92 to 95 (top), versus sum of spectra 100 to 101 (bottom) from Figure 72. The vertical scales are linked to illustrate the minimal carry over between laser pulses.

The throughput rate, as limited by the ionisation plume time spread through the MS system and the ability of the MS data acquisition to acquire high speed spectra suggests that > 100 samples/second may be acquired with minimal carry over. In order to realise this maximum throughput, rate the XY sample stage would need to move precisely and synchronously with the MS acquisition. If the MALDI sample droplets are deposited on the sample plate every 2.25 mm (1536 well micro-titre pitch), the XY stage needs to move at speeds greater than 225 mm/sec in order to take full advantage of this data acquisition rate. (XY stage speeds up to 1000 mm/sec are readily available.)

Even without the acquisition system modifications as detailed in this chapter, acquisition rates up to 5 samples/second for peptides, lipids and antibiotics have been reported using the liquid AP-MALDI technique.[123] This would be equivalent to 432,000 samples per day. These speeds of analysis are highly competitive with other commercial MS based techniques. For example, a review by Krenka in 2018 listed the following:[124] Agilent Rapidfire, 7 secs/sample (12300 / day) from 10µL volumes; Advion Nanomate, 45 sec/ sample (1920 / day) from 1-10µL volumes; DESI 2.8 samples/sec (10,000 / day) from 50nL volumes; and acoustic mist (AMS) at 3 samples/sec (240,000 /day) from 0.5 -500pL volume.

It may therefore be concluded from the results presented in this chapter that ultra-high throughput sample acquisition beyond 10 samples per second should be easily obtained and the system described may well be capable of >100 samples per second.

6. Conclusions and future directions

The liquid AP-MALDI source first developed by Cramer[41] has been successfully fitted to a different mass spectrometer, the Synapt G2-Si. Work to optimise the design of the inlet capillary was required to benefit from the high sensitivity of the mass spectrometer. The construction of the ion source, the optimisation of the gas flow within the inlet capillary and the operation/modification of the MS is detailed in the thesis.

Optimisation of the cone gas flow within the capillary improved the signal for multiply charged peptides by at least an order of magnitude, possibly through improvements in desolvation temperature and droplet transit time into the first vacuum region of the ion source. Furthermore, the acquisition of data using ion mobility provided a further significant enhancement via drift time filtering to remove singly charged interferences of the chemical noise (mainly the matrix) from the analyte spectra. This aspect was able to increase the signal-to-noise to approximately 500:1 when less than 100 fmol of peptide sample was consumed.

Electron-mediated fragmentation techniques such as ECD and ETD provide complementary information to CID, the fragment ions can retain post-translational modifications and the fragmentation data tends to be easier to interpret since the ion-electron reaction is non-ergodic.[125] Liquid AP-MALDI provides higher charge state ions that are required with fragmentation techniques such as ECD and ETD. These developments thus allow MALDI to benefit from the advantages of these techniques which so far has been exclusively the domain of ESI-generated cations. Although good ETD spectra could be obtained, screening and/or purging of the ion source from ambient air is likely to improve the reliability of signals for the glow discharge anion reagent. ECD of multiply charged MALDI ions was demonstrated on a Q-TOF system for the first time, using a prototype ECD device that was installed after the ion mobility cell. Furthermore, it was shown that the ECD fragment ions retained the drift profile of the precursor ions thus

allowing “on-the-fly” IMS-ECD to be carried out. Future work should aim to reduce the level of CID fragmentation for higher charged peptides whilst entering and leaving the ECD cell. This could be addressed by using helium as a buffer gas in the transfer cell. Overall, for MS/MS it was shown that the relative abundance and profile of fragment ions from ESI-generated ions was very similar to liquid AP-MALDI-generated ions, indicating that there is no ionisation memory effect once the ions are formed and transferred to further analysis.

For the liquid AP-MALDI set-up described in this study, the optimum laser energy (fluence) in terms of the highest doubly charged ion signal was measured at 14µJ per laser pulse (~150µm laser spot diameter). This allowed continuous acquisitions from a 1 µL MALDI sample droplet for up to 90 minutes with a laser pulse repetition rate of 10 Hz. The fluence was found to be approximately similar to conventional solid-state dried-droplet MALDI[107] (at least within a factor 4) and the MALDI sample droplet consumption was calculated at approximately 20 pL for each laser pulse. The optimum fluence level for liquid AP-MALDI was orders of magnitude lower in comparison to what was previously reported for laserspray ionisation.[108]

Laser-based ion sources provide highly precise and flexibly controlled spatial and temporal ionisation events due to the tight focal point and timing of the laser pulse. These features explain why the application of MALDI-TOF for ion imaging has been successful. Other high throughput applications such as the analysis of single nucleotide polymorphisms (SNP)[90] and bacterial fingerprinting[126] also employ MALDI-TOF instrumentation. However, these systems still need to mitigate the traditional sweet-spot problems associated with crystalline MALDI. Analysis directly from liquid droplets, without the need to hunt for sweet-spots (and with the additional benefit of producing multiply charged ions), suggests that liquid AP-MALDI may also be beneficial for the SNP and bacterial analysis applications.

Experiments showed that for higher laser pulse repetition rates (whilst maintaining optimum fluence) the analyte ion signal per unit time increased linearly up to approximately 1 kHz, i.e. the

ion signal per laser pulse was constant. However, between 1 kHz and 5 kHz the ion signal per unit time stayed approximately constant. Future optimisation of the matrix and/or laser parameters (including pulse duration and/or wavelength) may provide sensitivity advances when operating at laser repetition rates higher than 1 kHz.

Having established the maximum laser pulse repetition rate and optimum (low) fluence values, experiments to investigate the potential of high-throughput sample analysis were carried out. It was found that for individual laser pulses, ion signals could be acquired separately, reproducibly and with minimal carry-over from laser pulse to laser pulse at laser pulse repetition rates exceeding 100 Hz. To observe the ion signals at 100 Hz, modifications were made to the acquisition software that enabled spectral acquisition rates beyond 1000 spectra per second. The data obtained suggests that sample rates above 10 samples per second should be easily obtained. With further engineering of the motorised XY sample plate stage, sample throughput rates may be able to reach 100 samples per second with readily available components. To complement the mass spectrometer speed, high-throughput sample preparation and sample spotting robotics are also required. Another challenge would involve the informatics given high volume of data being generated by such systems whilst ensuring that each sample analysed can be accurately tracked.

At the time of writing this thesis, the COVID-19 pandemic is causing significant loss of life and disrupting livelihoods. Although non-MS RNA-based testing methods are already available, alternative and/or complementary testing assays should also be developed. Rapid, sensitive and specific diagnosis by fast and unambiguous testing seems critical as it allows the tracking and isolation of infected people and their close contacts. In order to determine if the SARS-CoV-2 virus had previously infected an individual, electrochemiluminescence[127] based assays have recently been released by Roche Diagnostics. Although the tests are highly specific and sensitive to the presence of the SARS-CoV-2 virus antibodies, the test takes 18 minutes per sample.[128] Regarding fast MS based testing approaches, new MALDI-TOF based tests for the SARS-CoV-2

virus have been reported over the last few weeks.[129,130] One assay, from Agena Biosciences announced that their product could test 2300 samples per day.[131] To put this into context, 10 samples per second (as proposed by the liquid AP-MALDI MS technology in this thesis) equates to 860,000 samples per day per MS instrument.

It is therefore hoped that the instrumentation described in this thesis may eventually play a part in the fight against pathogenic threats (such as the SARS-CoV-2 virus) through the development of ultra-high throughput screening assays.

7. Bibliography

1. P. Ryumin, J. Brown, M. Morris and R. Cramer, Investigation and optimization of parameters affecting the multiply charged ion yield in AP-MALDI MS, *Methods*, 2016, **104**, 11–20

2. P. Ryumin, J. Brown, M. Morris and R. Cramer, Protein identification using a nanoUHPLC-AP-MALDI MS/MS workflow with CID of multiply charged proteolytic peptides, *Int. J. Mass Spectrom.*, 2017, **416**, 20–28

3. O. J. Hale, P. Ryumin, J. M. Brown, M. Morris and R. Cramer, Production and analysis of multiply charged negative ions by liquid atmospheric pressure matrix-assisted laser desorption/ionization mass spectrometry, *Rapid Commun. Mass Spectrom.*, 2018, 1–8

4. H. Krenkel, E. Hartmane, C. Piras, J. Brown, M. Morris and R. Cramer, Advancing Liquid Atmospheric Pressure Matrix-Assisted Laser Desorption/Ionization Mass Spectrometry Toward Ultrahigh-Throughput Analysis, *Anal. Chem.*, 2020, 2931–2936

5. E. Goldstein, 'Vorläufige Mittheilungen über elektrische Entladungen in verdünnten Gasen' (Preliminary communications on electric discharges in rarefied gases), *Monatsberichte der Königlich Preuss. Akad. der Wissenschaften zu Berlin (Monthly Reports R. Prussian Acad. Sci. Berlin)*, 1876, 279–295

6. M. A. Grayson, The evolution of mass spectrometry:1920 to 1940, https://www.asms.org/docs/history-posters/evolution-of-ms-1910-to-1940-2010.pdf?sfvrsn=2

7. J. J. Thomson, Rays of Positive Electricity, *Proc. Roy. Soc. London,*

8. G. Lappin and R. C. Garner, Current perspectives of 14C-isotope measurement in biomedical accelerator mass spectrometry., *Anal. Bioanal. Chem.*, 2004, **378**, 356–364

9. D. Z. Keifer, E. E. Pierson and M. F. Jarrold, Charge detection mass spectrometry: Weighing heavier things, *Analyst*, 2017, **142**, 1654–1671

10. Liam A. McDonnell* and Ron M.A. Heeren*, IMAGING MASS SPECTROMETRY, *Mass Spectrom. Rev.*, 2007, **26**, 606–643

11. J. Balog, L. Sasi-Szabó, J. Kinross, M. R. Lewis, L. J. Muirhead, K. Veselkov, R. Mirnezami, B. Dezso, L. Damjanovich, A. Darzi, J. K. Nicholson and Z. Takáts, Intraoperative tissue identification using rapid evaporative ionization mass spectrometry, *Sci. Transl. Med.*, 2013, **5**, 194ra93-194ra93

12. Strategic Directions International: Global Assessment Report - The Laboratory Analytical & Life Science Instrumentation Industry Report 19-001, *SDI Global Assessment Report 10.5*, 2009

13. M. Karas and F. Hillenkamp, Laser desorption ionization of proteins with molecular masses exceeding 10,000 daltons, *Anal. Chem.*, 1988, **60**, 2299–2301

14. K. Tanaka, H. Waki, Y. Ido, S. Akita, Y. Yoshida, T. Yoshida and T. Matsuo, Protein and

polymer analyses up tom/z 100 000 by laser ionization time-of-flight mass spectrometry, *Rapid Commun. Mass Spectrom.*, 1988, **2**, 151–153

15. M. Yamashita and J. B. Fenn, Electrospray ion source. Another variation on the free-jet theme, *J. Phys. Chem.*, 1984, **88**, 4451–4459

16. S. J. Gaskell, SPECIAL FEATURE : Electrospray : Principles and Practice, 1997, **32**, 677–688

17. Lord Rayleigh, XX. On the equilibrium of liquid conducting masses charged with electricity , *London, Edinburgh, Dublin Philos. Mag. J. Sci.*, 1882, **14**, 184–186

18. M. Dole, L. L. Mack, R. L. Hines, D. O. Chemistry, R. C. Mobley, L. D. Ferguson and M. B. Alice, Molecular beams of macroions, *J. Chem. Phys.*, 1968, **49**, 2240–2249

19. J. V. Iribarne and B. A. Thomson, On the evaporation of small ions from charged droplets, *J. Chem. Phys.*, 1976, **64**, 2287–2294

20. L. Konermann, E. Ahadi, A. D. Rodriguez and S. Vahidi, Unraveling the mechanism of electrospray ionization, *Anal. Chem.*, 2013, **85**, 2–9

21. R. Kaufmann, F. Hillenkamp and R. Wechsung, The laser microprobe mass analyzer (LAMMA): A new instrument for biomedical microprobe analysis, *Med. Prog. Technol.*, 1979, **6**, 109–121

22. E. Denoyer, R. Van Grieken, F. Adams and D. F. S. Natusch, Laser Microprobe Mass Spectrometry 1: Basic Principles and Performance Characteristics, *Anal. Chem.*, 1982, **54**, 26–41

23. F. Hillenkamp and J. Peter-Katalinic, *MALDI MS: a practical guide to instrumentation, methods and applications*, John Wiley & Sons, 2nd edn., 2013

24. M. Karas, D. Bachmann, U. Bahr and F. Hillenkamp, Matrix-assisted ultraviolet laser desorption of non-volatile compounds, *Int. J. Mass Spectrom. Ion Process.*, 1987, **78**, 53–68

25. J. Karas, Michael;Gluckmann, Matthias; Schafer, Ionization in matrix-assisted laser desorption/ionization: singly charged molecular ions are the lucky survivors, *J. Mass Spectrom.*

26. J. L. Stephenson and S. A. McLuckey, Ion/ion reactions in the gas phase: Proton transfer reactions involving multiply-charged proteins, *J. Am. Chem. Soc.*, 1996, **118**, 7390–7397

27. M. Karas and R. Krüger, Ion formation in MALDI: The cluster ionization mechanism, *Chem. Rev.*, 2003, **103**, 427–439

28. T. W. Jaskolla and M. Karas, Compelling evidence for lucky survivor and gas phase protonation: The unified MALDI analyte protonation mechanism, *J. Am. Soc. Mass Spectrom.*, 2011, **22**, 976–988

29. A. S. Kononikhin, E. N. Nikolaev, V. Frankevich and R. Zenobi, Multiply charged ions in matrix-assisted laser desorption/ionization generated from electrosprayed sample layers., *Eur. J. Mass Spectrom. (Chichester, Eng).*, 2005, **11**, 257–9

30. V. V. Laiko, M. A. Baldwin and A. L. Burlingame, Atmospheric pressure matrix-assisted laser desorption/ionization mass spectrometry, *Anal. Chem.*, 2000, **72**, 652–657

31. C. Keller, J. Maeda, D. Jayaraman, S. Chakraborty, M. R. Sussman, J. M. Harris, J.-M. Ané and L. Li, Comparison of Vacuum MALDI and AP-MALDI Platforms for the Mass

Spectrometry Imaging of Metabolites Involved in Salt Stress in Medicago truncatula, *Front. Plant Sci.*, 2018, **9**, 1238

32. V. V Laiko, V. M. Doroshenko, S. Jackson, H. J. Wang and A. S. Woods, Atmospheric Pressure MALDI Imaging Mass Spectrometry Tissue Imaging requirements RESULTS MS Profiling of tissue sections : Matrix selection AP-MALDI MS Imaging of tissue sections :, 18388

33. E. Moskovets, A. Misharin, V. Laiko and V. Doroshenko, A comparative study on the analytical utility of atmospheric and low-pressure MALDI sources for the mass spectrometric characterization of peptides, *Methods*, 2016, **104**, 21–32

34. B. Spengler and M. Hubert, Scanning microprobe matrix-assisted laser desorption ionization (SMALDI) mass spectrometry: instrumentation for sub-micrometer resolved LDI and MALDI surface analysis., *J. Am. Soc. Mass Spectrom.*, 2002, **13**, 735–48

35. K. Dreisewerd, The desorption process in MALDI., *Chem. Rev.*, 2003, **103**, 395–426

36. P. Ryumin and R. Cramer, The composition of liquid atmospheric pressure matrix-assisted laser desorption/ionization matrices and its effect on ionization in mass spectrometry, *Anal. Chim. Acta*, 2018, **1013**, 43–53

37. R. Cramer and A. L. Burlingame, Employing target modifications for the investigation of liquid infrared matrix-assisted laser desorption/ionization mass spectrometry, *Rapid Commun. Mass Spectrom.*, 2000, **14**, 53–60

38. M. Palmblad and R. Cramer, Liquid Matrix Deposition on Conductive Hydrophobic Surfaces for Tuning and Quantitation in UV-MALDI Mass Spectrometry, , DOI:10.1016/j.jasms.2006.11.013

39. M. Cramer, Rainer;Towers, Liquid Matrices for Analyses by UV-MALDI Mass Spectrometry | Spectroscopy, *Spectroscopy*, 2007, **22**, 29–37

40. S. König, O. Kollas and K. Dreisewerd, Generation of highly charged peptide and protein ions by atmospheric pressure matrix-assisted infrared laser desorption/ionization ion trap mass spectrometry., *Anal. Chem.*, 2007, **79**, 5484–8

41. R. Cramer, A. Pirkl, F. Hillenkamp and K. Dreisewerd, Liquid AP-UV-MALDI enables stable ion yields of multiply charged peptide and protein ions for sensitive analysis by mass spectrometry, *Angew. Chemie - Int. Ed.*, 2013, **52**, 2364–2367

42. S. Trimpin, E. D. Inutan, T. N. Herath and C. N. McEwen, Laserspray ionization, a new atmospheric pressure MALDI method for producing highly charged gas-phase ions of peptides and proteins directly from solid solutions., *Mol. Cell. Proteomics*, 2010, **9**, 362–7

43. A. Hirabayashi, M. Sakairi and H. Koizumi, Sonic Spray Mass Spectrometry, *Anal. Chem.*, 1995, **67**, 2878–2882

44. C. N. McEwen, V. S. Pagnotti, E. D. Inutan and S. Trimpin, New paradigm in ionization: Multiply charged ion formation from a solid matrix without a laser or voltage, *Anal. Chem.*, 2010, **82**, 9164–9168

45. S. Trimpin, C. Lee, S. M. Weidner, T. J. El-Baba, C. A. Lutomski, E. D. Inutan, C. D. Foley, C. K. Ni and C. N. McEwen, Unprecedented Ionization Processes in Mass Spectrometry Provide Missing Link between ESI and MALDI, *ChemPhysChem*, 2018, **19**, 581–589

46. V. S. Pagnotti, N. D. Chubatyi and C. N. McEwen, Solvent assisted inlet ionization: an

ultrasensitive new liquid introduction ionization method for mass spectrometry., *Anal. Chem.*, 2011, **83**, 3981–3985

47. V. S. Pagnotti, E. D. Inutan, D. D. Marshall, C. N. McEwen and S. Trimpin, Inlet ionization: A new highly sensitive approach for liquid chromatography/mass spectrometry of small and large molecules, *Anal. Chem.*, 2011, **83**, 7591–7594

48. A. J. Harding, J. Hough, C. Curtis, D. Kinsman and M. R. Clench, Matrix-assisted ionisation in vacuum mass spectrometry and imaging on a modified quadrupole-quadrupole-time-of-flight mass spectrometer, *J. Spectr. Imaging*, 2019, **8**, 1–9

49. W. Paul and H. Steinwedel, Ein neues Massenspektrometer ohne Magnetfeld, *Paul W.*, 1952, **8**, 448–450

50. H. G. Dehmelt, Radiofrequency Spectroscopy of Stored Ions I: Storage, *Adv. At. Mol. Opt. Phys.*, 1968, **3**, 53–72

51. S. Guan and A. G. Marshall, Stacked-ring electrostatic ion guide, *J. Am. Soc. Mass Spectrom.*, 1996, **7**, 101–106

52. W. M. Brubaker, *Advances in Mass Spectrometry*, 1968, vol. 4

53. K. Giles, S. D. Pringle, K. R. Worthington, D. Little, J. L. Wildgoose and R. H. Bateman, Applications of a travelling wave-based radio-frequency-only stacked ring ion guide, *Rapid Commun. Mass Spectrom.*, 2004, **18**, 2401–2414

54. S. D. Pringle, K. Giles, J. L. Wildgoose, J. P. Williams, S. E. Slade, K. Thalassinos, R. H. Bateman, M. T. Bowers and J. H. Scrivens, An investigation of the mobility separation of some peptide and protein ions using a new hybrid quadrupole/travelling wave IMS/oa-ToF instrument, *Int. J. Mass Spectrom.*, 2007, **261**, 1–12

55. R. J. Barlow, *Statistics: A Guide to the Use of Statistical Methods in the Physical Sciences*, John Wiley and Sons Ltd, Chichester, 1999

56. M. Lewin, M. Guilhaus, F. Read, J. Wildgoose, J. Hoyes, B. Bateman, B. St, M. Manchester, M. Uk and F. R. Wythenshawe, Ion Dispersion near Grids in TOFMS The Critical Effect of the Angle of Incidence School of Chemistry , The University of New South Wales , Sydney 2052 Australia ;, 2001, **2**, 3–4

57. B. Mamyrin, V. Karataev, D. Shmikk and V. Zagulin, The mass-reflectron, a new nonmagnetic time-of-flight mass spectrometer with high resolution, *Sov. J. Exp. Theor. Phys.*, 1973, **37**, 45

58. J. Wildgoose and J. Brown, in *Proceedings of the 56th ASMS Conference on Mass Spectrometry and Allied Topics , Denver , CO*, 2008, p. 2008

59. R. S. Brown and J. J. Lennon, Mass Resolution Improvement by Incorporation of Pulsed Ion Extraction in a Matrix-Assisted Laser Desorption/Ionization Linear Time-of-Flight Mass Spectrometer, *Anal. Chem.*, 1995, **67**, 1998–2003

60. W. C. Wiley and I. H. McLaren, Time-of-flight mass spectrometer with improved resolution, *Rev. Sci. Instrum.*, 1955, **26**, 1150–1157

61. Micromass, Micromass M@LDI Mass Spectrometer Operators Guide, https://www.waters.com/webassets/cms/support/docs/maldi_guide_rev_a.pdf

62. E. Clayton and R. H. Bateman, Letter to the editor, *Rapid Commun. Mass Spectrom.*, 1992,

6, 719–720

63. J. H. J. Dawson and M. Guilhaus, Orthogonal-acceleration time-of-flight mass spectrometer, *Rapid Commun. Mass Spectrom.*, 1989, **3**, 155–159

64. K. Giles, J. Ujma, J. Wildgoose, S. Pringle, K. Richardson, D. Langridge and M. Green, A Cyclic Ion Mobility-Mass Spectrometry System, *Anal. Chem*, 2019, **91**, 24

65. A. Verenchikov, S. Kirillov, Y. Khasin, V. Makarov, M. Yavor and V. Artaev, Multiplexing in Multi-Reflecting TOF MS, *J. Appl. Solut. Chem. Model.*, 2017, **6**, 1–22

66. ETP, MagneTOF ™: A New Class of Robust Sub-nanosecond TOF Detectors with Exceptional Dynamic Range, https://www.etp-ms.com/file-repository/8

67. J. Ladislas Wiza, Microchannel plate detectors, *Nucl. Instruments Methods*, 1979, **162**, 587–601

68. G. Westmacott, M. Frank, S. E. Labov and W. H. Benner, Using a superconducting tunnel junction detector to measure the secondary electron emission efficiency for a microchannel plate detector bombarded by large molecular ions, *Rapid Commun. Mass Spectrom.*, 2000, **14**, 1854–1861

69. A. L. Rockwood, M. Busman and R. D. Smith, Coulombic effects in the dissociation of large highly charged ions, *Int. J. Mass Spectrom. Ion Process.*, 1991, **111**, 103–129

70. L. A. Gethings, K. Richardson, J. Wildgoose, S. Lennon, S. Jarvis, C. L. Bevan, J. P. C. Vissers and J. I. Langridge, Lipid profiling of complex biological mixtures by liquid chromatography/mass spectrometry using a novel scanning quadrupole data-independent acquisition strategy, *Rapid Commun. Mass Spectrom.*, 2017, **31**, 1599–1606

71. R. A. Zubarev, N. L. Kelleher, F. W. Mclafferty and R. V October, Electron Capture Dissociation of Multiply Charged Protein Cations . A Nonergodic Process, 1998, **7863**, 3265–3266

72. D. B. Robb, M. Brown, M. Morris and M. W. Blades, Tandem Mass Spectrometry Using the Atmospheric Pressure Electron Capture Dissociation Ion Source

73. J. E. P. Syka, J. J. Coon, M. J. Schroeder, J. Shabanowitz and D. F. Hunt, Peptide and protein sequence analysis by electron transfer dissociation mass spectrometry., *Proc. Natl. Acad. Sci. U. S. A.*, 2004, **101**, 9528–33

74. F. Lermyte, T. Verschueren, J. M. Brown, J. P. Williams, D. Valkenborg and F. Sobott, Characterization of top-down ETD in a travelling-wave ion guide, *Methods*, 2015, **89**, 22–29

75. B. C. Katzenmeyer, L. R. Cool, J. P. Williams, K. Craven, J. M. Brown and C. Wesdemiotis, Electron transfer dissociation of sodium cationized polyesters: Reaction time effects and combination with collisional activation and ion mobility separation, *Int. J. Mass Spectrom.*, 2015, **378**, 303–311

76. F. Lermyte, J. P. Williams, J. M. Brown, E. M. Martin and F. Sobott, Extensive Charge Reduction and Dissociation of Intact Protein Complexes Following Electron Transfer on a Quadrupole-Ion Mobility-Time-of-Flight MS, *J. Am. Soc. Mass Spectrom.*, 2015, 1068–1076

77. F. Lermyte, A. Konijnenberg, J. P. Williams, J. M. Brown, D. Valkenborg and F. Sobott, ETD allows for native surface mapping of a 150 kDa noncovalent complex on a commercial Q-TWIMS-TOF instrument, *J. Am. Soc. Mass Spectrom.*, 2014, **25**, 343–350

78. K. D. Rand, S. D. Pringle, M. Morris, J. R. Engen and J. M. Brown, ETD in a traveling wave ion guide at tuned Z-spray ion source conditions allows for site-specific hydrogen/deuterium exchange measurements., *J. Am. Soc. Mass Spectrom.*, 2011, **22**, 1784–93

79. J. P. Williams, J. M. Brown, I. Campuzano and P. J. Sadler, Identifying drug metallation sites on peptides using electron transfer dissociation (ETD), collision induced dissociation (CID) and ion mobility-mass spectrometry (IM-MS)., *Chem. Commun. (Camb).*, 2010, **46**, 5458–60

80. K. C. I. Campuzano, J. Brown, J. Williams, J. Langridge, *J. Biomol. Tech.*, 2010, 21, S36

81. M. Hervé, R. Brédy, G. Karras, B. Concina, J. Brown, A.-R. R. Allouche, F. Lépine and I. Compagnon, On-the-Fly Femtosecond Action Spectroscopy of Charged Cyanine Dyes: Electronic Structure versus Geometry, *J. Phys. Chem. Lett.*, 2019, **10**, 2300–2305

82. A. Theisen, R. Black, D. Corinti, J. M. Brown, B. Bellina, P. E. Barran, U. H. Mistarz, S. A. Chandler, J. M. Brown, J. L. P. Benesch and K. D. Rand, Initial Protein Unfolding Events in Ubiquitin, Cytochrome c and Myoglobin Are Revealed with the Use of 213 nm UVPD Coupled to IM-MS, *J. Am. Soc. Mass Spectrom.*, 2019, **30**, 24–33

83. U. H. U. H. Mistarz, B. Bellina, P. F. P. F. Jensen, J. M. J. M. Brown, P. E. P. E. Barran and K. D. K. D. Rand, UV Photodissociation Mass Spectrometry Accurately Localize Sites of Backbone Deuteration in Peptides, *Anal. Chem.*, 2018, **90**, 1077–1080

84. J. S. Brodbelt, Shedding light on the frontier of photodissociation., *J. Am. Soc. Mass Spectrom.*, 2011, **22**, 197–206

85. M. A. Halim, M. Girod, L. Macaleese, J. Lemoine, R. Antoine, P. Dugourd, I. L. Matière, U. L. Cnrs, U. De Lyon, V. Cedex, S. Analytiques, U. L. Cnrs, U. De Lyon and V. Cedex, 213 nm Ultraviolet Photodissociation on Peptide Anions: Radical-Directed Fragmentation Patterns, 2016, 474–486

86. P. Roepstorff and J. Fohlman, *Biol. Mass Spectrom.*, 1984, 11, 601–601

87. R. S. Johnson, S. A. Martin and K. Biemann, Novel Fragmentation Process of Peptides by Collision- Induced Differentiation of Leucine and Isoleucine, 1987, 2621–2625

88. R. S. Johnson, S. A. Martin, K. Biemann, J. T. Stults and J. Throck Watson, *Novel Fragmentation Process of Peptides by Collision-Induced Decomposition in a Tandem Mass Spectrometer: Differentiation of Leucine and Isoleucine*, 1987, vol. 59

89. M. M. Wolff and W. E. Stephens, A pulsed mass spectrometer with time dispersion, *Rev. Sci. Instrum.*, 1953, **24**, 616–617

90. P. Ross, L. Hall, I. Smirnov and L. Haff, High level multiplex genotyping by MALDI-TOF mass spectrometry, *Nat. Biotechnol.*, 1998, **16**, 1347–1351

91. I. Sinclair, M. Bachman, D. Addison, M. Rohman, D. C. Murray, G. Davies, E. Mouchet, M. E. Tonge, R. G. Stearns, L. Ghislain, S. S. Datwani, L. Majlof, E. Hall, G. R. Jones, E. Hoyes, J. Olechno, R. N. Ellson, P. E. Barran, S. D. Pringle, M. R. Morris and J. Wingfield, Acoustic mist ionization platform for direct and contactless ultrahigh-throughput mass spectrometry analysis of liquid samples, *Anal. Chem.*, 2019, **91**, 3790–3794

92. Z. Takáts, J. M. Wiseman, B. Gologan and R. G. Cooks, Mass spectrometry sampling under ambient conditions with desorption electrospray ionization, *Science (80-.).*, 2004, **306**, 471–473

93. M. Vestal, L. Li, E. Dobrinskikh, Y. Shi, B. Wang, X. Shi, S. Li, C. Vestal and K. Parker, Rapid MALDI-TOF molecular imaging: Instrument enhancements and their practical consequences, *J. Mass Spectrom.*, , DOI:10.1002/jms.4423

94. Micromass, Z-SPRAY COMBINED INLET/ION SOURCE, https://notendur.hi.is/~agust/kennsla/ee05/verkl/MALDITOF/decode talk oct 9/itarefni2/zspbtb.pdf

95. D. Fenyo, Q. Wang, J. A. DeGrasse, J. C. Padovan, M. Cadene and B. T. Chait, MALDI sample preparation: The ultra thin layer method, *J. Vis. Exp.*, , DOI:10.3791/192

96. Spectra Physics, Explorer OEM Diode-Pumped, Q-Switched, Ultraviolet Laser System User's Manual, https://www.spectra-physics.com/assets/client_files/files/documents/service/user-manuals/Explorer-349 OEM User's Manual Rev. A.pdf

97. J. P. Williams, S. Pringle, K. Richardson, L. Gethings, J. P. C. C. Vissers, M. De Cecco, S. Houel, A. B. Chakraborty, Y. Q. Yu, W. Chen and J. M. Brown, Characterisation of glycoproteins using a quadrupole time-of-flight mass spectrometer configured for electron transfer dissociation, *Rapid Commun. Mass Spectrom.*, 2013, **27**, 2383–2390

98. K. L. Fort, C. N. Cramer, V. G. Voinov, Y. V. Vasil'Ev, N. I. Lopez, J. S. Beckman and A. J. R. Heck, Exploring ECD on a Benchtop Q Exactive Orbitrap Mass Spectrometer, *J. Proteome Res.*, 2018, **17**, 926–933

99. J. B. Shaw, N. Malhan, Y. V. Vasil'Ev, N. I. Lopez, A. Makarov, J. S. Beckman and V. G. Voinov, Sequencing Grade Tandem Mass Spectrometry for Top-Down Proteomics Using Hybrid Electron Capture Dissociation Methods in a Benchtop Orbitrap Mass Spectrometer, *Anal. Chem.*, 2018, **90**, 10819–10827

100. V. G. Voinov, J. S. Beckman, M. L. Deinzer, D. F. Barofsky and F. Glu-fibrinopeptide, (730) Radio Frequency-Free Electromagnetostatic Cell For ECD, CID And Combined ECD/CID Mass Spectrometry, 2009, 690022

101. J. P. Williams, L. Morrison, C. J. Hughes, J. Beckman, V. G. Voinov, F. Lermyte and J. M. Brown, in *Proceedings of the 67th ASMS Conference on Mass Spectrometry and Allied Topics , Atlanta, Georgia*, 2019

102. J. P. Williams, L. J. Morrison, J. M. Brown, J. S. Beckman, V. G. Voinov and F. Lermyte, Top-Down Characterization of Denatured Proteins and Native Protein Complexes Using Electron Capture Dissociation Implemented within a Modified Ion Mobility-Mass Spectrometer, *Anal. Chem.*, 2020, **92**, 3674–3681

103. C. Hao, R. E. March, T. R. Croley, J. C. Smith and S. P. Rafferty, Electrospray ionization tandem mass spectrometric study of salt cluster ions. Part 1 - Investigations of alkali metal chloride and sodium salt cluster ions, *J. Mass Spectrom.*, 2001, **36**, 79–96

104. K. Dreisewerd, M. Schürenberg, M. Karas and F. Hillenkamp, Influence of the laser intensity and spot size on the desorption of molecules and ions in matrix-assisted laser desorption/ionization with a uniform beam profile, *Int. J. Mass Spectrom. Ion Process.*, 1995, **141**, 127–148

105. K. Dreisewerd, M. Schürenberg, M. Karas and F. Hillenkamp, Matrix-assisted laser desorption/ionization with nitrogen lasers of different pulse widths, *Int. J. Mass Spectrom. Ion Process.*, 1996, **154**, 171–178

106. F. Hillenkamp and K. Dreisewerd, in *Proceedings of the 49th ASMS Conference on Mass Spectrometry and Allied Topics, Chicago, Illinois, May 27- 31, 2001.*, 2001

107. V. S. and W. E. Hui Qiao, The effect of laser profile, fluence, and spot size on sensitivity in orthogonal-injection matrix-assisted laser desorption/ionization time-of-flight mass spectrometry, *Rapid Commun. Mass Spectrom.*, 2008, **22**, 2779

108. S. Trimpin, B. Wang, E. D. Inutan, J. Li, C. B. Lietz, A. Harron, V. S. Pagnotti, D. Sardelis and C. N. McEwen, A mechanism for ionization of nonvolatile compounds in mass spectrometry: Considerations from MALDI and inlet ionization, *J. Am. Soc. Mass Spectrom.*, 2012, **23**, 1644–1660

109. T. J. Kauppila, J. A. Syage and T. Benter, Recent developments in atmospheric pressure photoionization-mass spectrometry, *Mass Spectrom. Rev.*, 2017, **36**, 423–449

110. P. Kebarle and U. H. Verkerk, Ion-Ion and ion-molecule reactions at the surface of proteins produced by nanospray. Information on the number of acidic residues and control of the number of ionized acidic and basic residues, http://massspecgateway.net/Authenticated.aspx?doi=10.1016/j.jasms.2005.03.018, (accessed 21 October 2014)

111. H. Kambara and I. Kanomata, ms240271.pdf, *Mass Spectrosc.*, 1976, **24**, 271–282

112. W. Ens, K. G. Standing and I. V. Chernushevich, Eds., in *New Methods for the Study of Biomolecular Complexes*, Springer Netherlands, Dordrecht, 1998

113. J. B. Fenn, Ion formation from charged droplets: Roles of geometry, energy, and time, *J. Am. Soc. Mass Spectrom.*, 1993, **4**, 524–535

114. G. A. E. Godsave, Studies of the combustion of drops in a fuel spray—the burning of single drops of fuel, *Symp. Combust.*, 1953, **4**, 818–830

115. Y. Lin, Y. Huang and D. B. Chrisey, Droplet formation in matrix-assisted pulsed-laser evaporation direct writing of glycerol-water solution, *J. Appl. Phys.*, 2009, **105**, 093111

116. J. M. Lafferty, Ed., *Foundations of vacuum science and technology*, Wiley New York, 1998

117. M. Pauly, M. Sroka, J. Reiss, G. Rinke, a Albarghash, R. Vogelgesang, H. Hahne, B. Kuster, J. Sesterhenn, K. Kern and S. Rauschenbach, A hydrodynamically optimized nano-electrospray ionization source and vacuum interface., *Analyst*, 2014, **139**, 1856–67

118. S. Mochizuki, Effective methods for the measurement of CsI cluster ions using MALDI-MS with suitable solvent combinations and additives, *J. Mass Spectrom.*, 2014, **49**, 1199–1202

119. Waters, Synapt G2-S specifications, https://www.waters.com/webassets/cms/library/docs/720004005en.pdf

120. H. P. Gunawardena, M. He, P. a. Chrisman, S. J. Pitteri, J. M. Hogan, B. D. M. Hodges and S. a. McLuckey, Electron transfer versus proton transfer in gas-phase ion/ion reactions of polyprotonated peptides, *J. Am. Chem. Soc.*, 2005, **127**, 12627–12639

121. H. P. Gunawardena, M. He, P. A. Chrisman, S. J. Pitteri, J. M. Hogan, B. D. M. Hodges and S. A. McLuckey, Electron transfer versus proton transfer in gas-phase ion/ion reactions of polyprotonated peptides., *J. Am. Chem. Soc.*, 2005, **127**, 12627–12639

122. V. Frankevich, J. Zhang, M. Dashtiev and R. Zenobi, Production and fragmentation of multiply charged ions in 'electron-free' matrix-assisted laser desorption/ionization, *Rapid*

Commun. Mass Spectrom., 2003, **17**, 2343–2348

123. H. Krenkel, E. Hartmane, C. Piras, J. Brown, M. Morris and R. Cramer, Advancing Liquid Atmospheric Pressure Matrix-Assisted Laser Desorption/Ionization Mass Spectrometry Toward Ultrahigh-Throughput Analysis, *Anal. Chem.*, 2020, **92**, 2931–2936

124. E. E. Kempa, K. A. Hollywood, C. A. Smith and P. E. Barran, High throughput screening of complex biological samples with mass spectrometry-from bulk measurements to single cell analysis, *Analyst*, 2019, **144**, 872–891

125. K. Breuker, H. Oh, C. Lin, B. K. Carpenter and F. W. McLafferty, Nonergodic and conformational control of the electron capture dissociation of protein cations, *Proc. Natl. Acad. Sci. U. S. A.*, 2004, **101**, 14011–14016

126. A. Croxatto, G. Prod'hom and G. Greub, Applications of MALDI-TOF mass spectrometry in clinical diagnostic microbiology, *FEMS Microbiol. Rev.*, 2012, **36**, 380–407

127. H. Ju, G. Lai and F. Yan, *Electrochemiluminescent immunosensing*, 2017

128. Roche Diagnostics, Elecsys® Anti-SARS-CoV-2, https://diagnostics.roche.com/global/en/products/params/elecsys-anti-sars-cov-2.html

129. M. F. Rocca, J. C. Zintgraff, M. E. Dattero, L. S. Santos, M. Ledesma, C. Vay, M. Prieto, E. Benedetti, M. Avaro, M. Russo, F. M. Nachtigall and E. Baumeister, A Combined approach of MALDI-TOF Mass Spectrometry and multivariate analysis as a potential tool for the detection of SARS-CoV-2 virus in nasopharyngeal swabs, *bioRxiv*, 2020, 2020.05.07.082925

130. MAP Sciences, UK DIAGNOSTICS FIRM ANNOUNCES DEVELOPMENT OF RAPID TEST FOR THE COVID-19 VIRUS, https://mapsciences.com/uk-diagnostics-firm-announces-development-of-rapid-test-for-the-covid-19-virus/

131. Agena Biocience, Low-Cost and High-Throughput SARS-CoV-2 RNA Detection, https://agenabio.com/products/panels/coronavirus-sars-cov-2-detection-research-panel/

8. Appendices

8.1 Safety

Special care and training are required when working with high voltage power supplies and laser beams. The lasers used in this study were classified as “safety class 4” requiring appropriate laser eye protection goggles and other screening and signage measures as well as consultation with the laser safety officer.

To fit the liquid AP-MALDI source the several source safety interlocks had to be overridden to enable the instrument to go into “Operate” for the operation of the source high voltage power supply and relevant gas controls within the system. Relevant warning signs were posted near exposed high voltage components to warn of the risk of electrical shock hazard.

8.2 WRENS C# Script

```
//increases cone gas by 10L/h every 5 seconds J. Brown

public override void main()
{
            connect("epc"); //connects to embedded PC


            for(double i=0;i<200;i+=10)// from 0 to 200 insteps of 10
            {
                  set_property("CONE_GAS_SETTING", i.ToString());
                  wait(5000); // wait  5 seconds
            print(i.ToString());
            }
```

8.3 Selection of related patents (published granted and published applications)

(12) **United States Patent**
Brown et al.

(10) **Patent No.: US 9,947,521 B2**
(45) **Date of Patent: Apr. 17, 2018**

(54) **AUXILIARY GAS INLET**

(71) Applicant: **Micromass UK Limited**, Wilmslow (GB)

(72) Inventors: **Jeffery Mark Brown**, Hyde (GB); **Rainer Cramer**, Reading (GB)

(73) Assignee: **MICROMASS UK LIMITED**, Wilmslow (GB)

(*) Notice: Subject to any disclaimer, the term of this patent is extended or adjusted under 35 U.S.C. 154(b) by 0 days.

(21) Appl. No.: **15/155,669**

(22) Filed: **May 16, 2016**

(65) **Prior Publication Data**

US 2016/0336157 A1 Nov. 17, 2016

(30) **Foreign Application Priority Data**

May 15, 2015 (GB) 1508328.0

(51) **Int. Cl.**
H01J 49/04 (2006.01)

(52) **U.S. Cl.**
CPC ***H01J 49/0404*** (2013.01); ***H01J 49/04*** (2013.01); *H01J 49/0418* (2013.01)

(58) **Field of Classification Search**
CPC H01J 49/0404; H01J 49/04; H01J 49/0418
USPC 250/281, 282, 286, 288
See application file for complete search history.

(56) **References Cited**

U.S. PATENT DOCUMENTS

5,318,752	A	6/1994	Visser
6,649,908	B2	11/2003	Apffel, Jr. et al.
6,707,037	B2	3/2004	Whitehouse
6,770,875	B1	8/2004	Guevremont et al.
6,806,468	B2	10/2004	Laiko et al.
7,470,899	B2	12/2008	Atherton et al.
9,293,315	B2	3/2016	Makarov
2005/0269518	A1	12/2005	Bajic et al.
2010/0282966	A1	11/2010	Schneider et al.

Primary Examiner — Nicole Ippolito
Assistant Examiner — Hanway Chang
(74) *Attorney, Agent, or Firm* — Womble Bond Dickinson (US) LLP; Deborah M. Vernon; Heath T. Misley

(57) **ABSTRACT**

There is provided a method of introducing ions into a mass spectrometer, comprising ionising a sample using a Matrix Assisted Laser Desorption Ionisation ("MALDI") ion source to form a plurality of ions, transporting said plurality of ions in a first, primary gas through a passageway and into an inlet of a mass spectrometer, introducing a second, auxiliary gas into said inlet, and controlling a flow rate of said second gas into said inlet so as to control a flow rate of said first gas through said passageway.

15 Claims, 5 Drawing Sheets

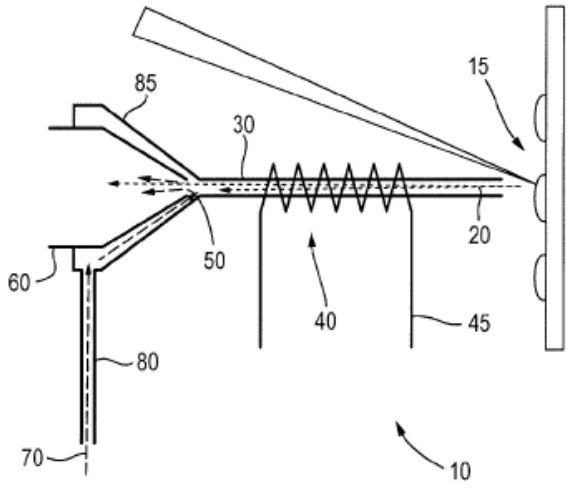

US009881779B2

(12) **United States Patent**
Brown

(10) **Patent No.: US 9,881,779 B2**
(45) **Date of Patent: Jan. 30, 2018**

(54) **AUXILIARY GAS INLET**

(71) Applicant: **Micromass UK Limited**, Wilmslow (GB)

(72) Inventor: **Jeffery Mark Brown**, Hyde (GB)

(73) Assignee: **MICROMASS UK LIMITED**, Wilmslow (GB)

(*) Notice: Subject to any disclaimer, the term of this patent is extended or adjusted under 35 U.S.C. 154(b) by 0 days.

(21) Appl. No.: **15/155,622**

(22) Filed: **May 16, 2016**

(65) **Prior Publication Data**

US 2016/0336156 A1 Nov. 17, 2016

(30) **Foreign Application Priority Data**

May 15, 2015 (GB) 1508325.6

(51) **Int. Cl.**
H01J 49/04 (2006.01)
H01J 49/24 (2006.01)
H01J 49/16 (2006.01)

(52) **U.S. Cl.**
CPC ***H01J 49/0404*** (2013.01); *H01J 49/165* (2013.01)

(58) **Field of Classification Search**
CPC H01J 49/0404; H01J 49/165; H01J 49/24
USPC 250/281, 282, 283, 288
See application file for complete search history.

(56) **References Cited**

U.S. PATENT DOCUMENTS

5,318,752	A	6/1994	Visser	
9,293,315	B2	3/2016	Makarov	
2010/0282966	A1	11/2010	Schneider et al.	
2012/0228492	A1 *	9/2012	Franzen	H01J 49/401 250/288
2014/0097338	A1 *	4/2014	Eiler	H01J 49/0009 250/282
2016/0126078	A1 *	5/2016	Liepert	H01J 49/24 250/282

* cited by examiner

Primary Examiner — Nicole Ippolito
(74) *Attorney, Agent, or Firm* — Womble Bond Dickinson (US) LLP; Deborah M. Vernon; Health T. Misley

(57) **ABSTRACT**

There is provided a method of introducing ions into a mass spectrometer, comprising ionising a sample using a continuous ionisation source to form a plurality of ions, transporting said plurality of ions in a first, primary gas through a passageway and into an inlet of a mass spectrometer, introducing a second, auxiliary gas into said inlet, and controlling a flow rate of said second gas into said inlet so as to control a flow rate of said first gas through said passageway.

21 Claims, 1 Drawing Sheet

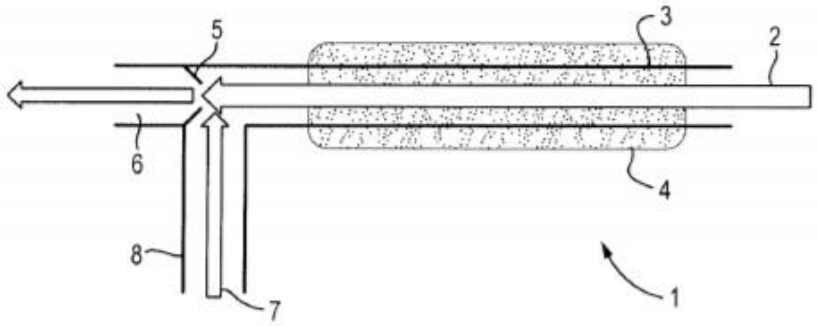

US010090144B2

(12) **United States Patent**
Brown

(10) **Patent No.: US 10,090,144 B2**
(45) **Date of Patent: Oct. 2, 2018**

(54) **LIQUID EXTRACTION MATRIX ASSISTED LASER DESORPTION IONISATION ION SOURCE**

(71) Applicant: **Micromass UK Limited**, Wilmslow (GB)

(72) Inventor: **Jeffery Mark Brown**, Hyde (GB)

(73) Assignee: **MICROMASS UK LIMITED**, Wilmslow (GB)

(*) Notice: Subject to any disclaimer, the term of this patent is extended or adjusted under 35 U.S.C. 154(b) by 0 days.

(21) Appl. No.: **15/126,721**

(22) PCT Filed: **Mar. 18, 2015**

(86) PCT No.: **PCT/GB2015/000095**
§ 371 (c)(1),
(2) Date: **Sep. 16, 2016**

(87) PCT Pub. No.: **WO2015/140491**
PCT Pub. Date: **Sep. 24, 2015**

(65) **Prior Publication Data**

US 2017/0117125 A1 Apr. 27, 2017

(30) **Foreign Application Priority Data**

Mar. 18, 2014 (EP) 14160588
Mar. 18, 2014 (GB) 1404847.4

(51) **Int. Cl.**
H01J 49/00 (2006.01)
H01J 49/16 (2006.01)
H01J 49/04 (2006.01)

(52) **U.S. Cl.**
CPC ***H01J 49/164*** (2013.01); ***H01J 49/0431*** (2013.01); ***H01J 49/165*** (2013.01)

(58) **Field of Classification Search**
CPC H01J 49/164; H01J 49/165; H01J 49/0431
(Continued)

(56) **References Cited**

U.S. PATENT DOCUMENTS

5,965,884 A 10/1999 Laiko et al.
6,140,639 A 10/2000 Gusev et al.
(Continued)

FOREIGN PATENT DOCUMENTS

GB 2511643 10/2014
WO 98/53308 11/1998

OTHER PUBLICATIONS

Sampson et al., "Generation and Detection of Multiply-Charged Peptides and Proteins by Matrix-Assisted Laser Desorption Electrospray Ionization (MALDESI) Fourier Transform Ion Cyclotron Resonance Mass Spectrometry", Journal American Society for Mass Spectrometry , vol. 17, No. 12, pp. 1712-1716, 2006.
(Continued)

Primary Examiner — Nicole Ippolito
Assistant Examiner — Hanway Chang
(74) *Attorney, Agent, or Firm* — Womble Bond Dickinson (US) LLP; Deborah M. Vernon; Heath T. Misley

(57) **ABSTRACT**

A Matrix Assisted Laser Desorption Ionization ("MALDI") ion source is disclosed comprising a first device arranged and adapted to supply a flow of liquid on to the surface of a target or a sample to be analyzed so that the liquid forms a liquid junction on the surface of the target or the sample to be analyzed and wherein analyte molecules to be ionized are extracted into the liquid junction, and a laser source emits a laser beam which causes analyte ions or an analyte plume to be released or desorbed from the liquid junction.

20 Claims, 1 Drawing Sheet

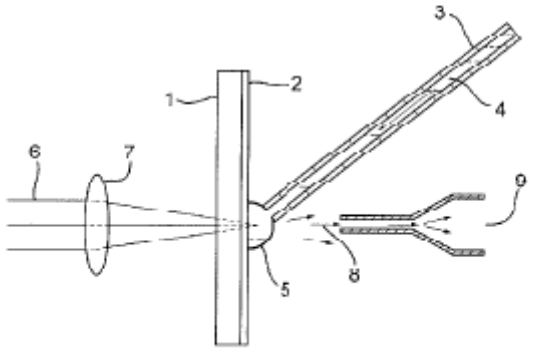

(12) INTERNATIONAL APPLICATION PUBLISHED UNDER THE PATENT COOPERATION TREATY (PCT)

(19) World Intellectual Property Organization
International Bureau

(43) International Publication Date
18 October 2018 (18.10.2018)

WIPO | PCT

(10) International Publication Number
WO 2018/189544 A1

(51) International Patent Classification:
H01J 49/04 (2006.01)

(21) International Application Number:
PCT/GB2018/050973

(22) International Filing Date:
12 April 2018 (12.04.2018)

(25) Filing Language: English

(26) Publication Language: English

(30) Priority Data:
1705981.7 13 April 2017 (13.04.2017) GB

(71) Applicant: **MICROMASS UK LIMITED** [GB/GB]; Stamford Avenue, Altrincham Road, Wilmslow SK9 4AX (GB).

(72) Inventor: **BROWN, Jeffery Mark**; Dial House, Old Hall Lane, Mottram-in-Longdendale, Hyde Cheshire SK14 6LT (GB).

(74) Agent: **DEHNS**; St Bride's House, 10 Salisbury Square, London Greater London EC4Y 8JD (GB).

(81) Designated States *(unless otherwise indicated, for every kind of national protection available)*: AE, AG, AL, AM, AO, AT, AU, AZ, BA, BB, BG, BH, BN, BR, BW, BY, BZ, CA, CH, CL, CN, CO, CR, CU, CZ, DE, DJ, DK, DM, DO, DZ, EC, EE, EG, ES, FI, GB, GD, GE, GH, GM, GT, HN, HR, HU, ID, IL, IN, IR, IS, JO, JP, KE, KG, KH, KN, KP, KR, KW, KZ, LA, LC, LK, LR, LS, LU, LY, MA, MD, ME, MG, MK, MN, MW, MX, MY, MZ, NA, NG, NI, NO, NZ, OM, PA, PE, PG, PH, PL, PT, QA, RO, RS, RU, RW, SA, SC, SD, SE, SG, SK, SL, SM, ST, SV, SY, TH, TJ, TM, TN, TR, TT, TZ, UA, UG, US, UZ, VC, VN, ZA, ZM, ZW.

(84) Designated States *(unless otherwise indicated, for every kind of regional protection available)*: ARIPO (BW, GH, GM, KE, LR, LS, MW, MZ, NA, RW, SD, SL, ST, SZ, TZ, UG, ZM, ZW), Eurasian (AM, AZ, BY, KG, KZ, RU, TJ, TM), European (AL, AT, BE, BG, CH, CY, CZ, DE, DK, EE, ES, FI, FR, GB, GR, HR, HU, IE, IS, IT, LT, LU, LV, MC, MK, MT, NL, NO, PL, PT, RO, RS, SE, SI, SK, SM, TR), OAPI (BF, BJ, CF, CG, CI, CM, GA, GN, GQ, GW, KM, ML, MR, NE, SN, TD, TG).

Published:
— *with international search report (Art. 21(3))*

(54) Title: MALDI TARGET PLATE

Fig. 1

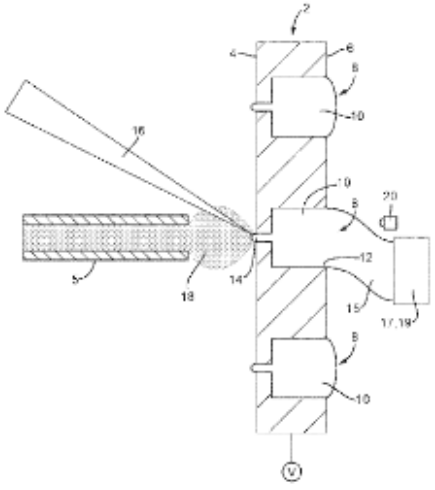

(57) Abstract: A MALDI ion source is disclosed comprising: a target plate (2) having a front surface (4), a rear surface (6), and at least one sample receiving well (9) for receiving a liquid sample or at least one sample receiving channel (8) extending from an opening (12) in the rear surface (6) to an opening (14) in the front surface (4) for receiving a liquid sample (10), wherein each well (9) or channel (8) has a volume of ≥ 1 μL. The ion source also comprise a laser (16) for ionising a liquid sample (10) on or in the target plate (2), wherein the laser (16) is a pulsed laser set up and configured to have a pulsed repetition rate of ≥ 20 Hz, or is a continuous laser.

WO 2018/189544 A1